Simulated Fatigue Testing and Condition Monitoring Investigation by Vibration Analysis of a Composite Material Fan Blade Structure

by
Anro Malan Olivier

Thesis presented in partial fulfilment of the requirements for the degree of Master of Engineering (Mechanical) in the Faculty of Engineering at Stellenbosch University

Supervisor: Dr DNJ Els
Co-supervisor: Prof AA Groenwold

April 2019

Declaration

By submitting this report electronically, I declare that the entirety of the work contained therein is my own, original work, that I am the sole author thereof (save to the extent explicitly otherwise stated), that reproduction and publication thereof by Stellenbosch University will not infringe any third party rights and that I have not previously in its entirety or in part submitted it for obtaining any qualification.

Date: April 2019

Plagiarism Declaration

1. Plagiarism is the use of ideas, material and other intellectual property of another's work and to present it as my own.
2. I agree that plagiarism is a punishable offence because it constitutes theft.
3. I also understand that direct translations are plagiarism.
4. Accordingly all quotations and contributions from any source whatsoever (including the internet) have been cited fully. I understand that the reproduction of text without quotation marks (even when the source is cited) is plagiarism.
5. I declare that the work contained in this assignment, except where otherwise stated, is my original work and that I have not previously (in its entirety or in part) submitted it for grading in this module/assignment or another module/assignment.

AM Olivier Initials and surname	April 2019 Date

Abstract

Simulated Fatigue Testing and Condition Monitoring Investigation by Vibration Analysis of a Composite Material Fan Blade Structure

AM Olivier

Department of Mechanical and Mechatronic Engineering,
University of Stellenbosch,
Private Bag X1, Matieland 7602, South Africa.

Thesis: MEng (Mech)

April 2019

A study on composite materials fatigue for a fan blade used in air cooled condensers (ACCs) is presented. The purpose of this study is to investigate the fatigue properties of composite materials with the intent of including the gathered knowledge in the maintenance considerations of ACC fan blades. Information about the loading conditions seen during operation of an installed fan was used to formulate a full-scale accelerated constant amplitude test with the goal of investigating stiffness degradation as a measure of damage progression. This was achieved by firstly conducting material and fatigue tests on test specimens and then by conducting a full-scale fatigue test on a structure designed to simulate a fan blade. The outcomes of the material specimen tests were a stress-life curve and stiffness degradation information at different fatigue loading levels which are compared to the full-scale test results. The full-scale test results show that the first natural frequency of the structure degrades in a similar trend as bending stiffness and monitoring natural frequency degradation over time, therefore has the potential to be used as a condition monitoring method for installed fan blades.

Uittreksel

Gesimuleerde Vermoeidheidstoetsing en Toestandsmoniteringondersoek deur middel van Vibrasie Analise van 'n Saamgestelde Materiaal Waaierlemstruktuur

AM Olivier

Departement Meganiese en Megatroniese Ingenieurswese,
Universiteit van Stellenbosch,
Privaatsak X1, Matieland 7602, Suid Afrika.

Tesis: MIng (Meg)

April 2019

Hierdie tesis omvat 'n studie oor die vermoeidheid van saamgestelde materiaal waaierlemme wat in lugverkoelde kondensators gebruik word. Die doel van hierdie studie is om die vermoeidheidseienskappe van saamgestelde materiale te ondersoek en om die kennis toe te pas op die instandhoudingoorwegings van waaierlemme in lugverkoelde kodensators. Inligting oor die belastingstoestande wat tydens die werking van 'n geïnstalleerde waaierlem versamel is, is gebruik om 'n volskaalse versnelde konstante amplitude toets te formuleer met die doel om die styfheidsvermindering as 'n maatstaaf van skadeprogressie te ondersoek. Hierdie is behaal deur eerstens materiaal- en vermoeidheidstoetse op materiaalmonsters te doen en dan deur 'n volskaalse vermoeidheidstoets te doen op 'n struktuur wat ontwerp is om 'n waaierlem te simuleer. Die uitkomste van die materiaalmonster toetse was 'n spannings-leeftydkuwe en inligting oor styfheidsvermindering by verskillende vlakke van vermoeidheidsbelasting. Hierdie resultate is met die resutate van die volskaalse toets vergelyk. Die resultate van volskaalse toetsing toon dat die eerste natuurlike frekwensie van die struktuur teen 'n soortgelyke tendens as buigstyfheid verminder en dat die monitering van die vermindering van natuurlike frekwensie oor tyd, dus die potensiaal het om as 'n metode van toestand monitering vir geïnstalleerde waaierlemme gebruik te word.

Acknowledgements

The author thanks his suporvisor Dr DNJ Els and co-supervisor Professor AA Groenwold for their support and guidance in scientific research. The funders Min-Water CSP and Horizon2020 provided the essential funding and research drive for this project. Another word of thanks to the many people who made themselves available for advice, assistance or support throughout the course of this project.

Contents

List of Figures

List of Tables

List of Abbreviations

ACC Air Cooled Condenser
CSP Concentrated Solar Power
CNC Computer Numerical Control
GFRP Glass Fibre Reinforced Polymer
FRP Fibre Reinforced Polymer
FEA Finite Element Analysis
S-N Stress - Life
CA Constant Amplitude
RFC Rainflow Counting
ASTM American Society for Testing and Materials
DOF Degree Of Freedom
FI Failure Index
EMA Experimental Modal Analysis
FRF Frequency Response Function
SDOF Single Degree Of Freedom
LVDT Linear Variable Displacement Transducer
NI National Instruments
DAQ Data Acquisition Controller
UTS Ultimate Tensile Strength
MRR Modulus Reduction Ratio

Nomenclature

Variables

a	Amplitude	[mm]
e	Ultimate Strain	[m/m]
E	Young's Modulus	[Pa]
f	Frequency (time)	[Hz]
F	Force	[N]
F	Stress Interaction Term	[ ]
FI	Failure Index	[ ]
g	Gravitational Acceleration	[9.81 m/s^2]
G	Shear Modulus	[Pa]
I	Area moment of Inertia	[m^4]
l	Length	[m]
m	Mass	[kg]
M	Bending Moment	[$N \cdot m$]
N	Number of Cycles	[N]
r^2	Coefficient of Determination	[ ]
R	Fatigue Stress Ratio	[ ]
S	Ultimate Strength	[Pa]
W	Power	[Watt]
γ	Shear Strain	[m/m]
δ	Change in displacement	[m/m]
ϵ	Strain	[m/m]
θ	Angle	[rad]
ν	Poisson's Ratio	[ ]
ρ	Density	[kg/m^3]
σ	Stress	[Pa]

τ	Shear Stress	$[\mathrm{Pa}]$
ω	Frequency (radial)	$[\mathrm{rad} \cdot \mathrm{s}]$

Subscripts

a	Amplitude
c	Compression
e	Endurance Limit
f	Final Condition
m	Mean
max	Maximum
min	Minimum
t	Tension
ut	Ultimate Tensile
x	Defined X-axis (global coordinates)
y	Defined Y-axis (global coordinates)
yp	Yield Point
0	Initial Condition
1	Longitudinal Direction (local coordinates)
2	Transverse Direction (local coordinates)
3	Depth-wise Longitudinal Direction (local coordinates)
LW	Lag-wise direction
FW	Flap-wise direction
$tors$	Torsional direction

Chapter 1

Introduction

1.1 Background and Motivation

Power generation systems such as coal fired and concentrated solar plants (CSP) that operate on the Rankine cycle, generate electricity by passing pressurised steam through turbines. Not all of the energy in the steam is utilised in electricity generation and the heat remaining in low quality steam or condensate needs to be rejected through a cooling system. The conventional wet cooling systems use cooling towers where heat is exchanged in a open system between high temperature water and the atmosphere. Fans can be implemented to induce a draft in the cooling tower which increases cooling efficiency. Either way, the exchanging of heat in a cooling tower typically leads to considerable water losses to the atmosphere which can be seen as white plumes exiting the cooling towers.

South Africa has a national average rainfall of 500 mm and most regions of South Africa are therefore considered semi-arid or arid (WeatherSA, 2018). For this reason, dry cooling systems, also known as air cooled condensers (ACCs) have become an attractive means to save water. The working of an ACC is very similar to that of a motorcar radiator. It depends on constant air flow, which draws atmospheric air over cooling surfaces called the heat exchanger bundles which contain the fluid to be cooled. Air cooled condensers can be encountered in natural draft, forced draft or induced draft types. A natural draft configuration relies on a natural temperature gradient to induce airflow while airflow is generated by large diameter fans in the latter two types. Figures 1.1 and 1.2 illustrate a V-configuration of an induced draft ACC and an A-configuration of a forced draft ACC respectively.

Due to the use of air-cooled condensers (ACCs) instead of conventional cooling towers, dry-cooled power stations need 200 times less water per unit of electric-

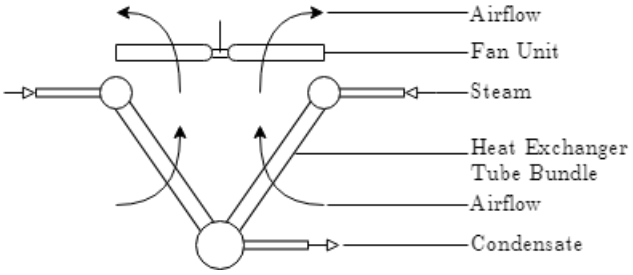

Figure 1.1: V-Configuration induced draft ACC bundle

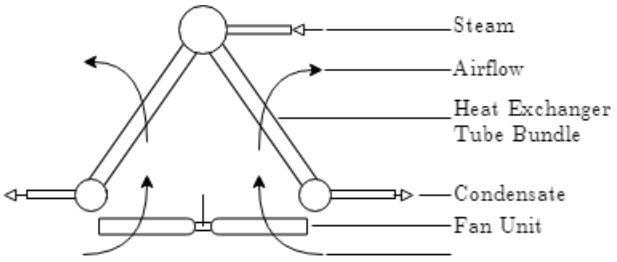

Figure 1.2: A-Configuration forced draft ACC bundle

ity generated and as a result have become the norm on the South African power generation landscape. Besides conventional coal fired power plants, ACCs are also recently being implemented for cooling at CSP plants, which are usually located in regions where sun exposure is high and water availability is low. Figure 1.3 is an aerial image of the Redstone CSP plant near Postmasburg in the Northern Cape of South Africa.

The MinWaterCSP (2018) Project, supported by the European Commission Horizon 2020 programme, aims to develop technologies that increase efficiency and significantly reduce water consumption in CSP plants. Included in one of the Project's work packages is the development of a large diameter axial flow fan which shows the abilities of the consortium to successfully manufacture and test fans for implementation in A-configuration forced draft ACCs (Els *et al.*, 2018). For this reason a newly designed, improved ACC fan was built, installed and tested in the Matimba Power Station ACC.

The Matimba Power Station in Mpumalanga, South Africa, is a coal-fired power plant with a total installed capacity of 3 990 MW and is the largest dry-cooled power station in the world. In the ACC which is shown in figure 1.4, 288 axial flow fans,

Figure 1.3: Redstone solar thermal power plant in South Africa (Solarreserve, 2018)

each with eight fan blades spanning a diameter of approximately 9 m. These fans induce the draught for an air side condenser surface area of 1 200 000 m^2. The fans consume approximately 5.6 % of the power generated by the power station (Eskom, 2016).

Figure 1.4: Matimba power station (Eskom, 2016)

The harsh conditions that the fan blades in an ACC operates under makes them susceptible to fatigue failure. Defined as the gradual deterioration in material properties caused by repeated cyclic loading, fatigue is a common cause of part failure in many industries that have equipment operating continuously. It has been referred to as the "silent killer" since the progression of fatigue is often difficult to detect with the naked eye and can occur even when a part operates well below the yield strength of the material. The onset of fatigue in homogeneous materials usually

occurs as a small crack propagating from a stress concentration. The mechanisms for fatigue in composite materials are different to the simplistic crack propagation model for homogeneous materials. The increasing amount of applications for composite materials in new industries make the characterisation of fatigue a matter of high importance. Wind turbine fan blade fatigue is a topic on which there is a field of growing research interest and it happens that the fan blades that are the topic of this research project have a very similar construction and operating conditions. This fortunate circumstance shall be used in this project as a starting point to the eventual goal of characterising fatigue behaviour in a composite materials fan blade.

A full scale performance test is shown in figure 1.5. This test was performed on the fan at Matimba Power Station by Els and Muiyser (2016) over a period of three days. The results concluded the fan to be well suited for full time installation at this location. The improved fan blade offers a closed blade root which decreases recirculation effects and increases fan static pressure with up to 21 % less power consumption. The new fan blades are manufactured with CNC technology and an improved resin infusion process which decreases the mass of the structure and increases the quality of the final product. These fan blades have been designed with a vibrational response that ensures minimal excitation of natural frequencies during operation. A further step in the analysis of the suitability of the fan blade is to consider the structural response of the fan blades to dynamic loading conditions. The fans used in ACCs should be safe to operate continuously under cyclic aerodynamic loads, fluctuating ambient temperature, humidity and wind conditions. When the operating frequency of the fan is sufficiently close to one of the components' natural frequencies, there is a risk of exciting the fan into resonance which amplifies the loading on parts within the system. These factors all contribute to fatigue loading effects which need to be considered to ensure safe, long term operation. It is therefore important to characterise the effect of long-term cyclic loading on the material within the fan blade and on the structure itself. This research project directs its attention specifically to the study of fatigue response in the fan blade structure designed by the MinWaterCSP project and hopes to answer the seemingly simple question of: "How long will it last?"

The material used for the fan blade construction is a glass fibre reinforced polymer (GFRP) composite material. The mechanical properties of fibre reinforced polymers (FRP) are anisotropic and unlike more conventional homogeneous structural materials can be designed with desirable properties at different locations of a structure. The use of FRPs provides the advantage of creating lightweight structures that can be designed for stiffness under certain loading conditions and compliance under others. This property makes FRP materials ideal for implementation in large fans and rotor blades such as those used in wind turbines. Despite previ-

Figure 1.5: Testing of the ACC fan blades at Matimba power station (Els and Muiyser, 2016)

ously being designated as fatigue-insensitive relative to metals, composite materials will inevitably also be affected by fatigue and it is certainly necessary to investigate its effects (Vassilopoulos and Keller, 2011). Significant attempts have already been made into the fatigue research of wind turbine rotor blades which use a very similar structure and GFRP material. Wind turbine blades often exceed lengths of 40 meters and typically operate at low rotation rates. Although the fan blades mentioned in this project are smaller in scale and operate at much higher rotation rates, the research principles remain the same and the field of wind turbine fatigue testing will be used as a reference and starting point for this research. Both of these structures generally experience loading in one direction due to the air pressure gradients induced by their rotation. Another similarity is that these structures both experience some variance in loading due to wind effects which in the case of wind turbine fatigue research has been addressed by standard test spectrum profiles as discussed by Nijssen (2006*b*).

Various methods of modelling fatigue of composite materials has been developed. A choice on which method to employ will be based on outcome accuracy, cost and time available. Another important consideration for this project is also how to translate a damage model from specimen tests to a full-scale test with the same material health monitoring criteria. The available fatigue models that have been developed can be categorised in different ways depending on the author, however this document shall use the six classifications defined by Mohammadi *et al.* (2017). These classification categories are: (i) S-N curve based fatigue life models; (ii) residual strength models; (iii) residual stiffness models; (iv) progressive damage models; (v) physically based multi-scale damage models; and (vi) continuum damage mechanics models.

S-N based fatigue life models remain the norm despite fatigue behaviour in composite materials being significantly different to that of homogeneous materials for which this model was developed. The shortcoming of this model is that it simply gives information about how far the material has progressed towards ultimate failure, and not the actual deterioration in the material properties which has occurred. The second and third methods offer a solution to this by phenomenologically defining fatigue behaviour based on measurable material properties and give insight into the possible causes of ultimate material failure. The residual strength model is impractical for most purposes since it requires destructive testing of the test specimens after incremented numbers of cycles. This would require many specimens and many days of fatigue testing which might be better used on results processing and analysis.

This study chose the more suitable residual stiffness model for fatigue analysis. Stiffness degradation is not only simple to measure non-destructively, but also provides some clues into the damage mechanisms that contribute towards ultimate failure. Progressive and multi-scale damage models intelligently make predictions based on damage history, but require involved non-linear Finite Element Analysis (FEA) techniques which are not the focus of this study. Continuum damage mechanics models are based on thermodynamic and continuum mechanics laws. These methods focus on the micromechanics of a composite material and since the material composition is often not completely defined, these models can only be used in applications where the material has been fully defined.

1.2 Objectives

- **Investigate Fan Blade Fatigue Behaviour**
  Time histories of loads experienced by the fan blade during operational intervals have already been gathered. From these variable load time histories an accelerated constant amplitude (CA) cyclic load will be selected that will be used to gather information about the material's fatigue behaviour and mechanical property degradation. The study will only be performed for the selected load case and the formulation of a worst case scenario fatigue life prediction will be investigated.

  A substitute structure to the fan blade will be designed to have full control over test variables. Tests on material specimens will assist in the formulation of the final loading sequence, but since this project has only one full-scale structure available for destructive testing, only one CA cycling sequence will

be formulated and implemented.

The objective of full-scale testing will be to conclude whether the fatigue life of the fan blade structure matches the behaviour predicted by specimen testing. Eventually the aim is to provide a characteristic of fatigue life which future researchers and possibly the fan operators.

- **Develop a Material Health Monitoring Sequence**
  Traditional methods of determining the progression of damage will not be possible on such a large structure. A non-destructive testing sequence will be developed for monitoring material health during full scale testing. This testing sequence will be designed such that operators may be able to monitor the health of the structure while mounted on the fan hub. Fatigue failure is progressive and a set of criteria will be developed for when failure of the structure is said to have occurred. This point of failure will be specified to the operators of the fans and a safety factor may be included to ensure that failure is never encountered during operation and the system may remain safe.

1.3 Scope

The objectives of this project will be governed by the following boundaries listed throughout this section. These boundaries are determined by the available time, equipment and funds, as well as the general expectations of a master's thesis.

This project shall determine the fatigue response of a single selected composite material for a single load case. The CA accelerated test shall be based on the worst case operating conditions, calculated in terms of Palmgren-Miner damage (Palmgren, 1959) and realistic testing conditions. Due to the available equipment, fatigue testing shall only consider the effect of cyclic mechanical loading and effects such as temperature and humidity will not be controlled. The fan blade will not be tested on a full-scale level, but an equivalent structure shall be designed based on the static loading response of the fan blade. This structure shall be tested on full scale. Due to the design of the test bench, the equivalent structure will only be loaded in one direction. Furthermore, the boundary conditions of this full-scale test shall be a simplified version of the actual boundary conditions. A distributed load on the fan blade will be simplified to a single point cantilever bending load and the structure will be rigidly mounted. It is recognised that operator negligence and lack of due diligence might make the material health monitoring sequence seem

unrealistic, but the proposed method shall assume ideal design conditions with trained and responsible personnel and an accessible ACC design.

1.4 Outline

The following section provides an outline as to how this project achieved the project objectives successfully:

Following this introductory chapter, the project is sectioned into four more chapters, the first of which is a Literature Review of well established composite materials mechanics and fatigue theory as well as relevant recent research.

The methodology chapter discusses standard fatigue data interpretation methods which will be used to formulate a CA accelerated fatigue load cycle to simulate the variable amplitude loads seen during actual operation. Most prominently the Rainflow Counting (RFC) method described in the ASTM E1049-85 (2003) Standard will be used. The design of a filament wound GFRP structure resembling the fan blade's structural properties using FEA, failure criteria and fatigue analysis software will be discussed. A manufacturable laminate, which is made from the same material as the test specimens, shall also designed in the FEA step. The specimens, along with the experimental set-ups for material and fatigue testing according to the relevant American Society for Testing and Materials (ASTM) standards, shall be discussed together in their corresponding sub-sections. The failure and residual stiffness results from these tests are then processed and briefly reported upon before full-scale testing and modal analysis is discussed.

The results chapter discusses the results of each of the three experimentation steps individually. The static tensile testing results are used in the specimen fatigue testing step, and the specimen fatigue testing results will be used in the full-scale fatigue testing step. This chapter attempts to explain the implementation of test results as well as formulating a simple stiffness degradation model for life prediction of the full-scale structure. The test bench for the full-scale test was designed as part of an undergraduate project at Stellenbosch University. This, as well as the full-scale experimental procedure to extract fatigue results and to test the material health monitoring method is discussed in detail.

The concluding chapter of the project will primarily discuss the how the objectives of the study were achieved. Furthermore, shortcomings and assumptions will be clearly laid out and recommendations for future studies will be made.

Chapter 2

Literature Review

2.1 Fan Blade Loads

Axial flow fans typically operate at constant speeds for long periods of time. In a controlled environment, a perfectly shaped and shrouded fan would experience a highly predictable loading cycle. However, this is not the case for the fans studied in this project where wind, recirculation and manufacturing inconsistencies distort the expected regularity of load cycles to appear distorted and random. In addition, these loads do not occur in only one plane. It is important to be aware of what direction the critical loads are acting in especially if the structure is non-symmetric with potential stress concentrations.

The loads to which axial flow fan blades are subjected to can be referred to by using three degrees of freedom (DOF). Figure 2.1 illustrates the DOF that the fan blade is constrained to. Parallel to the air flow direction is the the flap-wise DOF which is primarily activated by the pressure gradient between the high- and low pressure sides of the air foil as the blade rotates. Since the fan blade is fixed at the rotor hub, loads in the flap-wise direction cause an in-plane bending moment. Loads in the lag-wise DOF plane perpendicular to the air flow direction and are caused by drag forces between the air and the fan blade surface Nijssen (2006*b*). Twisting moments that are caused by uneven pressure distribution of air between the leading and trailing edges of the air foil activate the torsional DOF.

The combination of loads cause complex stress states within the fan blade structure. Different laminate stacking sequences may be used to reinforce the structure against known load cases such as shear, axial or buckling loads.

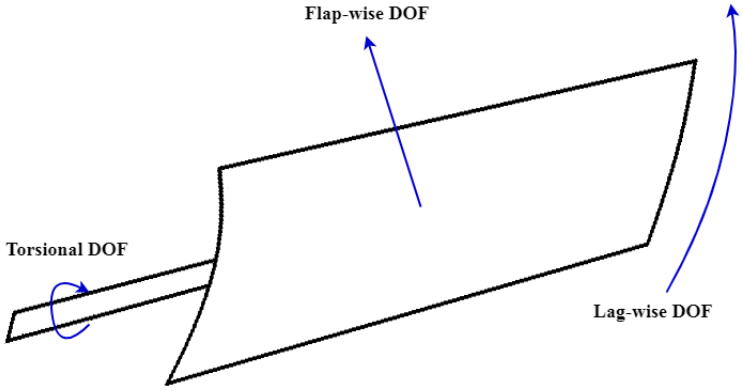

Figure 2.1: Notation for fan blade degrees of freedom

2.2 Classical Lamination Theory

This section covers a brief overview of classical lamination theory (CLT) and although not exhaustive, should provide an elementary understanding of the topic and the principles used in modelling.

In this thesis the terms ply and lamina shall be used interchangeably since both imply a single layer of material of which multiple make up a laminate. Hence, each ply or lamina contributes to the overall material properties of the laminate depending on its constituent materials and fibre orientation. Two composite materials of the exact same constituent materials may have completely different material properties due to the way in which the fibres are aligned in each ply. It is therefore important to specify this stacking sequence according to the notation explained by Gibson (2011). This convention has the following rules:

1. The stacking of plies starts from the top of the laminate as shown in Figure 2.4.
2. The stacking sequence reports the orientation of fibres in the global coordinate system.
3. The stacking sequence is written in square brackets.
4. Each layer or groups of layers are separated by a forward slash symbol.
5. The subscript, n, is used to indicate repeated groups or layers.

6. The subscript S after the square brackets is used to indicate a laminate that is symmetric about the mid-plane of a laminate.

These rules significantly condense the reporting of laminate stacking sequences and relatively thick laminate with a complex stacking sequence can be referred to without having to mention each lamina orientation individually. As an example: The MD2 laminate, which will be discussed shortly, has 13 plies with orientations alternating between 45°, -45°and 0°and is written as $[[\pm 45/0]_4/\pm 45]$.

For the discussion of CLT it shall be assumed that the constituents of each ply is of the same material with long fibres orientated uniformly in one direction. Furthermore the thickness and constituent volume fractions are equal for each ply. The most important limitation of CLT is that each ply is considered to be in a state of plane stress and that inter-laminar stresses are neglected (Gibson, 2011). With this assumption in mind the coordinate system for the laminate analysis may be defined. The global xyz coordinate system is used with the origin located on the middle surface of the laminate as shown in Figure 2.2. A local 123 coordinate system can however be defined for each ply which is aligned to the principle fibre direction of the material within the ply. With fibres in one ply orientated at an angle θ to the global coordinate system, the local coordinate system may be represented as shown in Figure 2.3. For a static analysis Whitney (1987) made 10 basic assumptions of which the most relevant for this discussion on CLT are:

1. The laminate consists of orthotropic laminae orientated in the xy plane.
2. The laminate thickness t is much smaller than the edge lengths.
3. The laminate thickness t is constant.
4. Each ply obeys Hooke's law.
5. Transverse shear strains γ_{xz} and γ_{yz} are negligible.

The stress-strain relationship for a lamina from elementary orthotropic mechanics theory is:

$$\begin{Bmatrix} \sigma_x \\ \sigma_y \\ \tau_{xy} \end{Bmatrix} = \begin{bmatrix} \bar{Q}_{11} & \bar{Q}_{12} & \bar{Q}_{16} \\ \bar{Q}_{21} & \bar{Q}_{22} & \bar{Q}_{26} \\ \bar{Q}_{61} & \bar{Q}_{62} & \bar{Q}_{66} \end{bmatrix} \begin{Bmatrix} \epsilon_x^0 + z\kappa_x \\ \epsilon_y^0 + z\kappa_y \\ \gamma_{xy}^0 + z\kappa_{xy} \end{Bmatrix} \tag{2.2.1}$$

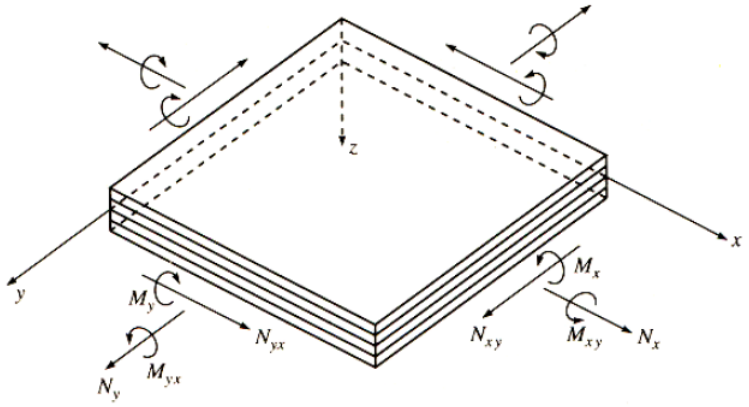

Figure 2.2: Laminate example with CLT coordinate system Gibson (2011)

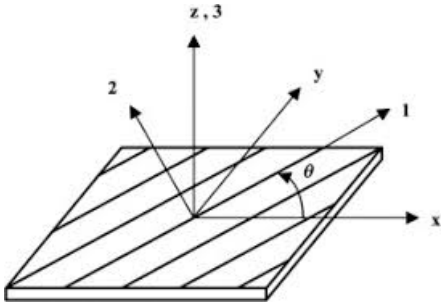

Figure 2.3: Local coordinate system at θ degrees from the global coordinate system Gibson (2011)

The equivalent to this lamina stress-strain relation for laminates is:

$$\begin{Bmatrix} N_x \\ N_y \\ N_xy \\ M_x \\ M_y \\ M_xy \end{Bmatrix} = \begin{bmatrix} A_{11} & A_{12} & A_{16} & B_{11} & B_{12} & B_{16} \\ A_{21} & A_{22} & A_{26} & B_{21} & B_{22} & B_{26} \\ A_{61} & A_{62} & A_{66} & B_{61} & B_{62} & B_{66} \\ B_{11} & B_{12} & B_{16} & D_{11} & D_{12} & D_{16} \\ B_{21} & B_{22} & B_{26} & D_{21} & D_{22} & D_{26} \\ B_{61} & B_{62} & B_{66} & D_{61} & D_{62} & D_{66} \end{bmatrix} \begin{Bmatrix} \epsilon_x^0 \\ \epsilon_y^0 \\ \epsilon_{xy}^0 \\ \kappa_x \\ \kappa_y \\ \kappa_{xy} \end{Bmatrix} \tag{2.2.2}$$

This relationship can be condensed into the partitioned form as

$$\begin{Bmatrix} N \\ M \end{Bmatrix} = \begin{bmatrix} A & B \\ B & D \end{bmatrix} \begin{Bmatrix} \epsilon^0 \\ \kappa \end{Bmatrix} \tag{2.2.3}$$

The response of a laminate subjected to a loading case can be solved using this relationship where the terms N and M are forces and moments in the global coordinate system and are defined per unit length. A, B and D represent the components of the lamina extensional- , coupling- and bending stiffness matrices respectively and are found on a per lamina basis using the following rules:

$$A_{ij} = \sum_{k=1}^{N} (\bar{Q}_{ij})_k (z_k - z_{k-1}) \tag{2.2.4}$$

$$B_{ij} = \frac{1}{2} \sum_{k=1}^{N} (\bar{Q}_{ij})_k (z_k^2 - z_{k-1}^2) \tag{2.2.5}$$

$$C_{ij} = \frac{1}{3} \sum_{k=1}^{N} (\bar{Q}_{ij})_k (z_k^3 - z_{k-1}^3) \tag{2.2.6}$$

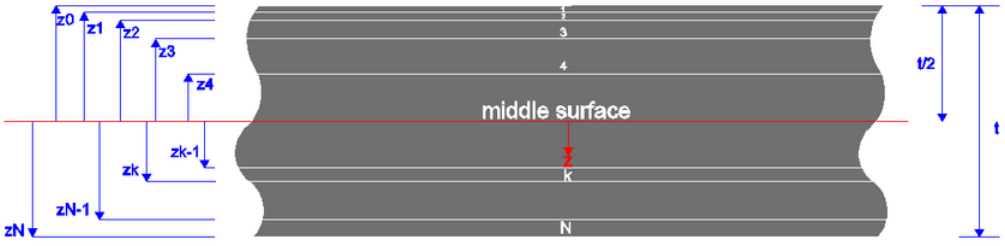

Figure 2.4: Laminate example with CLT coordinate system (Naderian *et al.*, 2017)

It is often the case that the applied loads on a laminate are known rather than the deformations and thus the inverted form of the laminate force-deformation relationships. When inverted, the stiffness matrices essentially become compliance matrices and. The relation simply becomes:

$$\begin{Bmatrix} \epsilon^0 \\ \kappa \end{Bmatrix} = \begin{bmatrix} A & B \\ B & D \end{bmatrix}^{-1} \begin{Bmatrix} N \\ M \end{Bmatrix} \tag{2.2.7}$$

To find the induced orthotropic stress state within a particular lamina in the laminate, the k$^{\text{th}}$ lamina, the following equation may be used.

$$\{\sigma\}_k = \left[\bar{Q}\right]_k \left(\{\epsilon^0\} + z\{\kappa\}\right) \tag{2.2.8}$$

Here z is the distance of the k$^{\text{th}}$ lamina from the middle surface of the laminate as defined by Figure 2.4:

2.3 Failure Criteria

To design a laminated FRP part, it is necessary to know what the safe operation loads of the part are. There is not a simple answer to this question, since multiple failure modes are possible for laminated FRPs and they often occur at the same time, failure criteria have been developed to define the regions of safe operation for a material.

A stress tensor of a specimen under axial loading orientated parallel to its principle axis, will not experience a stress in only the direction of the applied stress. A stress in the two transverse directions as well as shear stresses will most certainly be present and even if the greatest stress component is not close to the specified ultimate stress of the material, the interactions between these stresses may cause the part to fail. For this reason it is necessary to consider the effect of these stress interactions in failure analysis and the failure criteria discussed in this section, among many others, attempt to do this.

Failure criteria can be represented in a two-dimensional (2D) or three dimensional (3D) coordinate space known as a failure envelope. When a stress tensor is defined within the space of the failure envelope, the specific failure criterion predicts that the material will not fail at the location of the stress tensor. If the tensor is however defined outside the failure envelope boundaries, failure is predicted. For brevity the definitions and failure envelopes will be presented for the 2D, plane stress assumption only, but they can be easily expanded to the more general 3D versions. This section will discuss and illustrate the Maximum Stress (Jenkins, 1920), Maximum Strain (Waddoups, 1967), Tsai-Wu (Tsai and Wu, 1971), Tsai-Hill (Tsai, 1968) and Hashin-Rotem (Hashin and Rotem, 1973) failure criteria.

2.3.1 Maximum Stress and Maximum Strain

The maximum stress and maximum strain criteria provide the most elementary predictions of failure based on combining known ultimate stresses or strains in their respective directions. For the maximum stress and maximum strain criteria the borders of the failure envelopes are defined on the coordinate axes as the ultimate stresses and strains in the respective directions. The major shortcoming of these two criteria are that they do not take the interaction between stress or strain components into account.

Figure 2.5 and Figure 2.6 illustrate point cloud (3D spaces viewed in 2D) examples of such envelopes, while Equations 2.3.1 and 2.3.2 provide the mathematical definitions. In Equation 2.3.1 S_1 and S_2 are defined as the ultimate stresses along

the respective local coordinate axes and the subscripts t and c indicate the tensile or compressive direction. S_{12} is the ultimate shear stress. Furthermore, e_1 and e_2 are the ultimate strains and e_{12} the ultimate shear strain.

$$\begin{aligned} S_{1c} < \sigma_1 < S_{1t} \\ S_{2c} < \sigma_1 < S_{2t} \\ |\tau_{12}| < S_{12} \end{aligned} \tag{2.3.1}$$

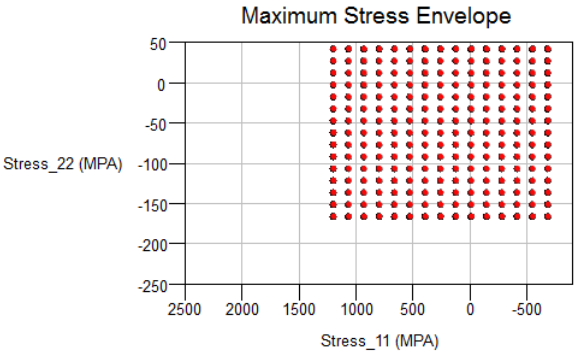

Figure 2.5: Maximum Stress failure criterion point cloud

$$\begin{aligned} e_{1c} < \sigma_1 < e_{1t} \\ e_{2c} < \sigma_1 < e_{2t} \\ |\gamma_{12}| < e_{12} \end{aligned} \tag{2.3.2}$$

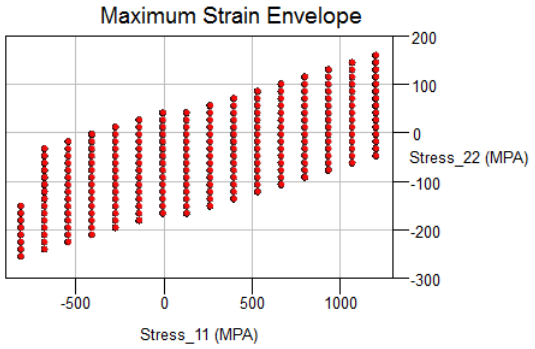

Figure 2.6: Maximum Strain failure criterion point cloud

2.3.2 Tsai-Hill and Tsai-Wu

The Tsai-Wu and Tsai-Hill failure criteria offer an improvement on the previously discussed failure criteria by including terms which account for interactions between the stress components (Gibson, 2011). Known as quadratic interaction criteria, the two examples discussed in this section have elliptical failure envelopes and quadratic terms in their definitions. The shortcomings of these two failure criteria are that they do not distinguish between matrix failure and fibre failure.

Figures 2.7 and 2.8 illustrate the failure envelopes for the Tsai-Hill and Tsai-Wu failure criteria respectively. Equations 2.3.3 for Tsai-Hill and 2.3.4 for Tsai-Wu show the mathematical definitions of the failure criteria where failure is predicted when the left hand side of the equation is equal to the failure index (FI), which in this case is equal to 1. The Tsai-Hill interaction terms, generally denoted F and not to be confused with force, in Equation 2.3.4 can be found in Kaw (2005) and many other sources of composite materials literature.

$$\frac{\sigma_1^2}{S_1^2} - \frac{\sigma_1\sigma_2}{S_1^2} + \frac{\sigma_2^2}{S_2^2} + \frac{\tau_{12}^2}{S_{12}^2} = 1 \tag{2.3.3}$$

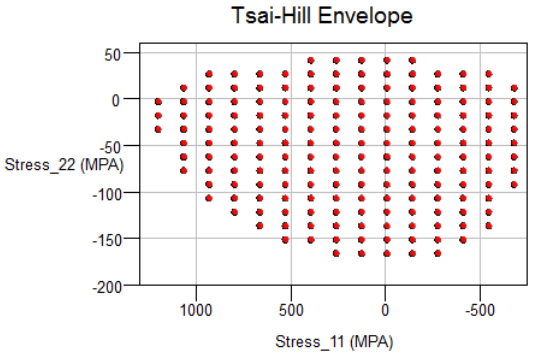

Figure 2.7: Tsai-Hill failure criterion point cloud

$$F_{11}\sigma_1^2 + F_{22}\sigma_2^2 + F_{66}\tau_{12}^2 + F_1\sigma_1 + F_2\sigma_2 + 2F_{12}\sigma_1\sigma_2 = 1 \tag{2.3.4}$$

2.3.3 Hashin-Rotem

The failure criterion proposed by 2.10 Hashin and Rotem (1973) distinguishes between matrix and fibre failure where matrix failure is governed by Equation 2.3.5

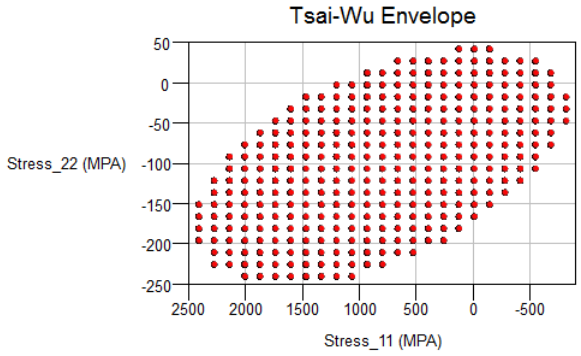

Figure 2.8: Tsai-Wu failure criterion point cloud

and fibre failure is governed by Equation 2.3.6. Figure 2.9 and Figure 2.10 shows the failure envelope in two orthotropic views. The reason for the one view being rectangular and the other elliptical, is because of the simplistic definition of matrix failure and the quadratic terms in the definition of fibre failure.

$$\frac{\sigma_1}{S_1} \tag{2.3.5}$$

$$\frac{\sigma_2}{S_2}^2 + \frac{\tau_{12}}{S_12}^2 \tag{2.3.6}$$

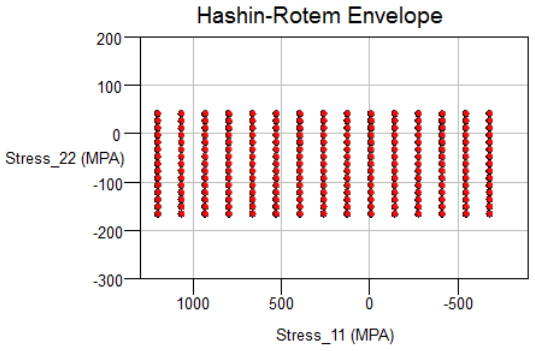

Figure 2.9: Hashin-Rotem failure criterion point cloud view 1

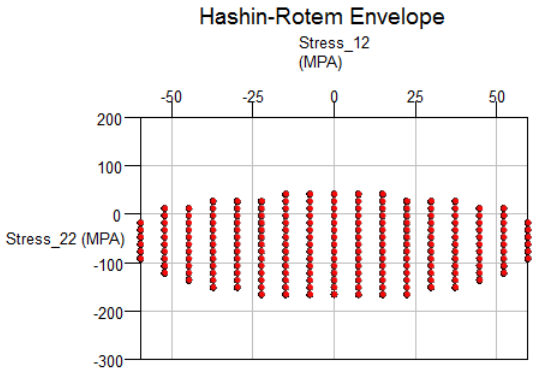

Figure 2.10: Hashin-Rotem failure criterion point cloud view 2

2.4 Fatigue of Composite Materials

As with all structural materials, FRPs experience a gradual decline in material properties when subjected to repeated loading cycles. Every material behaves uniquely to fatigue loading and it is therefore important to characterise the responses individually. This is especially relevant for laminated FRPs where each constituent material behaves differently under fatigue loading and the way in which these constituents interact directly affects the fatigue behaviour of the composite material.

Fatigue life for a particular material is typically reported on a S-N or Woehler curve which displays the amount of CA load cycles to failure on the X-axis and the load cycle amplitude at which failure occurs, referred to as the fatigue strength, on the Y-axis. Displaying fatigue failure results in this manner was first done by German railway engineer August Woehler (Schuetz, 1996). The load cycles to failure, despite being on the Y-axis, is considered the dependent variable and the fatigue strength is the independent variable (Gibson, 2011). Similar to homogeneous materials, FRP fatigue failure tends to be subject to a considerable amount of variation due to stress concentrations caused by surface defects and tiny imperfections within the material. Some metals display a noticeable limit at which the slope of the S-N curve tends to zero. This point is known as the fatigue or endurance limit. It has generally been accepted that such a limit does not exist for composite materials although relatively recent research efforts suggest that this might not be true for all composite materials (Nijssen, 2006*b*).

Failure due to fatigue loading in composite materials occurs as a combination of failure modes such as delamination, fibre failure, matrix failure and fibre pull-out

(Vassilopoulos and Keller, 2011), these failure modes contribute to ultimate failure in varying degrees depending on the material composition. Due to this statistical nature of fatigue, the drawing of a S-N curve requires numerous tests of material samples at the same R-ratio, but different load amplitudes. The ASTM E739 (2015) Standard suggests a minimum of 12 tests for an academic study and up to 24 for fatigue classification for materials in industrial use.

For a specific S-N curve, the ratio between the minimum and the maximum applied cyclic loads remain constant. This ratio can be described in terms of force or in the case of this study, in stress:

$$R = \frac{\sigma_{min}}{\sigma_{max}} \tag{2.4.1}$$

The amount of cycles to failure at each stress amplitude is noted and eventually a line can be drawn, typically on a log-log scale, to represent the fatigue behaviour of the material. S-N curves plotted on a log-log scale can be represented by a straight line with a steep slope representing materials with poor resistance to fatigue while the opposite is true for materials with flat S-N curves. The slope, m, of the line is described with the assistance of the S-N curve shown in Figure 2.11 and the equations described in Prenscia (2017).

$$m = \frac{1}{-b} \tag{2.4.2}$$

$$\log N_0 - \log N = \frac{1}{-b} \log \frac{S}{S_0} \tag{2.4.3}$$

$$N = N_0 \left(\frac{S}{S_0} \right)^{\frac{1}{-b}} \tag{2.4.4}$$

The OptiDat database (Nijssen, 2006*a*) is a collection of fatigue failure data from various laboratories across the world. Besides S-N curve related information for multiple common GFRP laminates at different R-ratios, the database also contains information on static material properties, testing equipment and specimen geometries. This information was used to determine whether testing would be feasible with the available equipment to the projects disposal. Furthermore, the fatigue failure data in the OptiDat database can be used to verify whether results from this project correlates to those of previous researchers. Table 2.4 shows the magnitudes of the slope variable b for S-N curves drawn for some standard GFRP laminates. This table will be referred to for comparison with the S-N curve which will generated by the specimen testing step of this project.

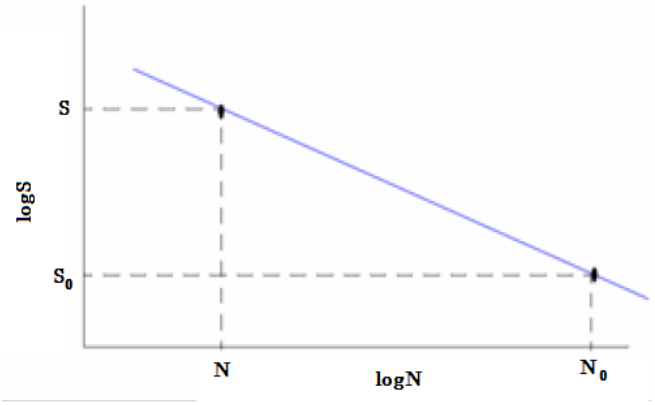

Figure 2.11: S-N curve for a material with a fatigue limit

Table 2.1: Slope variables for some of the GRP laminates within the OptiDat database. (Nijssen, 2006*a*)

Laminate	Name	Fibre	Resin	b
$[[\pm 45/0]_4/\pm 45]$	MD2	PPG2002	Prime 20, slow hardener	-10.87
$[[\pm 45/0]_4/\pm 45]$	MD4	PPG2002	LM-E6	-11.11
$[\pm 45]_5$	MD3	PPG2002	Prime 20, slow hardener	-10.98
$[0]_4$	UD2	PPG2002	Prime 20, slow hardener	-8.54
$[0]_7$	UD3	PPG2002	Prime 20, slow hardener	-11.90
$[0]_4$	UD4	PPG2002	LM-E6	-12.5
$[\pm 45/0_5/\pm 45]$	MUD	PPG2002	Prime 20, slow hardener	-11.90

2.5 Cycle Counting

Before testing may commence it will be necessary to determine the test conditions for the fatigue analysis. The RFC method is a convenient staring point for this as it is a procedure capable of counting variable amplitude load cycles in a time series in such a way that it is easy to translate into a CA equivalent. This involves decomposing a measured load sequence into elementary cycles characterised by unique means and stress ranges (Amzallag *et al.*, 1994). Depending on the preferred method, the metadata generated by RFC may be used to group cycles with similar ranges and means together in what is known as bins. With modern computational capabilities, binning is however not a necessary step.

The RFC method requires a time series monitoring of a single variable over time. This is usually generated as a two-column array with each time-step corresponding

to the recorded variable. Since, in the case of this project, the recorded variable is the bending strain experienced at the root of the fan blade, it is denoted $\epsilon(t)$. The first step of the RFC method is to locate only the local extrema (maxima and minima) of the $\epsilon(t)$ time series and eliminate all other data points. This is done by a one dimensional line search optimisation algorithm. The extrema are be isolated and arranged into i amount of peaks and troughs, $\epsilon(i)$. For demonstration purposes it is convenient to consider the time series as Matsuishi and Endo (1968) suggested by rotating the axes of the time series 90° clockwise. Following four point RFC method proposed by the ASTM E1049-85 (2003) Standard and imagining the time series as a series of pagoda roofs on a rainy day, streams of water that flow downward according to the set of rules mentioned below can be used to count and order cycles:

1. A stream starting at a peak will continue its flow downwards until it encounters an equal or more positive peak. Similarly a stream starting at a trough will continue downwards until it encounters an equal or more negative trough.

2. A stream ends when it encounters flow from a previous stream.

3. A new stream can not be started until the stream under consideration is ended.

4. A stream must end either when it encounters an equal or more positive peak or at the end of the time series.

5. The horizontal length of each stream is noted as the range and counted as one half-cycle.

6. To save computational time it should be noted that each peak-generated half-cycle will be matched by a trough generated half cycle. It is therefore acceptable to analyse only peak- or trough-generated half cycles and assume each to be a full cycle. (Wirsching *et al.*, 2006)

To illustrate this method consider the example of series of minimum and maximum bending moments shown in Figure 2.12. Rule 6, discussed above, will be implemented in the analysis and only trough-generated half-cycles will be considered when the plot is rotated as shown. The stream starting at point 1 flows down until it reaches a more negative trough than its origin and rule 1 is enforced. This stream moves from one negative (point 1) to one positive (point 4) and is therefore counted as a half-cycle. The stream starting at point 3 is terminated by rule 2 when it encounters another stream. This stream is also counted as a half-cycle.

The procedure is continued until all trough generated half-cycles are counted. Finally the cycles may be arranged into bins of similar load range. The amount of cycles in each bin can be doubled according to rule 6.

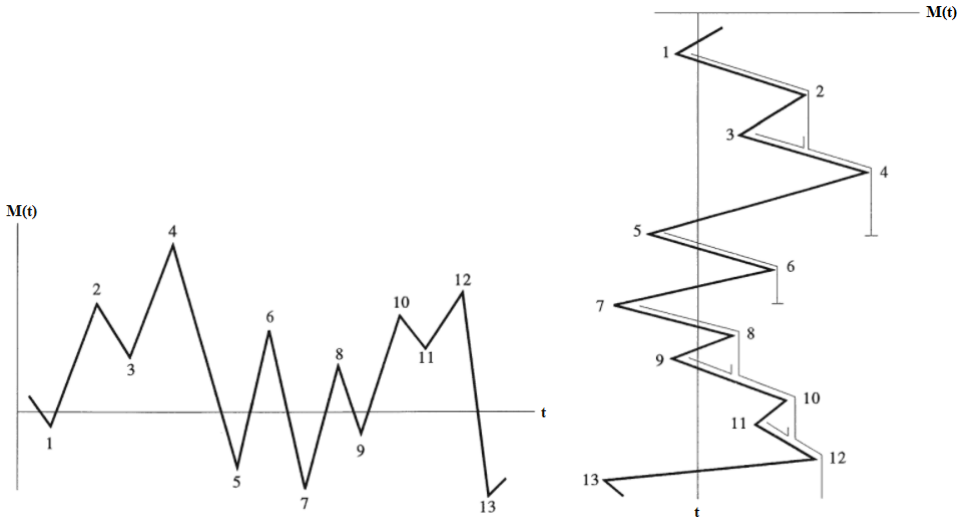

Figure 2.12: Wide-band time series plot for rainflow count illustration

Similar to the method used for dual axis fatigue testing of large wind turbine blades, RFC can be applied for loads in the flap- and lag-wise directions. The output of the rainflow counting operation is a three dimensional array of load ranges, the mean of each range and a corresponding half or unit cycle counts. The amount of cycles per load range can be used in a damage summation such as Palmgren-Miner summation to calculate the overall damage caused by the loading sequence. Information about the range means may be used to assist in the choice of an appropriate overall applied stress and stress ratio. The objective is to use the RFC generated metadata to choose a CA loading sequence that will most accurately model the variable loads of service life. The next section will discuss methods of quantifying fatigue damage in composite materials.

2.6 Fatigue Damage Modelling

Current approaches to fatigue characterisation and modelling can be grouped into six categories discussed in the Chapter 1. This section will discuss the most rele-

vant methods within from these categories.

2.6.1 Palmgren-Miner Summation

S-N curve based fatigue life models consider the amount of cycles to ultimate material failure. This classification of modelling provides intuitive predictions for material behaviour since, when considering fatigue loading, the question of "how long will it last?" often arises. Fatigue life models are able to provide a straight answer to this question.

The most common and simple approach to fatigue life modelling are cumulative damage methods of which the Palmgren-Miner damage summation is the most well known. This approach was originally developed for predicting the progression of damage for homogeneous materials, but is still frequently applied for composite materials Post *et al.* (2008). The Palmgren-Miner damage summation, or Miner's sum, is able to take into account a variable amplitude loading sequence and calculate the amount of relative damage each cycle contributes to ultimate failure. Equation 2.6.1 shows the fundamental Miner's sum where n_i is the amount of load cycles that occur at a specific amplitude and N_i is the amount of cycles that the material can withstand until failure at that amplitude. The result of the Miner's sum , D, is a unitless damage parameter where a value of one indicates ultimate failure (Greaves *et al.*, 2012). Sometimes, however, it is sensible to include a safety factor in the Miner's sum for a more conservative prediction and the value of the damage parameter may be made smaller than 1.

$$D = \sum_{i}^{m} \frac{n_i}{N_i} \tag{2.6.1}$$

Given that all cycles occur at the same R-ratio, Miner's sum can easily be used with the assistance of the traditional fatigue life, or S-N, curve. Rainflow counted loading data can simply be entered into the n_i variable of the Miner's sum and the S-N curve will provide the value for N_i. The damage sum can then assist in finding an accelerated CA load cycle to model the damage caused by the variable in-service loads.

Shortcomings of damage modelling with Miner's sum are that it requires S-N curves at various different R-ratios. This may be difficult to obtain for FRP materials where not only the specific material composition, but also the ply stacking sequence determines the material properties. A load sequence recorded during in-service operation will almost certainly not have a constant R-ratio and thus a

Miner's sum prediction based on a single S-N curve will be a loose approximation. ϵ-N curves solve this problem to some extent since the material strain is far less dependent on fibre orientation. Recent collaborative research efforts have led to the formation of the DOE/MSU database for fatigue data on FRP materials. Another issue with Miner's summation is that it returns the same result independent on the order of load cycles. This is a problem since it is known that certain broad spectrum loading sequences lead to more rapid failure when the cycle order is manipulated. Miner's sum and even its non-linear adaptations generally under-predict fatigue life in composite materials sometimes by more than an order of magnitude (Post *et al.*, 2008).

An important consideration when using the PM Summation is that the damage progression that is reported is merely a linear progression towards failure. The straight line produced gives little information about how the material properties and damage parameters change. For this reason it is good to supplement any predictions made by Miner's summation with a more sophisticated method that records some material properties. There are numerous adaptations of Miner's sum in existence that try and compensate for its shortcomings. Despite these shortcomings fatigue life modelling still remains the most popular method of damage modelling and will also be applied in this study.

2.6.2 Stiffness Degradation

While an S-N curve is a good way of reporting the fatigue behaviour of a material, it requires destructive testing to determine a when a material will fail and is not suitable for monitoring the progression of damage in a structure of which there may only be a single specimen available. It may be important to know the progression of damage to a structure for maintenance purposes without having to test it to failure. This obstacle is overcome by using phenomenological residual stiffness or strength models that include damage metrics which determine the progression of material fatigue by means of indirect and non-destructive testing methods.

Of these non destructive metrics, stiffness and absorbed mechanical energy seem to provide the most convenient measures of damage progression. Giancane *et al.* (2010) completed a study on the progression of these metrics during the fatigue lifetime of E-glass laminates. The results along with an accurate model for damage progression proposed by Mao and Mahadevan (2002) provide good reason to implement their methodology into this study. All material damage models are based on the notion that each cycle in a fatigue loading sequence causes a certain amount of degradation in the material properties. Stiffness degradation is easily

measured by direct and indirect methods and seems to be the most suitable of the two mentioned damage metrics when material property decay is considered. Composite material stiffness is not simply another term for Young's Modulus, but may refer to either flexural, coupling or axial stiffness. In this study, dynamic stiffness shall be measured during a fatigue test in the same way as Young's Modulus, but since the method does not make use of an accurate measurement device like an extensometer and grip tab displacement may also be measured, the measured data will only be relative to previous measurements in the same test and will simply be referred to as stiffness.

The typical decay of stiffness under fatigue loading is illustrated on the stiffness degradation curve in Figure 2.13. According to Schulte (1993) three distinctive stages of damage can be identified in the typical stiffness degradation curve for composite materials:

- Stage I: 2 to 5 % of the stiffness is lost rapidly in this initial stage. The reduction in stiffness is primarily due to the development of transverse cracks in the matrix.
- Stage II: 1 to 5 % of stiffness is lost and a gradual, almost linear decay can be observed. Longitudinal cracks in the fibres and edge delamination are the causes for further stiffness reduction.
- Stage III: Stiffness degradation happens rapidly when delamination occurs and fibres start breaking.

The axes in Figure 2.13 are normalised and the value of normalised relative stiffness $\frac{E}{E_0}$ is referred to the modulus reduction ratio (MRR) by Whitworth (1997). This metric shall also be used in this project to present normalised relative stiffness results.

In their research, Cadavid *et al.* (2017) noted that the stiffness degradation for GFRP laminates was greatest at a stress ratio of $R = 0.1$. This was witnessed for both 0° and 90° laminates. These researchers observed very rapid stiffness degradation and propose an exponential model that captures only the first two stages of stiffness degradation. This model is attractive from a maintenance perspective, because the third stage of stiffness degradation can effectively already be considered as material failure. One of their model curves, illustrated in Figure 2.14 with curve fitting constants $K = 0.846$ and $n = 0.0186$, is described by the equation:

$$MRR = \frac{E}{E_0} = K\frac{N}{N_f}^{-n} \tag{2.6.2}$$

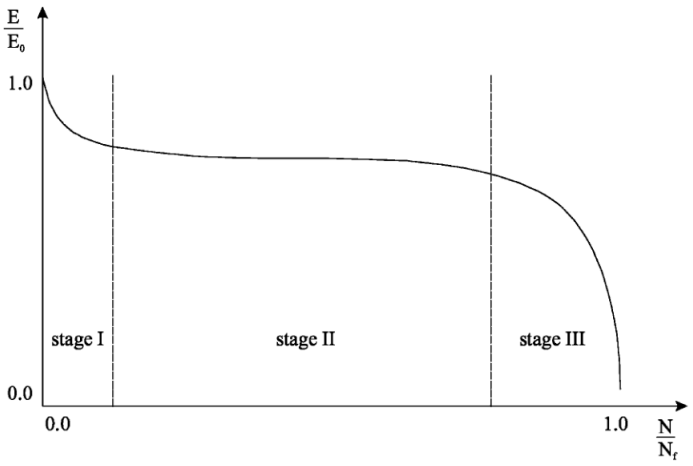

Figure 2.13: Typical FRP stiffness degradation curve Schulte (1993)

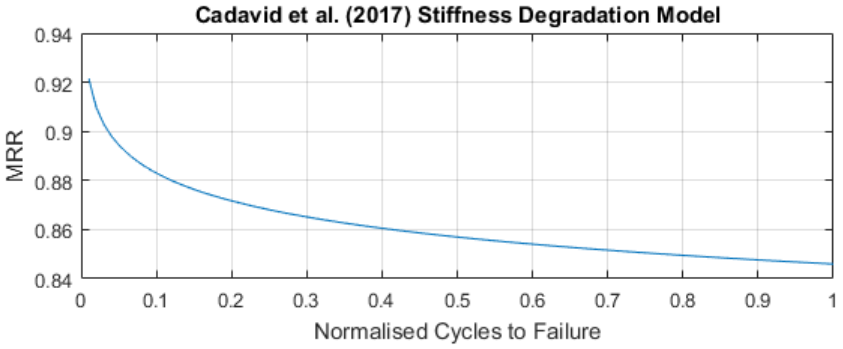

Figure 2.14: Cadavid stiffness degradation model

The stiffness of a large structure, such as the fan blade in this research project, which cannot be laboratory tested in a conventional universal testing machine, is somewhat more complicated to obtain. Here an indirect method can be implemented where the structure's vibrational responses can be used as an indication of stiffness degradation. A fan blade fixed to a rotor hub can be simplified as single degree of freedom (SDOF) cantilever beam with the natural frequency in the direction perpendicular to the length of a cantilever beam:

$$\omega_n = \frac{1}{2\pi}\sqrt{\frac{3EI}{\left(0.2235\rho L + m\right)L^3}} \tag{2.6.3}$$

An experimental modal analysis (EMA) by Els and Muiyser (2016) has yielded information about the mode shapes and natural frequencies of the fan blade. The EMA was done by applying accelerometers to the fan blade and then exciting the structure with a modal hammer. The accelerometers track the dynamic responses of the structure to excitation forces and produce a Frequency Response Function (FRF).

The material life of the fan structure can be monitored by performing a simplified version of the EMA done previously at predetermined service intervals. If it is assumed that the only time-variable properties in Equation 2.6.3 (Inman, 2013) are ω_n and E, a decrease in the first natural frequency must indicate a corresponding decrease in stiffness. The material health of the structure can be monitored in this way by performing this analysis often enough to be able to draw a curve similar to Figure 2.13. Since failure due to material fatigue is progressive rather than instantaneous, a set-up of criteria will have to be decided upon determine when the structure will be regarded to have failed. More research in this regard will be required to before it is possible to propose a point of failure, but a good guess is that the transition region between stage II and stage III may be considered as the point where safe operation can no longer continue.

Chapter 3

Methodology

This project is split up into three sections namely problem analysis, modelling and experimentation. The steps taken to address the objectives of this study is discussed within these sections. This chapter, therefore explains the steps taken, and reasoning behind these actions.

The chapter will commence with explaining the data processing step in which the loading data, which is the input to this study, is refined and converted from bending moments to strains. This data is then rainflow counted and an accelerated constant amplitude test is formulated. A rough prediction of fatigue damage is also made based on the simple Palmgren-Miner summation.

A simplified beam to simulate the fan blade root was developed to have full control over information like the constituent materials, stacking sequence and geometry of the structure. This structure was designed using FEA software based on the available information of the fan blade dimensions static properties. Test specimens from of the same laminate were manufactured for material and fatigue testing.

The material fatigue tests, also referred to as the specimen fatigue tests, are discussed in this chapter and the S-N curve generated from this test is reported in the upcoming Results Chapter. This accelerated fatigue testing is be done at a single R-ratio that will be chosen based on information gathered from the in service testing data and literature. During these tests, stiffness degradation measurements are taken and are intended to be used in a model to predict stiffness degradation under given load application amplitudes and R-ratios. The predictive ability of the stiffness degradation model is then tested on the full-scale equivalent structure of which The laminate was designed with the assistance of FEA software.

Finally, stiffness is recorded by monitoring the vibrational response of the struc-

ture and therefore the chapter will be concluded with a section on the set-up of an experimental modal analysis.

3.1 Problem Analysis

3.1.1 Data Processing

A previous analysis by Els and Muiyser (2016) has produced a time scale torsional and bending moment history in the lag-wise and flap-wise directions of the fan blade during operation at Matimba Power Station. These bending moments were then translated to material strains and then to stresses using given translation coefficients based on the fan blade geometry. Six of these analyses were conducted over a space of three days in which the conditions ranged from a light breeze to a strong wind. These stresses represent components of 2D stress tensor which, when a state of plane stress is assumed, can be translated to principle stresses and strains using Mohr's circle.

The first step in the translation from the general coordinate system is to determine the average principle stress. This is done by applying the following equation:

$$\sigma_{avg} = \frac{\sigma_{FW} + \sigma_{LW}}{2} \tag{3.1.1}$$

Then the radius of the Mohr's circle is:

$$\sigma_r = \sqrt{\frac{\sigma_{FW} - \sigma_{LW}{}^2}{2}} + \tau_{tors}^2 \tag{3.1.2}$$

The major principle and minor principle stresses are found respectively by:

$$\sigma_1 = \sigma_{avg} + \sigma_r \tag{3.1.3}$$

$$\sigma_2 = \sigma_{avg} - \sigma_r \tag{3.1.4}$$

and finally the stress rotation angle:

$$\theta_1 = \arctan \frac{\tau_{tors}}{\sigma_{FW} - \sigma_{avg}} \tag{3.1.5}$$

Using these relations, a Mohr's circle can be generated for each increment in the time series. Figure 3.1 illustrates such a Mohr's circle at a random time step during one of the tests.

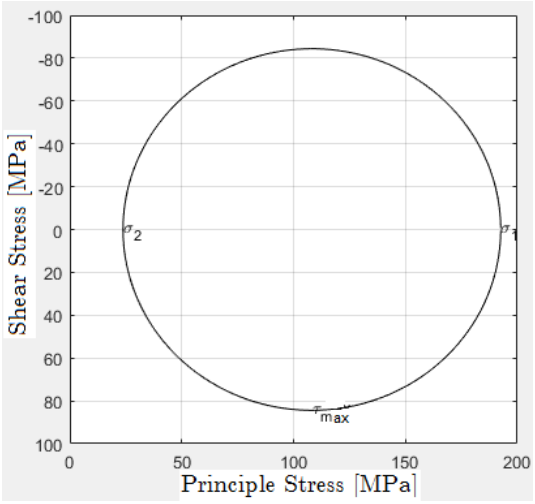

Figure 3.1: Mohr's circle for stress transformation

The transformed stresses from this analysis are used in further calculations of loading on the fan blade or equivalent structure.

The initial time-series loading data sets featured sections of drifting and erroneous data which required trimming before analysis could commence. The trimming operation is simple when the section of bad data is located at the beginning or end of the time-series. A visual inspection of the plotted data yields a good idea of where the data transitions from good to bad. These transition points can then simply be assigned as the new first or last integer in the data set index depending on the location of the bad data. A slightly more complex operation is required for trimming a section which does not lie at one of the extremities of a data set. Here visual inspection of MATLAB's ginput function is once again the first step, but it is followed by a step in which the indices of the data is determined. This is necessary because the time-scale does not always start indexing at zero. After the index has been determined the data may be trimmed once again by splitting the good data into separate arrays and assigning new indices to the arrays such that there are no discontinuities when they are eventually merged into a single array of only good data.

3.1.2 Damage Estimation and Specimen Test Formulation

After the data is filtered and converted into a more useful form of stresses and strains, the cycle count, organised in bins with similar amplitude ranges and means,

is extracted with the aid of the RFC algorithm. The RFC function within the HBM Prenscia (2017) nCode software package implements the rainflow count algorithm discussed in the Chapter 2 and is used to count the cycle peaks within each time series data set. The cycle peaks and troughs are essentially what this study is interested in and this is used for the calculation of statistical properties. Of primary interest when looking at these properties is to decide which dataset represents the most damaging conditions are of the available datasets. This dataset shall then be considered as the operating conditions to which a CA equivalent test will be designed.

To determine the severity of each dataset, a rainflow count on the stress time-series and Palmgren-Miner damage analysis is performed following the methods explained in Section 2.5. The damage summation is based on the S-N curve for a standard UD E-glass laminate and not the actual laminate used in the fan blade. A generic E-glass laminate was used since the laminate was not yet designed at this stage, and the fatigue slope variable b is similar for all E-glass GRPs. This analysis is however still acceptable at this stage, since the current objective is only to determine which of the datasets will induce the most damage relative to the others and actual induced damage is not of critical importance.

When considering the data, the problem arises that none of the datasets are equal in duration or number of cycles and it would therefore not be meaningful to simply look at the induced damage over the duration of the time-series. A simple solution is to calculate the damage induced by the time-series per unit of time. This damage over time result can then be used to determine the estimated damage per hour and acts as a normalised value for all datasets. For more intuitive representation and comparison the reciprocal of the damage per hour result may be taken to find the estimated lifetime in hours of the material. When comparing the predicted estimated lifetimes of each dataset in Table 3.1, it can be seen that datasets 2a and 2b represent the most severe conditions and will be regarded to represent the conditions closest to the worst case scenario. The integer in the dataset name indicates on which day of testing the data was collected and the letter indicates which of these tests were conducted before the other.

The methodology used to determine a CA accelerated material test from variable amplitude data is based on literature provided by HBM Prenscia (2017). This approach involves defining a constant amplitude equivalent load at a higher amplitude, but at the similar R-ratio than the original data. A decision was made to select and amplify the worst case scenario from the gathered data. Table 3.1 indicates that tests 2a and 2b induced the most damage and the metadata summary in Table 3.2 confirms this with test 2b clearly having the worst case R-ratio and

Table 3.1: Life estimations of each recorded dataset

Dataset	Life in Hours
1a	1.4721×10^{14}
1b	3.5361×10^{14}
2a	1.1131×10^{12}
2b	1.4331×10^{12}
3a	1.4741×10^{13}
3b	3.6351×10^{13}

Table 3.2: Metadata summary for each recorded dataset

Dataset	Mean Stress [MPa]	Standard Dev. [MPa]	Mean Resultant Angle [deg]	Standard Dev. [deg]	Worst Case R-ratio
1a	23.69	0.73	14.75	0.41	0.40
1b	23.66	0.73	13.97	0.43	0.54
2a	26.23	1.24	13.26	0.63	0.19
2b	26.47	1.50	13.4	0.64	0.10
3a	23.07	1.03	14.99	0.64	0.23
3b	26.13	1.15	13.39	0.66	0.28

highest mean stress.

Figure 3.2 shows the RFC density plot of the worst case dataset and the RFC density plot of the proposed cycle for accelerated testing. The second plot shows where a single accelerated cycle would be located in the coordinate space relative to the maximum recorded stress cycle. From the horizontal dashed line that indicates the R-ratio of 0.1, it can be seen that the test loads occurred very close to this ratio and that R = 0.1 would be a good approximation for an accelerated test.

3.2 Structural and Material Modelling

Finite Element Analysis software was used as a design tool to model a selected equivalent structure and to find the material that would satisfy the strength requirements based on laminate failure criteria. This section discusses the steps taken to build and analyse the model.

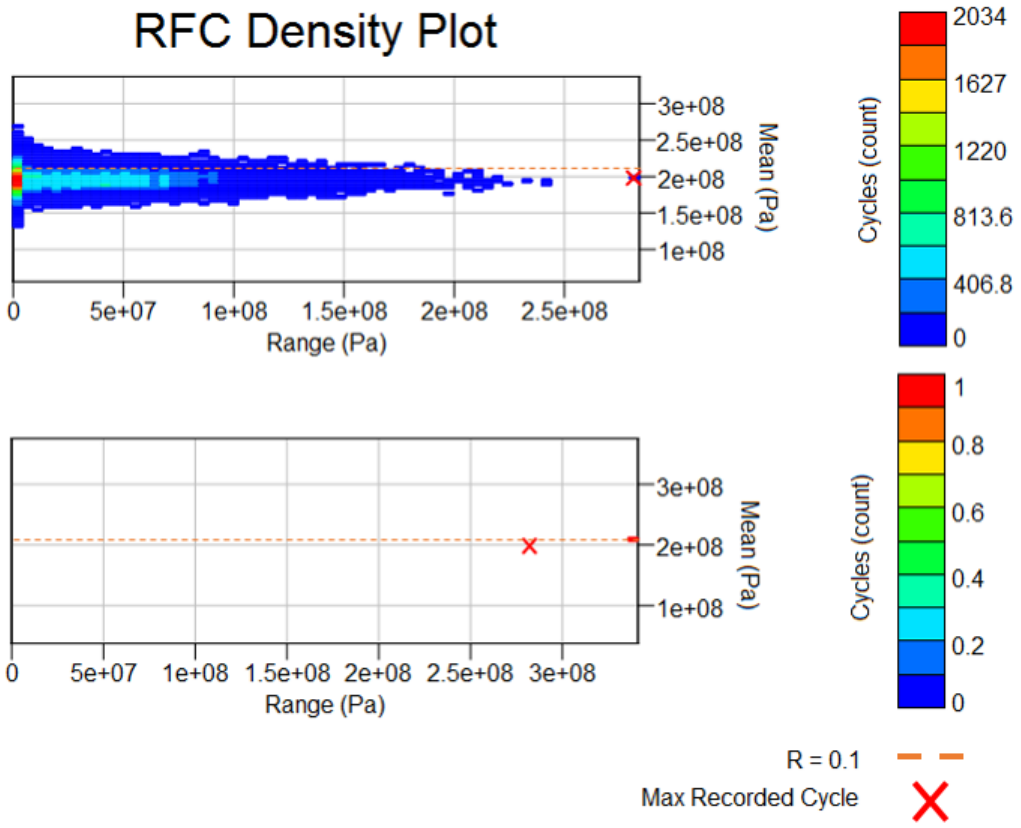

Figure 3.2: RFC with R = 0.1 load and accelerated amplitude indicated

3.2.1 Equivalent Filament Wound Structure Selection

Based on the information gathered by Els *et al.* (2018), the maximum static bending moment in a single direction on the fan blade root is 14 kNm. The approximate diameter, natural frequencies, approximate material constituents and boundary conditions were also known. This information was used to design a simplified beam to model an alternative system which can approximate the actual fan blade.

Due to practicality and cost efficiency it was decided that the proposed structure should be cylindrical, could not be longer than 1.6 m and that the diameter should be similar, if not approximately equal, to the octagonal cross-section of the original fan blade root. Many potential manufacturers were contacted to produce such a structure and initially the intention was that a cylinder could be made in the same process as was used to manufacture the fan blade root, which is by laminating woven resin pre-impregnated (prepreg) glass-epoxy sheets together according

to the specifications of the FE model. Feedback from the manufacturers indicated that this manufacturing method would be complicated and expensive for a one-off manufacture, but above all that the expected vs actual strength of the structure would likely be very different due to a discontinuity in each ply along the boundaries where the sheets are cut. After investigating manufacturing methods, filament winding proved to be the most realistic, affordable and predictable manufacturing method.

Filament winding as a manufacturing method for GRP which offers an alternative to conventional prepreg or resin infusion manufacturing processes. This method is most often used to manufacture cylindrical structures such as pipes and pressure vessels. Unlike the other manufacturing methods, filament winding uses continuous fibres which are wound in successive layers in different orientations. This means that filament winding produces no fibre discontinuities which should theoretically lead to the expected vs actual strength of the structure to be similar. One major drawback of filament winding is that the fibres cannot be wound at 0° to the lengthwise axis of the cylinder. The smallest angle that can be reached is 2°, but this leads to some overlapping of fibres which creates a very thick lamina. Similarly, fibres cannot be wound at 90° to the lengthwise axis of the cylinder. This is because the fibres are wound along the lengthwise axis of the mandrel and a winding angle perpendicular to that axis would make winding impossible. A recommendation was made by the manufacturer that 7° should be used as the smallest angle to the lengthwise axis since the it would aid manufacturing speed, and would also produce a more realistic ply thickness compared to the other plies. Because the cosine of a small angle yields a value close to that of the cosine of 0°, the smallest fibre angle of 7° approximates a 0° laminate sufficiently.

Another limitation of filament winding is that, due to the way in which the fibres are wound around the mandrel, laminae can only occur in cross-ply pairs with alternating signs. This means that a single +7° ply, cannot be followed up by plies of some arbitrary orientation, and that it can only be followed up by a -7°ply. The implication of this is that laminates created by filament winding can never be symmetric about the neutral axis and care should be taken in the analysis. Concerns were initially raised about the whether the material could still be accurately analysed with CLT, but Hernandez-Moreno *et al.* (2008) and Xia *et al.* (2001) confirmed that CLT analysis does still produce consistently accurate results for filament wound materials.

3.2.2 Geometry and Coordinate Systems

Greaves *et al.* (2012) suggest the formulation of a simplified analytical model to determine the points of maximum bending stress concentrations and major stress discontinuities. Due to the non-availability of dimensional specifications a numerical model will be based on a simple cantilever beam set-up with minimal complications. A previous analysis by Els and Muiyser (2016) of the fan blade's behaviour under static loading has already yielded a good indication of where stress concentrations are most critical in the flap-wise direction. This provides a good entry point for a Finite Element Analysis (FEA) of the problem.

The objective of a FEA done in Patran with Nastran solver (MSC, 2016) is to analyse an induced static bending moment of 14 kNm at the root of the cantilever modelled beam and to post process the stress results using various composite materials failure criteria. A 1600 mm long hollow cylindrical beam with a constant circular cross section was designed. The beam has an inner diameter of 160 mm and a wall thickness of 11.1 mm which brings the oter diameter to 182.2 mm. The inner diameter dimension is a constraint imposed by the filament winding manufacturing process since it is the outer diameter of the mandrel around which the fibres are wound. The beam is entirely cylindrical, and a first local cylindrical coordinate system, referred to as coord1, was therefore created to reference all geometries and results to. Coord1 is referenced to the global coordinate system, referred to as coord0. The geometry of the beam with the first local coordinate system and global coordinate system is shown in Figure 3.3. an understanding of the coordinate system transformations is important to for when results are reported since the software calculates results in coord0 but upon user request interprets the results to coord1. Since a composite laminate will be defined as the material in a subsequent step, note should be taken that each of the lamina within the material will have its own second local coordinate system. When exported for post-processing, the static FEA-generated results are exported relative to coord0 and are interpreted on a per-lamina level in the respective second local lamina coordinate systems.

3.2.3 Mesh Convergence Study

The Nastran isometric mesher was used with Quad 4 surface elements of 21.25 mm$\times$ 25 mm for the entirety of the beam's length. The dimensions of these elements were established by doing a mesh convergence study. The results from this exercise are shown in Figure 3.4 and show how the increase in density of Quad 4 elements on the surface of the model influence the convergence of results. Three materials namely an aluminium sheet of 1.6 mm, [0/90] and $\pm$[45] glass GRP laminates were

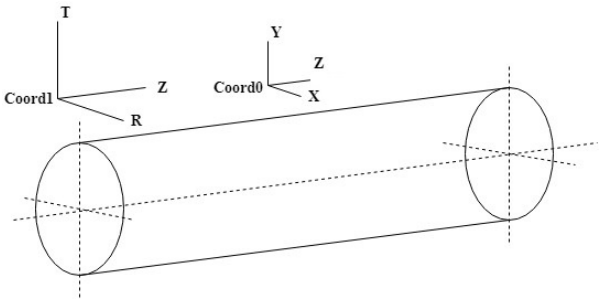

Figure 3.3: Beam geometry within cylindrical coordinate system

applied to the model and the maximum tip displacement was analysed at a 1 kN point load under cantilever clamped boundary conditions. The aluminium sheet was chosen to verify whether the mesh convergence would behave differently for a homogeneous material than for a laminate. From Figure 3.4 it can be observed that the maximum displacement results tend toward an ultimate accuracy and from this it is possible to select a mesh density that provides the best compromise between computational time and accuracy. The mesh density eventually chosen represents the third point on the curves with 1440 Quad4 elements. The Mesh seed was done to place 24 elements around the diameter of the beam and 60 elements along the length.

3.2.4 Boundary Conditions

The modelled boundary conditions are based on the actual clamping conditions and the eventual full scale test that will be performed on the cylindrical beam using already existing clamping fixtures and testing machinery. The intention is to clamp the beam at the one end with two brackets and to apply a point load to the other end. This essentially models a cantilever beam with the bending moment $M(x)$ expected to increase linearly as shown in Figure 3.5 until it reaches a maximum at the clamping point. The point load will be applied to a circular bracket at the free end of the beam and a solid cylindrical block will be inserted into the clamped end to protect the material from collapsing under the clamping pressure. This set-up will be discussed in more detail in the Full-Scale Testing section.

The circular clamps are modelled as a displacement constraint in coord1 as two rings around the beam that fix all six degrees of freedom. The reason for this simplification is that the rigid cylindrical block that will be inserted in to the clamped end of the beam is expected to resist displacements and rotations in the unconstrained region between the clamps. These clamping displacement constraints are

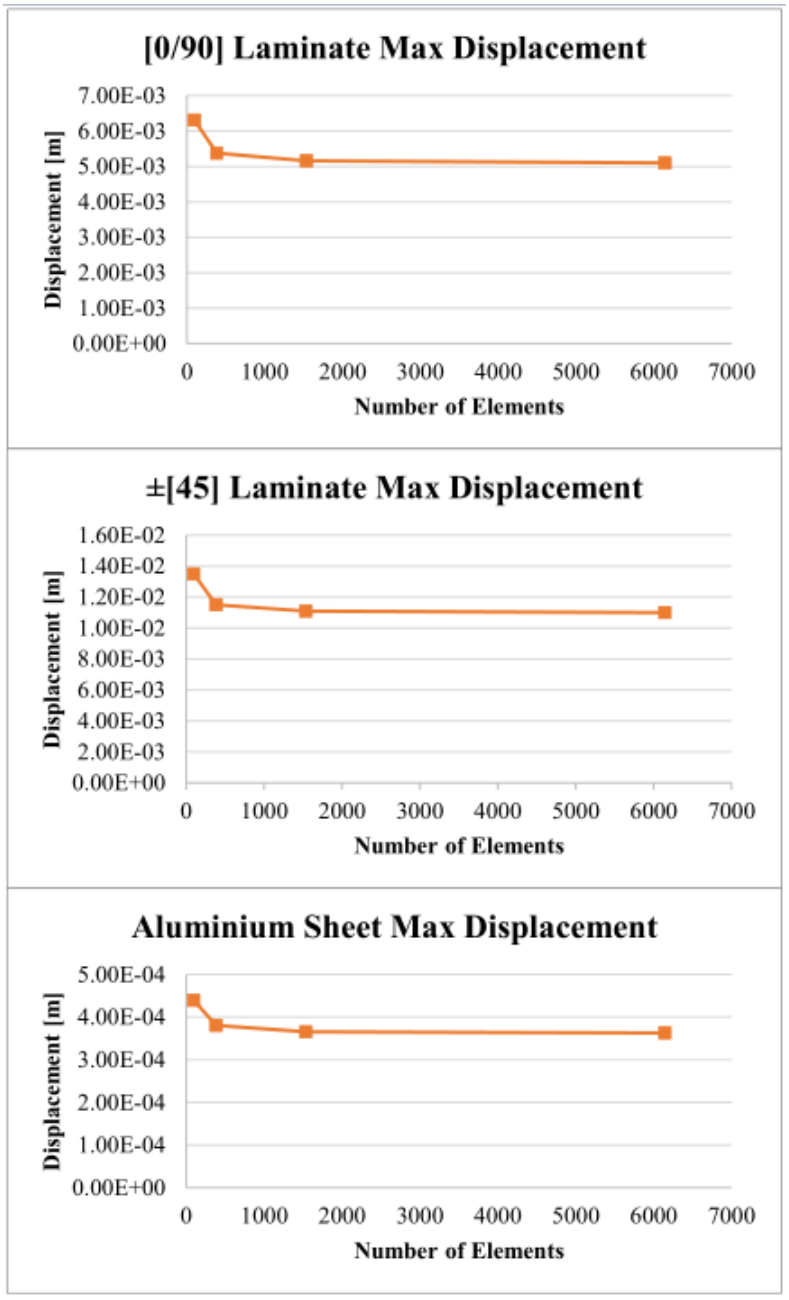

Figure 3.4: Mesh convergence study for [0/90], ±[45] GRP and aluminium plate

located 175 mm apart just like the clamps on the intended fixture. To model the application of a point load to a bracket on the free end of the beam, a multipoint constraint (MPC) is used by applying a scalable unit load to a node located on the

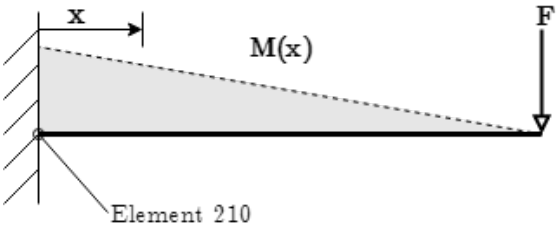

Figure 3.5: Bending moment diagram for a simply loaded cantilever constrained beam with the maximum stress element 210 shown

centre axis at the end of the beam. This node is constrained to all nodes on the free edge by means of rigid body elements (RBE2) also fixed in all six degrees of freedom. The argument here is that, due to Saint-Venant's principle, the simplification merely provides means of inducing a point load and that the effect of any inaccurate stress concentrations have a negligible influence on the area of interest due to it being sufficiently far enough removed from the clamps.

3.2.5 Material Modelling and Selection

Although applied to the model in an earlier step, the discussion about the application of the material to the model has been delayed since it is the property that is varied in the iterative design process. In the actual set-up of this FE model, the material application step follows directly after the geometry definition, but it is altered after each analysis to obtain the intended strength. A 2-dimensional orthotropic material was created within the FE design space. The material properties entered are typical E-glass properties obtained from the HBM Prenscia nCode and CES EduPack Material databases and are shown in Table D in Appendix D.

The objective for this iterative design process was to find a laminate that firstly fails under a load of 14 kN/m, is secondly manufacturable with filament winding and that is finally based on a standard stacking sequence. This last criterion was used as a departure point in the analysis and the known stacking sequences discussed in the first column of Table 2.4 were defined in the analysis software along with a $[0/90]_s$ laminate and a $\pm[45]_s$ laminate. These laminates were then applied one-by-one to the FE model and a linear-static analysis was done at at a point load of 10 kN at 1.4 m from the first clamp which induces a maximum of 14 kN/m bending moment to the beam. Each node in the FEA output file has n number of results associated to it, where n is the number of plies for the laminate being analysed. As previously mentioned, the results can easily be requested in coord0 or

coord1, but results in the local lamina coordinate systems could not be requested that easily. Results in these local lamina coordinate systems are important for a per-lamina failure analysis using composite materials failure criteria to determine at which node, and in which ply the material is likely to fail first.

The FE results files for each laminate analysis were post processed with HBM Prenscia nCode to identify the failure indices according to multiple failure criteria. This post processing step involves performing a tensor transformation as explained in Chapter 2 for all of the nodes in each of the n number of plies. Once this is done, a static failure criterion can be applied to each transformed stress tensor to determine whether or not the failure index of the specific criterion has been exceeded (FI $>$ 1) or not (FI $<$ 1). The failure criteria selected for the analysis were the Maximum Stress, Maximum Strain, Tsai-Hill, Tsai-Wu and Hashin-Rotem Criteria. These five failure criteria were chosen for the sake of completeness, but the intention was not to use Maximum Stress or Maximum Strain for further analysis because of the shortcomings discussed in Chapter 2. Tsai-Hill, Tsai-Wu and Hashin-Rotem provide slightly more conservative predictions of failure. The advantage of using the HBM nCode software is that the results file for each FEA could be applied to more than one failure criteria simultaneously. Moreover, the capabilities of the software allow for a 3D failure envelope which means that not only the normal 11 and 22 stresses can be analysed and displayed, but also the 12 shear stress in the same coordinate space. This created for a more realistic representation of the actual state of stress at each node as opposed to a more elementary 2D failure envelope.

From this analysis, the MUD laminate with a $[\pm 45/0_5/\pm 45]$ stacking sequence displayed a FI closest to unity out of all the laminates that was analysed. This result indicated that the MUD laminate would be the laminate upon which the next step could be applied by firstly changing all 0° plies to $\pm 7°$ and then iteratively adding more plies until an FI close to 1 was reached in post-processing. The post-processing analysis was done by multiplying the initial input point load of 10 kN incrementally with scaling values from 1 to -1. This simulated the application of a cyclic load between 14 kN/m and -14 kN/m which was then applied to each material iteration of the beam. For the material to be considered suitable, failure of the beam would need to be predicted at this maximum and minimum bending moment. Each of the selected failure criteria was applied to each node for each of the n amount of plies. This generated five FI values for each node and the greatest of these values was considered the worst case-scenario. The Tsai-Wu criterion proved to be the worst case scenario for almost all of the nodes across all tests. This suggested that Tsai-Wu is the most conservative failure criterion which in this case, where some uncertainty still existed over the manufacturing method, was considered desirable.

The analysis led to a laminate being found that satisfies all three requirements mentioned earlier in this section. The stacking sequence of this laminate is $[(\pm 45/\pm 7)_2/(\pm 7/\pm 45)_2]$ which is an antisymmetric laminate with 16 plies. For the purpose of brevity, this laminate shall be referred to the FIL457 laminate since it is based on the filament winding manufacturing method, and contains ply orientations of 45° and 7°.

Figure 3.6 displays different perspectives of the worst case 3D point cloud failure envelope, which again happens to be Tsai-Wu. The envelope shows the stress states in an element (element ID 210) just in front of the cantilever clamping point as seen in Figure 3.5 in the 16^{th} (or outermost) ply as the load is cycled from a minimum to a maximum. The failure index seen at this point in the model is FI = 0.899. The model geometry is symmetric and therefore there is a point on the opposite face of the surface with the same FI. A scaling value of zero simulates unloaded conditions on the beam and this can be seen as the red line, representing the stress states during load cycle application, passes through zero in each view. Figure 3.6 A is an isometric view of the failure envelope while B, C and D represent orthographic views. The labels "stress11", "stress22" and "stress12" refer to the two normal stresses in the local 1 and 2 directions and the shear stress τ_{12} respectively.

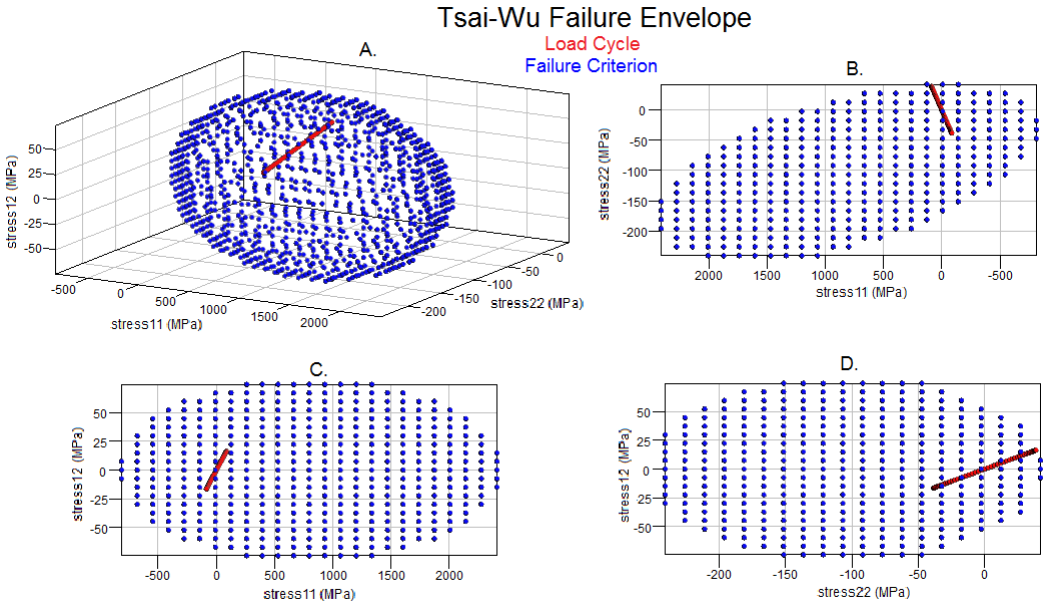

Figure 3.6: Tsai-Wu failure envelope at the point of maximum stress in the beam

To model the mass of the beam, a standard GFRP material density of 1854.6 kg/m^3 was assigned to the model. Additionally a zero dimensional lumped point mass of 26.4 kg was attached to the free end of the 30.2 kg beam. This mass represents the static mass of the grips, load cell and clevis attached to the beam. A normal modes analysis was done and the first natural frequency was found to be 43.2 Hz.

The FIL457 material was filament wound into the specified geometry that matches the FE model. The material was also specified to a second manufacturer that made fatigue testing specimens. Both the full-scale beam and the samples were intended for destructive testing in their respective experimental phases which will be discussed in the following section.

3.3 Experimentation

The experimental procedure for this investigation is broken up into three separate exercises that each supply information to. This section discusses these three test exercises and explains what information is passed on the next experimental step. Some results will be reported to provide reasons for the decisions made, but most of the results shall be discussed in the Results chapter.

Specimen fatigue testing is done to determine the S-N curve of the material and also the stiffness degradation characteristic. These tests will be done on test specimens to characterise the material behaviour. The information gathered from coupon fatigue testing will be used to formulate predictive stiffness degradation models for the full-scale set-up. Once the predictive models have been formulated and a suitable level of constant amplitude loading has been selected, the full-scale testing can commence. Information gathered throughout the full-scale testing will be compared to the behaviour of the material coupons. All experiments are designed to be done with the available materials and equipment of the Stellenbosch University Mechanical Engineering Department.

The experimental set-up to be used for the specimen testing is based on a combination of recommendations from various sources. The guidelines of the ASTM D3039/D3039M (2008), E1049-85 (2003) and D3479/D3479M (2012) testing standards will however be followed strictly.

Fatigue testing will be done on an MTS servo-hydraulic dynamic testing machine retrofitted with Instron software as shown in Figure 3.9. Testing shall be done at a stress ratio of $R = 0.1$. This decision is based on the findings of Cadavid *et al.*

(2017) that the stiffness degradation of a GFRP sample is highest under tension-tension fatigue loading.

3.3.1 Test Specimens

To avoid repetition in this chapter, the test specimen manufacturing method and geometry is discussed prematurely in this section. All three tests discussed subsequent to this subsection make use of the same test specimens and since some thought and decision making was required to select a geometry, a separate discussion is useful.

The laminate used for the specimens is the FIL457 laminate that was selected from the structural and material modelling section. This laminate is the same as the laminate in the filament wound beam since the objective of the testing exercise is to generate a model which will predict failure on a full-scale fatigue test. The constituents used in the material were selected to be as close as possible to those used in the filament wound beam. Epoxy resin SR 8100 with SD 8822 slow hardener was used to bond the unidirectional 500 gsm and biaxial 450 gsm together sheets together. Appendix C contains the specification sheets for each of these constituents. These can be compared to the specifications of the constituents used in the filament wound beam. Due to a requirement of high quality samples with end tabs, the manufacturing of the specimens were outsourced to ensure a higher quality than what could have been obtained by an in-house manufacture at Stellenbosch University. This decision ensured that the specimens had an even laminate thickness and were cut to constant widths.

The specimen geometry was based on the R05 specimen dimensions in the OptiDat database (Nijssen, 2006*a*) which conforms to the ASTM D3479/D3479M (2012) and D3039/D3039M (2008) testing standards specification. The equipment available in the Stellenbosch University Structures Laboratory was however a limiting factor in the geometry selection of the specimens since the safe operating limits of the universal testing machine and fatigue testing machine could not be exceeded before specimen failure. For this reason the specimen widths were reduced to 6 mm instead of 12 mm, and a gauge length of 45 mm was chosen to allow for an extensometer to be fitted during tensile testing. Figure 3.7 shows the geometry of the specimens which were fabricated as one laminated plate and then cut by a CNC water jet cutter. A fibre volume fraction of approximately 70 % was specified from the manufacturer. This translates to a material density of approximately 2132 kg/m^2. The end tabs are made from the same laminate and were also bonded to the plate with SR8100 epoxy in strips prior to cutting.

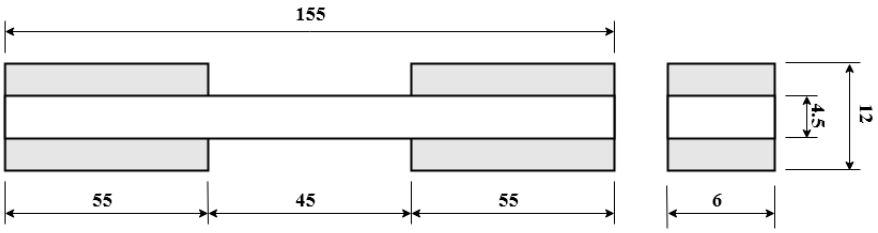

Figure 3.7: Mounted specimen prior to a tensile test

3.3.2 Material Specimen Tensile Testing

Fatigue testing was performed by applying cyclic loading to a material specimen until failure. For each test of constant R-ratio the cyclic loading amplitude was adjusted by applying a scaling factor to the ultimate tensile strength of the material. The first experiment and step in testing the material was therefore to determine the ultimate static tensile strength of the material by conventional tensile testing. This testing procedure is discussed below and is done according to the ASTM D3039/D3039M (2008) standard test method.

The specimens were mounted in a MTS Criterion Series 4000 Universal Testing Machine using standard MTS wedge grips. Both the wedge grips and the MTS 30 kN load cell are rated to a maximum tensile load of 30 kN. A Mess und Feinwerktechnik clip-on extensometer with a gauge length of 25 mm was mounted to the specimen. Figure 3.8 displays a specimen mounted between the wedge grips with an extensometer mounted onto the gauge. 6 specimens were tested at a crosshead displacement rate of 2 mm/min and a data capture rate of 20 Hz. All tests were run until failure which was set to be detected by the MTS TW4 TestWorks software as a 20 % drop in maximum recorded force. The argument here is that first ply failure is regarded as final failure and any residual strength in the material is not of interest.

An average ultimate tensile strength (UTS) of 469.32 MPa was seen from these tests with an average axial stiffness (Young's Modulus) of 27.09 GPa was seen from these six tests. The complete results from these tests will be displayed and discussed in the upcoming Results chapter.

3.3.3 Specimen Fatigue Testing

Following the establishment of the most basic material properties in the intended loading direction, a fatigue test set-up was designed to establish the material S-N curve and stiffness degradation characteristics. This test set-up was done according

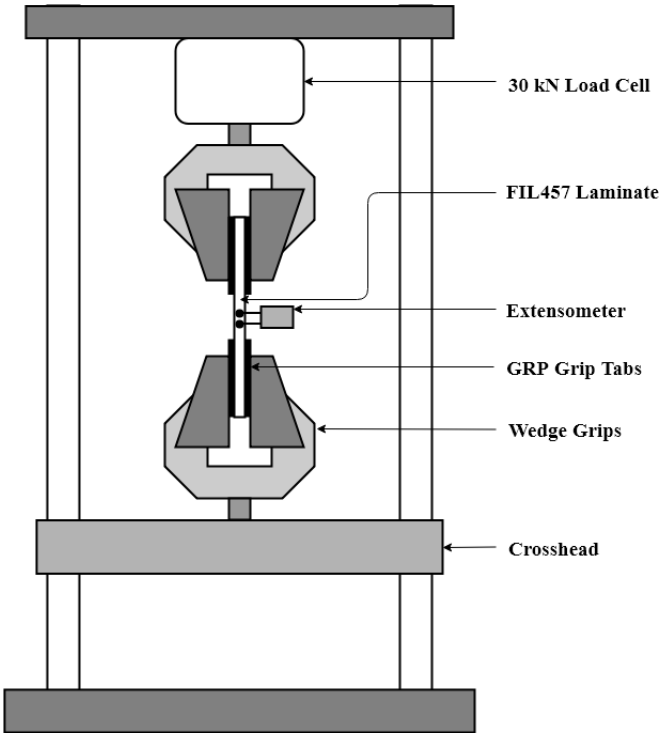

Figure 3.8: Tensile testing set-up with a mounted specimen and clip-on extensometer

to the ASTM D3479/D3479M (2012) Standard Test Method for Tension-Tension Fatigue of Polymer Matrix Composite Materials. Additional information was taken from the ASTM D3039/D3039M (2008) and E1049-85 (2003) standards.

The test was set up in a servo-hydraulic MTS testing machine retrofitted for fatigue testing with an Instron 8800MT controller. The standard recommends that the same geometry of specimens be used as in the static tension testing from the previous section. Remaining within the standard outlines, the standard MTS wedge grips were once again used to clamp the specimens. Due to sensor compatibility, crosshead displacement, and not extensometer displacement was used to record the strain in the specimen. A fatigue test specific extensometer was not obtainable for this test and conventional extensometers generally grip test specimens using bladed surfaces that introduce stress concentrations into the material which may cause premature failure in a fatigue test. The implication of this decision is that the gauge length in the fatigue tests would be the distance between the grips instead of the usually much smaller distance between the extensometer clamping points. This decision raised the concern that some accuracy would be sacrificed due to grip slippage, but it can be defended by raising the point that stiffness degradation will

be investigated by merely considering the relative increase in grip displacement and absolute accuracy in measurements, although ideal, is not of cardinal importance.

Bailey and Lafferty (2015) recognise that the current norm is to use grip separation in fatigue strain calculations and also note that the testing standards followed in this study make no specific note of gripping method. They do however recommend using a strain measurement sensor to ensure a consistent gauge length even though the ASTM standards are unclear about this. This statement is investigated in test post-processing by considering the actuator displacement at certain intervals and by inspecting whether each loading cycle passes through the same minimum displacement during the application of a sinusoidal load sequence. The outcome of this investigation eased concerns about about slipping and its results will be further discussed in the Results Chapter.

Specimens were mounted in the lengthwise direction using alignment lines drawn on the grips. Besides specimen geometry, the effective gauge length measured prior to each test and was consistently recorded to be between 50 mm and 52 mm apart. Figure 3.9 shows this test set-up. Not shown in Figure 3.9 is the FLIR E60 thermal camera was used to monitor the temperature of the specimens during testing. This was done because of the concern that the material may heat up during cyclic loading and that elevated temperatures may increase the rate of degradation in material properties.

Due to the concerns over temperature build up, the testing frequency for fatigue testing was uncertain. Preliminary fatigue tests were conducted to determine the test frequency with the expectation that the temperature within the specimen would increase but eventually stabilise at different rates depending on what frequency the test is conducted at. Additionally it was expected that a higher applied load would cause the temperature to increase more rapidly and that stabilisation would occur at a higher temperature. Since the epoxy used in the specimens state that it is rated for operation until 80 °C, a safety factor of 2 was added and a stabilised temperature of 40 °C was chosen as the pass/fail criterion. Most sources indicate fatigue testing of composite materials to be done at frequencies between 2 and 10 Hz, 5 Hz was therefore taken as a starting point for this preliminary analysis.

The specimen surface temperatures were monitored by the FLIR E60 thermal camera as shown in Figure 3.10 and they were tested at 45 %, 50 %, 65 % and 80 % of the material UTS. Ambient temperatures of between 9 °C and 12 °C were recorded during these preliminary tests. The intention was initially to test at other frequencies besides 5 Hz, but all tests passed by showing temperature stabilisation before 40 °C. All tests confirmed the hypothesis that an increase in loading am-

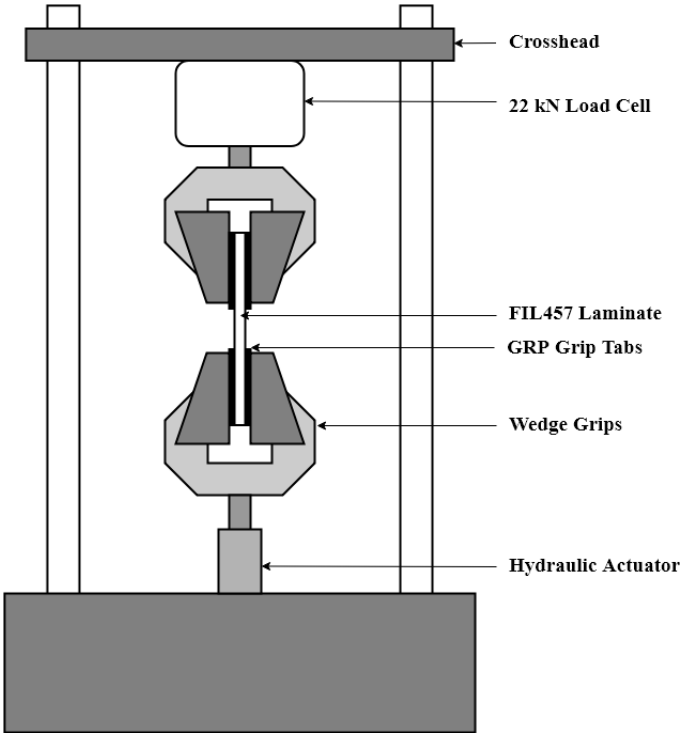

Figure 3.9: Mounted specimen prior to a fatigue test

plitude (and therefore mean stress) causes an increase rate of temperature build up within the specimens. The specimens tested at 80 % UTS displayed the most threatening stabilisation temperature at 36 °C. The conclusion from this preliminary testing operation was that 5 Hz is indeed a suitable testing frequency given that the ambient temperature during actual temperature remains approximately the same as in these preliminary tests.

The ASTM D3479/D3479M (2012) Standard Test Method for Tension-Tension Fatigue of Polymer Matrix Composite Materials recommends that a minimum 12 fatigue tests should be conducted to determine the S-N curve of a material and a minimum of 24 for reliability data. This recommendation was followed and 16 tests with an R-ratio of $R = 0.1$ and a maximum loading amplitudes of 45 %, 50 %, 55 %, 60 %, 65 % and 80 % UTS were conducted. Table 3.3 shows the actual minimum and maximum loads applied in at each load level and the amount of specimens tested at each level. The reasons for only two tests being reported at load levels 45 % and 55 % are because of bad interrupted or failed tests. Given the time schedule and project objective, the value of completing the study was considered higher than that of a scientifically representative population, and the

Figure 3.10: Temperature monitoring with thermal camera

decision was made not to continue with further fatigue testing. All of the tests were conducted with a sinusoidal load application curve of 5 Hz. The temperature of the specimens were continually monitored to ensure that the specimen temperature does not exceed the 40 °C threshold. Since the control software does not allow for continuous data logging, test data was gathered at increments during each test to determine discrete load-displacement curves. This incremental data gathering was done by pausing and immediately restarting the fatigue test which causes the software to log all the data captured in the last 10 cycles before the pause. Figure 3.11 shows how such a test was conducted with a higher density of data capturing events during the beginning and end of life to in an attempt to capture the expected first and third rapid stiffness degradation stages. The x-axis, indices, indicate the number of data points saved by each data capturing event, which is approximately 300 data points or ten cycles. Given the known gauge length of a test, the slope of the load-displacement curves for the ten cycles prior to each event could then be found for a discrete stiffness of the material. The expectation from literature was that a trend could be observed that would aid the formulation of a stiffness degradation model.

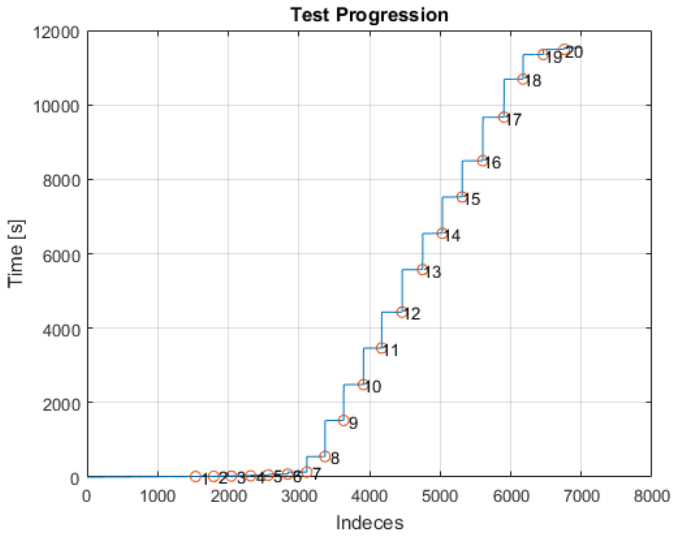

Figure 3.11: Test progression with stiffness measurement events

Table 3.3: Fatigue testing load level amplitudes

Percentage of UTS	Max. Load [N]	Min Load [N]	R-Ratio	Nr of Specimens
45	4294.55	429.45	0.1	2
50	5368.18	536.82	0.1	3
55	5905.01	590.50	0.1	2
60	6441,83	644.18	0.1	3
65	6978,64	697.86	0.1	3
80	8589,10	858.91	0.1	3

3.3.4 Full-Scale Fatigue Testing

The objective of the full-scale test is to investigate whether the stiffness degradation trends witnessed in specimen testing can be seen in full-scale simulated conditions. Stiffness degradation can be observed at the elementary level as the maximum displacement of the beam increases over time under cyclic loading. Additionally it will be investigated whether an experimental modal analysis of the beam can give a similar indication of how the material stiffness deteriorates. This section discusses the hardware and software experimental set-up to achieve these goals.

As discussed previously, the beam will be cantilever mounted and excited sinusoidally at the free end to simulate the bending moments seen by the fan blade under real life operating conditions. The design was approached with the objective

of creating boundary conditions that are as rigid as possible to correspond to the FE model discussed in Section 3.2.5. This was achieved by using clamps cut from 50 mm mild steel plate and fastened with ISO grade 8.8 high tensile threaded rods and lock nuts to resist self-loosening during fatigue loading, which is a problem previously observed on the ACC fans at Matimba power station. Another concern was that the hard edges of the mild steel clamps might damage the fibres in the outer layers of the laminate during initial clamping and fatigue loading. This issue was addressed by inserting strips of butyl rubber bicycle inner tubes between the beam and the clamp surface. Figure 3.12 shows the configuration a single clamped section at the fixed end of the beam. The clamps at the clamped end of the beam are bolted to the same rigid steel block platform used during the experimentation of Els and Muiyser (2016). This platform is in turn bolted and secured to the laboratory floor.

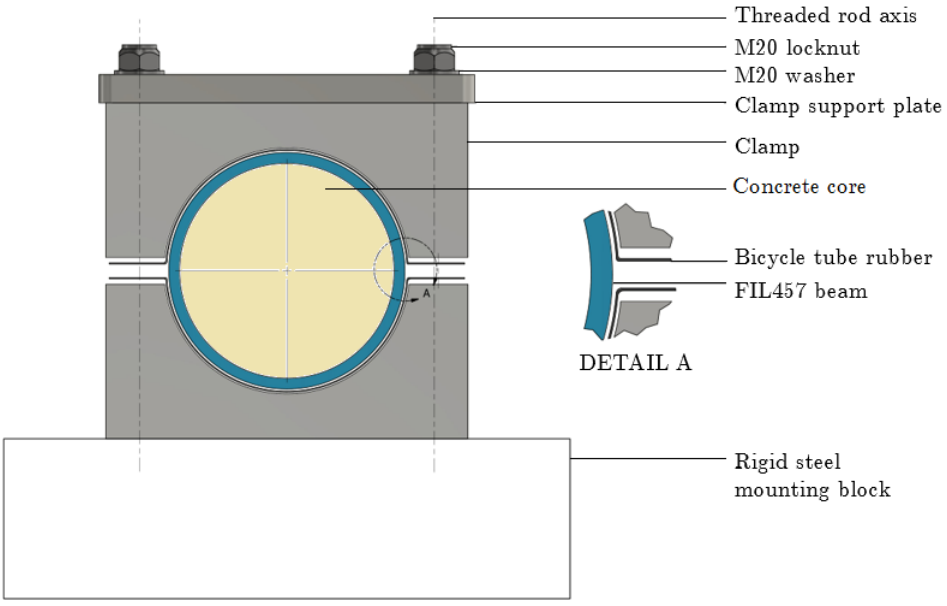

Figure 3.12: Clamped section configuration

To prevent the material from collapsing under the clamping pressure, two concrete cores were cast and inserted to reinforce the clamped sections of the beam. A similar epoxy-concrete core is used in the current standard M-type fan blades installed at Matimba power station. The lengths of these concrete cores were 60 mm and 220 mm long respectively and determined by the thickness of the clamp at the free end and the distance between the clamps at the fixed end. A 1:2:2 high strength concrete mixture prescribed by Owens *et al.* (2012) was cast into 160 mm

PVC pipe moulds with a bowl at the bottom to ensure a convex end for stress relief. After casting, the cores were left for the prescribed 28 days to ensure maximum curing and strength. Even though the fit of the plugs were relatively tight, Ampreg 21 resin and standard hardener was used to ensure that the plugs were bonded and sealed in place.

The cantilever mounted beam is excited sinusoidally at its free end by a hydraulic cylinder connected to the beam by a similar clamping configuration as discussed for the fixed end. The Instron retrofitted MTS servo-hydraulic fatigue machine is used to apply the sinusoidal load to the free end of the beam. The machine is rated to be operable up to 22 kN, which is more than enough force required to exert the calculated breaking moment of 14 kN·m.

A pin connection compensates for the rotational degree of freedom between the load cell and the clamp at the free end. Using beam theory and trigonometric relationships, the maximum expected resulting force perpendicular to the bending force is calculated to be approximately 69 N. A second degree of freedom exists as a result of beam bending which causes the tip to be offset slightly as the beam deflects under loading from the fatigue machine's piston rod. This deflection in the perpendicular direction does not satisfy the criteria of "large deflections" (Benham et al., 1996) since the bending deflection of the beam is not greater than 10 times the beam thickness. Despite this, a large-deflections non-linear FE analysis was done to ease concerns over additional perpendicular loads on the machine. The results from this analysis were included in the laboratory safety report and shown in Appendix E and showed that even at the maximum expected bending deflections, perpendicular deflections were in the order of micrometers and that the resulting forces on the equipment would be negligible.

A configuration image of the full-scale test with the testing machine and load cell is shown in Figure 3.13. The cyclic force is applied from the bottom of the beam as shown in compression relative to the load cell. This is done to ensure that the testing machine does not lift itself from the laboratory floor.

The decision of what amplitude to conduct full-scale testing at is based firstly upon the prescription from Whitworth (1997) that fatigue testing for stiffness degradation data should not be conducted at levels higher than 60 % UTS. Secondly, the likelihood of good quality data is considered, where it seemed from specimen testing that high amplitude testing yielded more consistent stiffness degradation results. The final consideration was the available time to conduct the fatigue test.

The stress-life curve and the stiffness degradation data collected in specimen

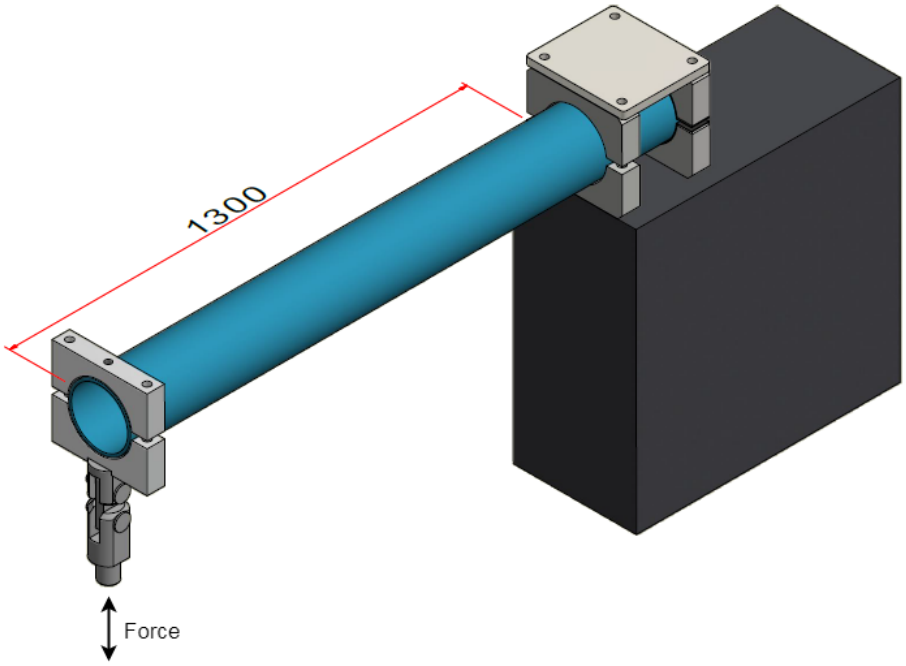

Figure 3.13: Full-scale test configuration with frame omitted

testing was observed and it was decided that full-scale fatigue testing would be done at 55 % UTS. At this load level, the maximum applied load by the testing machine is 5.923 kN with a minimum of 0.592 kN and a mean of 3.258 kN. Testing at this load level is predicted to last 30682 cycles until failure. The predicted stiffness of the beam at 80 % of life or 24546 cycles is 93.9 % of the initial stiffness.

Similarly to specimen fatigue testing, a brief set-up period is necessary for tuning the controller of the testing machine and selecting the testing frequency. To protect the specimen from too much damage, this set-up was done at a low load amplitude for the full-scale test.

To remain within safe machine operating limits and to protect the specimen from heat build up observed at higher frequencies, only loading frequencies between 1 Hz and 3 Hz were investigated. A further consideration is how the dynamic effects of the 26.4 kg clamp mass become greater at high test frequencies. The added dynamic force can be expressed by multiplying the clamp mass with the second derivative of the wave equation:

Table 3.4: Maximum dynamic forces at possible test frequencies

Frequency [Hz]	Max. dynamic force [N]
1	±0.3511
2	±1.4044
3	±3.1599

$$F_{dynamic} = m\frac{d^2y}{dt^2} = m\omega^2 a \sin \omega t \tag{3.3.1}$$

Table 3.4 shows what the maximum dynamic force would be at each of the possible frequencies. This dynamic force, which is shown to be a function of time, is to be subtracted from the load cell measured force. It is observed that the magnitude of this dynamic force is much smaller than the intended loading amplitude and a testing frequency of 3 Hz was selected since even the highest considered frequency adds close to negligible dynamic effects.

3.3.5 Experimental Modal Analysis

An experimental modal analysis (EMA) was set up to determine the natural frequencies of the beam after being mounted and before fatigue loading. The EMA is done to establish the first natural frequency of the beam in its mounted condition and to compare it to a second natural frequency taken close to the end of the material life. The intention is to find out whether material stiffness changes during the course of a fatigue test. Determining natural frequencies beyond the first is not considered to be of particular interest for this analysis, since the change in first natural frequency should be sufficient to determine whether material stiffness has decreased.

A simple EMA set-up with the only hardware components being a single piezoelectric accelerometer and modal hammer was done. Additionaly the set-up requires a DAQ and the (Siemens, 2013) LMS Test.Xpress software to determine the FRF for the measurements. An accelerometer is mounted on aluminium tape close to the free end of the beam where vibrational displacements will be at a maximum and can therefore be easily detected. The clevis and clamps are removed to ensure unconstrained movement of the free end of the beam.

The PCB piezoelectronics modal impact hammer is used to excite a vibration in the beam which is detected by piezoelectric accelerometer. The signals from these transducers are recorded by the DAQ and the software processes the information

Table 3.5: Natural frequency equation system variables

Property	Symbol	Value	Unit
Area moment of inertia	I	2.32673262422e-5	m^4
Density	ρ	18.875	kg/m
Distance to free end	L	1.3	m
End mass	m	3.7	kg

to display an FRF from which the natural frequencies can be observed.

Given knowledge on the material density, beam length, wall thickness and the end mass of the concrete plug, the required properties of the system are shown in Table 3.5 and the natural frequency of the beam can be expressed as:

$$\omega_n = \frac{1}{2\pi}\sqrt{\frac{3EI}{(0.2235\rho L + m)L^3}} \tag{3.3.2}$$

The relationship between bending stiffness, which will be recorded during the test by means of force vs displacement data, is shown in Figure 3.14.

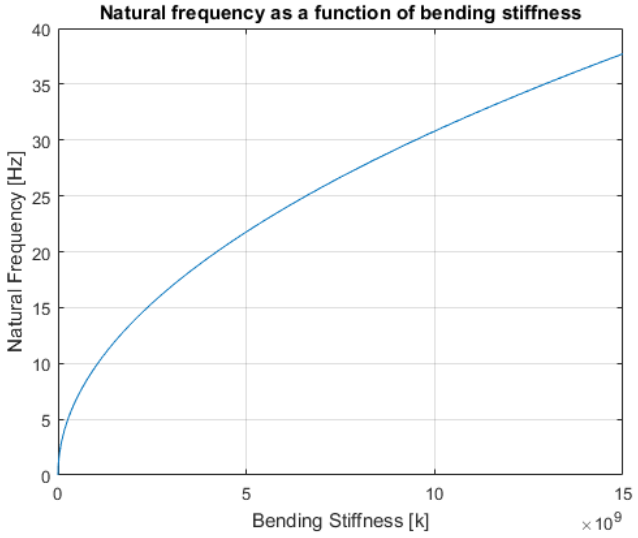

Figure 3.14: Cantilever beam first natural frequency vs bending stiffness

Chapter 4

Results and Discussion

4.1 Material Tensile Testing Results

A sample containing six specimens of the FIL457 was tested according to the D3039/D3039M (2008) standard test method for tensile Properties of polymer matrix composite materials. The specimen geometry, test set-up and method are described in the previous chapter. This section reports on the results obtained from these six tests.

Figure 4.1 shows the six stress-strain curves generated during tensile testing. A corresponding summary of the test data is shown in Table 4.1. The jagged appearance of some of the curves in Figure 4.1 is attributed to suspected extensometer slippage which may be due to slightly blunt knife-edges in the extensometer or due to some early isolated fibre failure under the blades. From this information an average UTS of 469,32 MPa and an average Young's Modulus in the global 1-direction of 27,09 GPa is observed. The standard deviations, maxima and minima between these tests are also shown.

The UTS and material stiffness (Young's modulus) are important values for the formulations for the specimen fatigue test. The UTS will be the value which will be scaled to find the magnitude of the applied sinusoidal loads and the material stiffness will serve as a reference for the stiffness degradation recordings during the fatigue test.

Table 4.1: FIL457 tensile testing results summary

Test Nr.	UTS [MPa]	Ultimate Tensile Strain [%]	Elastic Modulus / Stiffness [GPa]
1	451,55	1,59	29,83
2	469,10	1,83	26,67
3	412,40	1,60	27,01
4	531,39	2,19	28,54
5	469,12	1,80	24,50
6	482,36	1,98	25,99
Average	469,32	1,83	27,09
Maximum	531,39	2,19	29,83
Minimum	412,40	1,59	24,50
Std Dev.	35,54	0.21	1,72

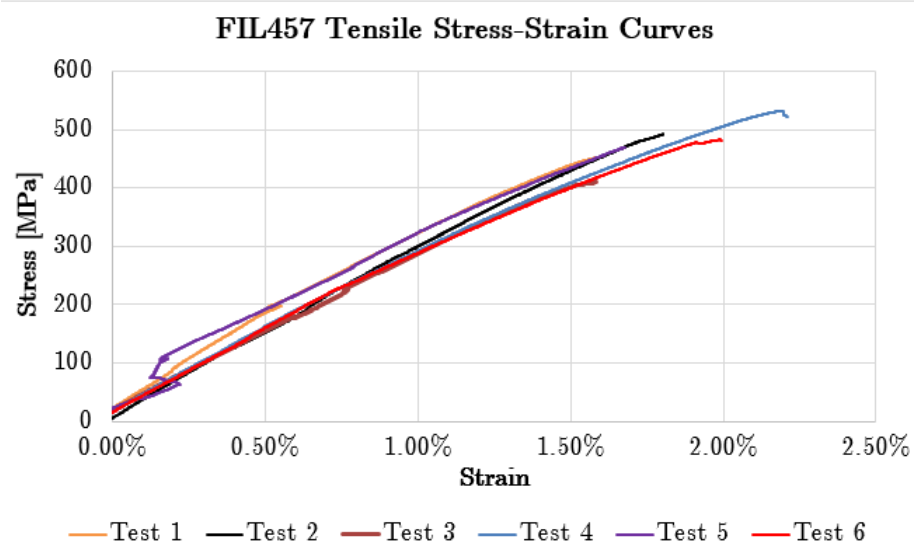

Figure 4.1: FIL457 tensile testing Stress-Strain curves

4.2 Specimen Fatigue Testing Results

Following the results of the tensile testing exercise, the actual loading magnitudes based on the selected load levels were established. These magnitudes are shown in Table 3.3 in Section 3.3.3. A stress stress-life curve and stiffness degradation data was gathered from these tests and will be discussed in this section. A discussion about the concern over wedge grip slippage will firstly be included.

4.2.1 Wedge Grip Slippage

The concerns over whether testing with standard wedge grips may lead to slipping of the tabs is investigated in this section. The ASTM D3479/D3479M (2012) standard makes no specific recommendation to use specialised fatigue grips and even prescribes in paragraph 7.2.5 that the same grips as in the tensile test should be used. Slippage as well as the effect of clamping on the specimen were nevertheless concerns since Bailey and Lafferty (2015) found that gripping effects do affect measured stiffness results. An additional concern raised by these authors that is especially relevant to the specimens used in this study is the fact that specimens with end tabs from composite materials, are prone to heat build-up within the tabbed region. It is unknown to what extent heat built up within the tabbed region during fatigue testing in this study since temperature monitoring was only focussed on the gauge area of the specimen and not within the clamped region, but given the evidence that the authors present, it is very likely that the same phenomenon occurred during fatigue testing in this project.

The first point of investigation was to consider the load - displacement curves of consecutive loading cycles during different periods of the fatigue test. To illustrate this, consider Figure 4.2, which shows the first 7 cycles just before a stiffness recording interval. Here a univariante smoothing spline with a smoothing factor of close to 1 but not equal to one is fit through the data. These 7 cycles can also be represented on different axes to investigate whether the grips returned to approximately the same point in consecutive loading cycles. When zooming in on the points where the loading direction changes sign, the discrete displacement maximum or minimum values for each cycle can be compared to determine whether slippage is occurring. It is reasoned that, if present, slippage will be most easily observed where the loads and displacements are at a maximum and therefore Figure 4.4 is a zoomed-in image of Figure 4.3 at the maximum turning points. When observing Figure 4.4 the maximum displacements of each cycle all occur at 73.92 mm. While there is some minor scatter in the load cell recorded part of the data, the maximum displacement readings, which have been rounded to the second decimal to eliminate noise, all occur at the same spot. The accuracy of the displacement readings at the maximum as well as at the minimum turning points of consecutive cycles is consistent throughout all tests and suggest that slippage did in fact not occur on the gripping interfaces during fatigue testing.

This investigation is reasoned to only be sensible when comparing consecutive cycles. When non-consecutive data is compared spaced far enough apart for stiff-

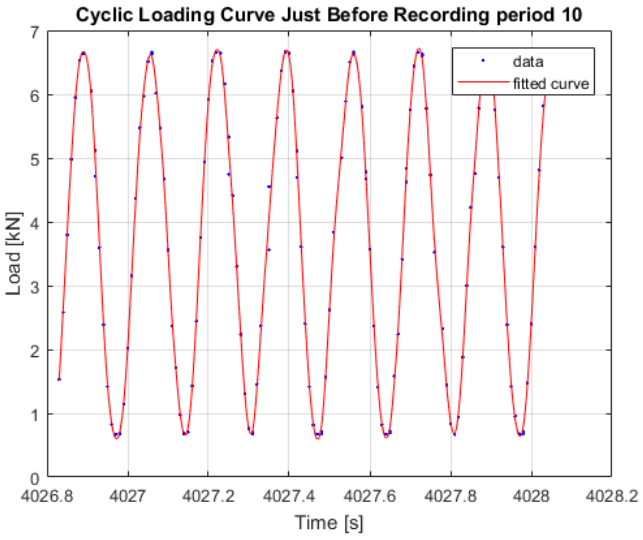

Figure 4.2: Cyclic loading curve example

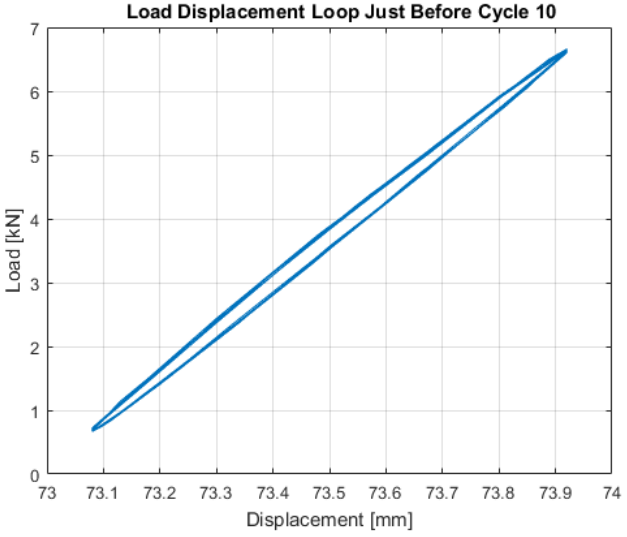

Figure 4.3: Load-displacement curve example

ness degradation to have occurred in the material, the displacement turning points clearly do not correlate and it might seem as if slippage is occurring. This is however not the case since the decreasing stiffness causes the loading amplitude means, maxima and minima to shift over time. This theory was validated by observing the

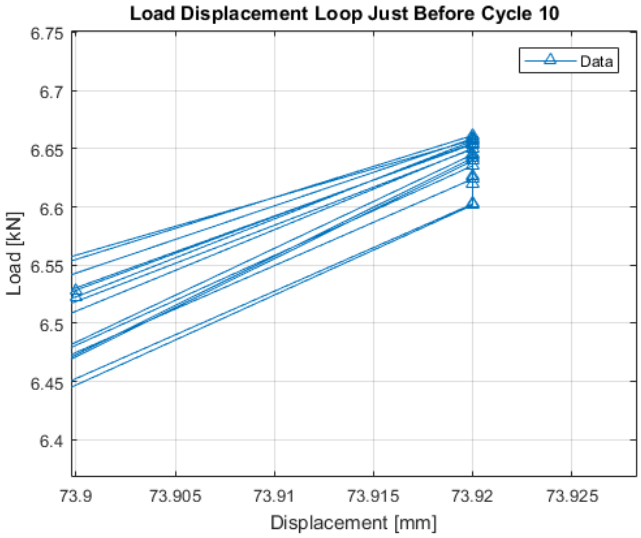

Figure 4.4: Turning points on load-displacement curve

same behaviour in the work of Cadavid *et al.* (2017).

4.2.2 Fatigue Life and Predictive Palmgren-Miner Model

The initial prediction of induced damage was done by applying the loading data to a Palmgren-Miner model of a generic GRP material. As explained, the analysis was merely done to determine which of the given datasets was the most damaging and would be considered the worst-case scenario. With the information obtained from material fatigue testing, the actual S-N curve for the FIL457 material was drawn and will be discussed in this section.

Before mounting, the specimens were transparent and the edges were smooth. It was observed that the transparency and edge smoothness of the specimens changed over time as the fatigue test progressed. Fatigue failure generally occurred in the gauge of the specimen. Figure 4.5 shows some of these specimens where slight thickening of the material can be observed within the gauge of the specimens. The D3039/D3039M (2008) would describe the failures of the specimens as delamination in the gauge and in middle of the specimen cross section. Some specimens displayed failure that tended closer toward the grips but failure within or at the grips was never observed.

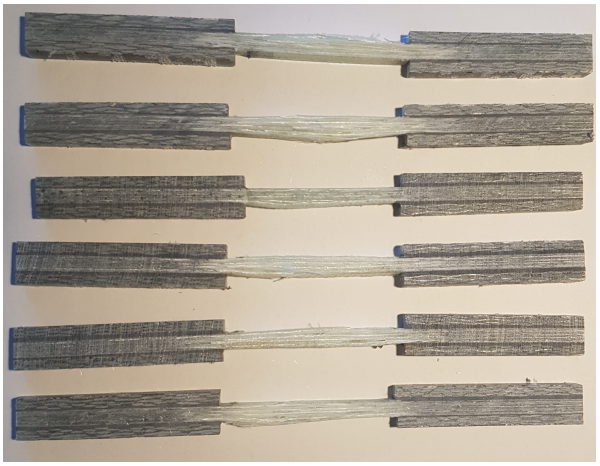

Figure 4.5: Failed fatigue specimens

Besides periodic stiffness recordings, which will be discussed shortly, the amount of cycles to failure for each specimen was recorded to draw an S-N curve for the FIL457 laminate. A least-squares fit of a power function through the data returns a line with the function $y = 7.52 \times 10^8 x^{-0.10}$ with a coefficient of determination $r^2 = 0.89$. The coefficient of determination is denoted in this thesis as a lower-case r to prevent confusion with the upper-case R which refers to the fatigue stress ratio in Equation 2.4.1. This power function shown in Figure 4.6, which is straight line when plotted in log-log scale, has a slope variable of -8.71214 and an intercept on the stress axis of 6.80×10^8, was used to predict the actual expected lifetimes of the material with the known loading conditions as input conditions. Also visible on this curve is the excluded data at 45 % UTS and the upper and lower 95 % confidence bounds.

The slope variable b of this curve is consistent with previous studies in the Opti-Dat database where laminates with less plies have S-N slopes slightly steeper within the range of -10, but still within the same order of magnitude as can be observed from Table 2.4.1. The result from one fatigue test at 45 % UTS was omitted due to the test being stopped prematurely because of user error. The same method of analysis was followed as before where the data is rainflow counted and each cycle is applied to the S-N curve. The results from the statistical analysis of the data is shown in table 4.2.

The S-N curve slope variable and stress-intercept can be used to draw a straight line in log-log scale and a Palmgren-Miner damage prediction can be made given any constant amplitude loading with a ratio of 0.1. Variable amplitude loading

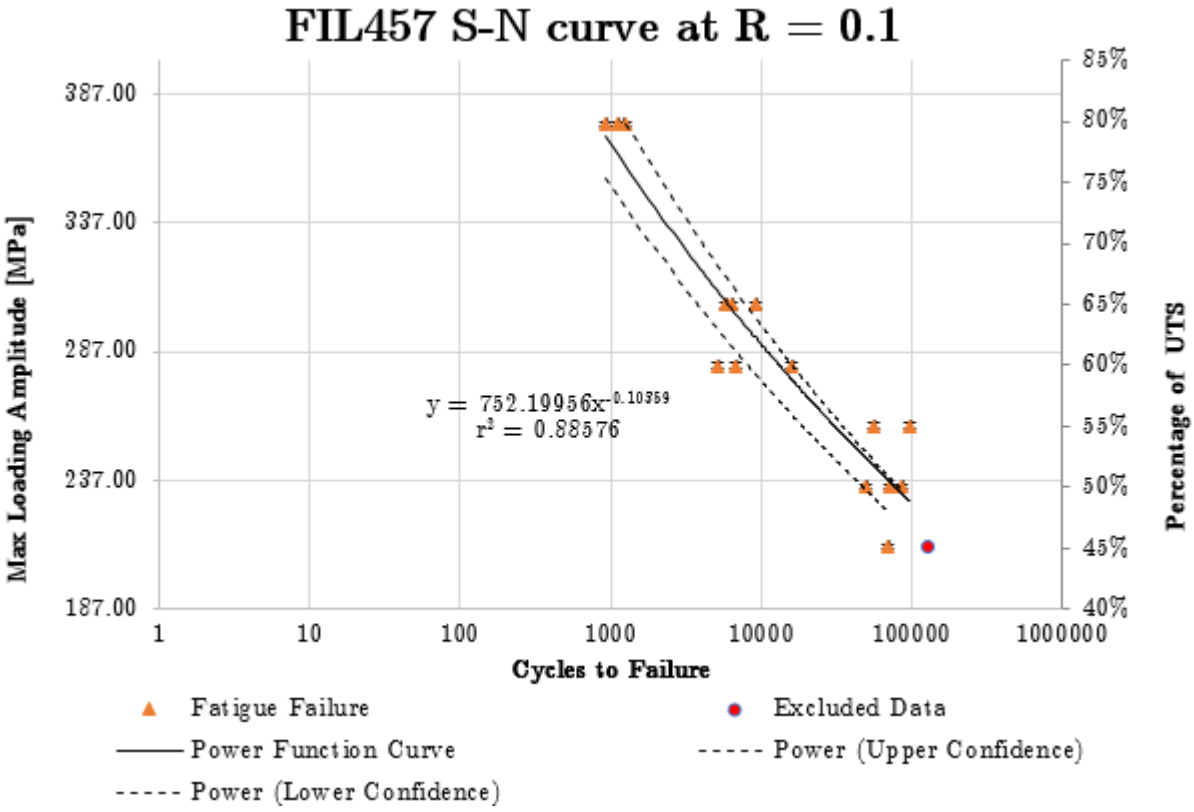

Figure 4.6: S-N curve for the FIL457 GRP laminate at R = 0.1

data can also be applied to this curve, but since it is specific to loading ratios of 0.1, found to be one of the most damaging by Cadavid *et al.* (2017), the prediction will be highly conservative. This analysis was nevertheless done using HBM nCode and the most damaging dataset, 2b, was predicted to induce failure within approximately 61.6 days. This is obviously not a realistic estimation of expected life since very few of the cycles within the most damaging dataset actually have a fatigue stress ratio of 0.1. In this case, even cycles with a much smaller ratio between maximum and minimum stress are assumed to have a 0.1 R-ratio. Ideally many different S-N curves would be required to make an accurate PM damage estimation, but this is not possible in this project and that is why it is necessary to look at material property deterioration trends such as stiffness to make real-time damage progression predictions.

Table 4.2: Fatigue testing results table

Percentage of UTS	Nr of specimens	Avg cycles to failure	Std Dev.	Margin of error	Upper 95 % bound	Lower 95 % bound
45	1	69022	–	–	69022	69022
50	3	68732	17594.82	19910.42	88642.42	48821.57
55	3	63466	18551.76	20993.30	84459.63	42473.02
60	3	9168	5692.48	6441.65	15610.32	2727.01
65	3	7077	1751.35	1981.84	9059.18	5095.48
80	3	1087	151.28	171.19	1258.52	916.14

4.2.3 Stiffness Degradation

Stiffness measurements were taken incrementally during each of the 16 fatigue tests. The stiffnesses were measured by making use of the grip displacement and load cell data. This information along with knowledge of the specimen cross sectional area and gauge length is used to calculate the material stiffness.

As discussed earlier, stiffness is calculated by the quotient of force and grip displacement. Since we know the gauge lengths and cross sectional areas of all the specimens, an approximated Young's Modulus, generally referred to in this thesis as stiffness can be calculated. This stiffness, although calculated with the same formula as Young's Modulus, is not expected to have the same magnitude as Young's Modulus, because of the much greater gauge length and other factors like tab thickness that contribute to deviations. There should however be a strong proportionate relationship between measured stiffness and actual Young's Modulus since both are calculated from properties with the same units. Figure 4.7 shows how stiffness was calculated from the test data. Practically, this was implemented by identifying the maxima and minima in the curve of 10 cycles before a measurement event and then finding the slope of a straight line between a corresponding maximum and minimum. Approximately ten slopes are found for each measurement event and these are then averaged to find the stiffness which is plotted as a straight line on the graph.

The data representing stiffness degradation when observed discretely for a single test displays one of two main trends. The first stiffness degradation trend is the three stage stiffness degradation model described by Shiri *et al.* (2015) and many others. This trend, shown for a specimen fatigue tested at 55 % UTS was primarily observed for specimens tested at the higher of the loading cycles implemented in this study. An example of this observed trend is shown in Figure 4.8 and with normalised axes in Figure 4.9. The data however presents itself such that this three-

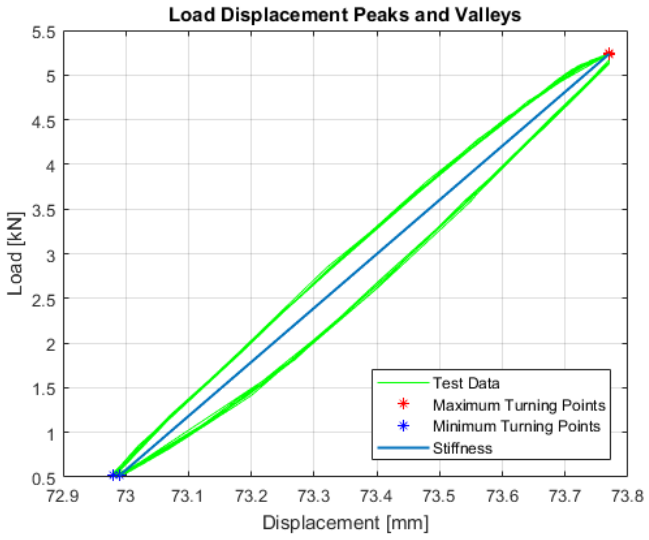

Figure 4.7: Load displacement cycle curve with stiffness calculation

stage trend cannot always be recognised and a second group of stiffness degradation was also observed. This second type of trend, referred to as the initial increase type, appears to rapidly gain stiffness in the initial phases of testing like in the example Figures 4.11 and 4.10 for the specimen fatigue tested at 45 % UTS, before reaching an ultimate stiffness, then displaying a stable, almost constant stiffness for a while and then rapidly decreasing. This type of trend was initially thought to be due to some sort of measurement error, but it has occurred across numerous tests and the reasons for it are a point of speculation. An investigation into the reasons for this is likely cause for a follow-up study.

The current speculation is that the fact that there are no fibres parallel to the longitudinal direction might influence the stiffness degradation behaviour as some fibres may become aligned to the direction of force application and add extra stiffness or that the thickness of the specimen end tabs may introduce significant inconsistencies in the clamped region which may have lead to inaccurate recordings. The increase in calculated stiffness from load vs crosshead displacement data is surprising since a faulty set-up could easily be blamed for the inverse, a disproportionate decrease. Such a decrease could be attributed to grip slippage or end tab de-bonding, but an increase, as was often observed, means that the effective gauge length between the griping surfaces must have decreased slightly in the initial phases with constant load application cycles before increasing. With the specimen under constant tension, upward grip slippage cannot be possible.

Table 4.3 summarises the trends observed with 31.25 % of specimens showing an initial increase in stiffness and 56.25 % of specimens showing the expected three stage decrease in stiffness. The second 45 % UTS specimen had no recorded data and there were too few recorded data points for the second 60 % UTS specimen to conclude what type of trend was observed.

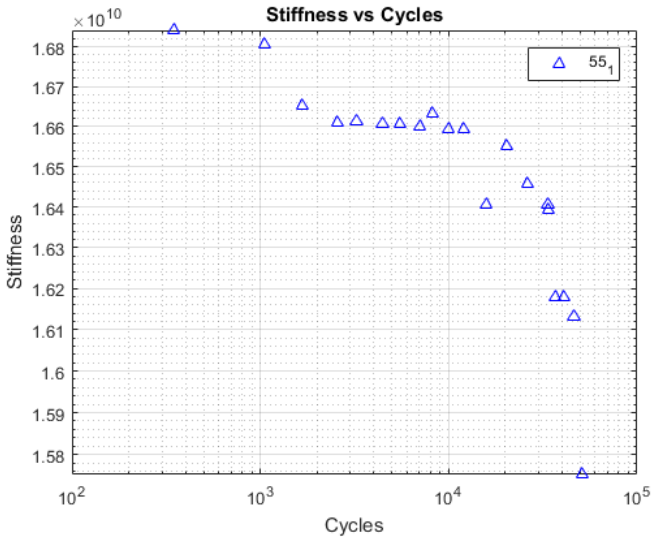

Figure 4.8: Three stage stiffness degradation observed at 45 % UTS

Many different stiffness degradation models were tested, and while some fit single sets of data well, no single model could be found that universally fits all data-sets. An example of a good fit is illustrated in Figure 4.12 by the power function used by Cadavid *et al.* (2017). Here the constants K and n are 0.8689 and -0.0172 respectively. The correlation coefficient r^2 is equal to 0.916.

Unfortunately the success of a model on a single dataset could not be repeated for all datasets and for this reason, the data in the figures above are presented without trend lines or model curve fits. To present the data in a comparative format, the decision was made to consider all stiffness data collectively in an attempt to recognise a trend. When this was done, on normalised axes of stiffness vs cycles to failure, it could be seen that the all specimens display a general trend of stiffness degradation and that ultimate fatigue failure always occurred with a final stiffness of higher than 78 % of the initial stiffness. The implication of this is that when

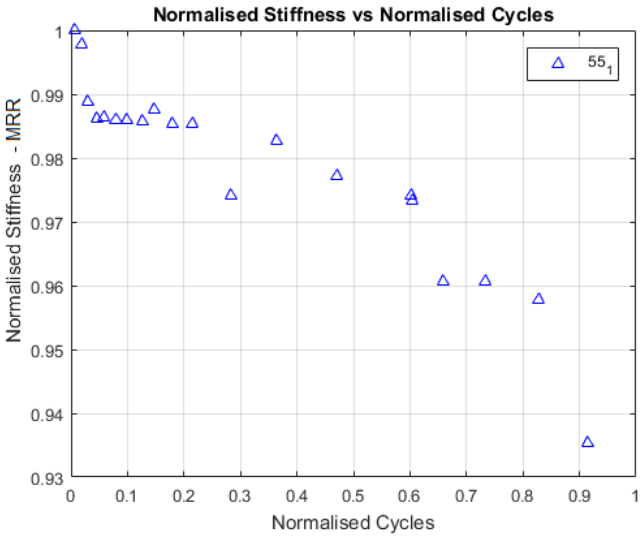

Figure 4.9: Normalised three stage stiffness degradation observed at 45 % UTS

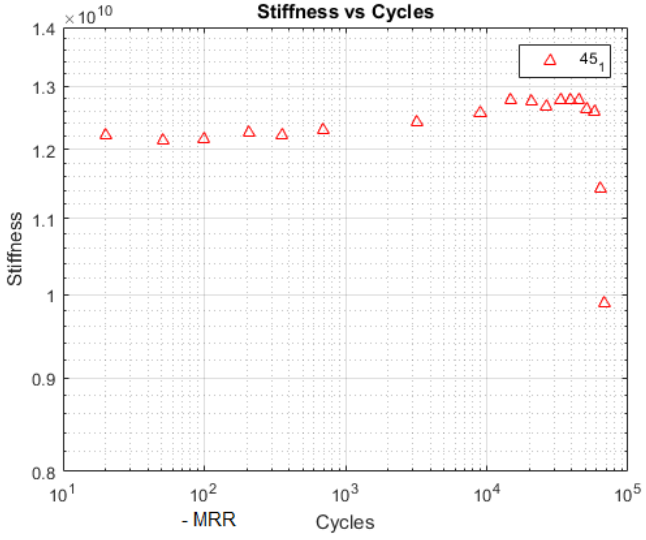

Figure 4.10: Initial stiffness increase observed at 55 % UTS

plotting the results on full scale, the data presents itself to be approximated by a straight line. Furthermore, upon close inspection of the stiffness data, rapid stiffness degradation seems to occur around 80 % of the ultimate life.

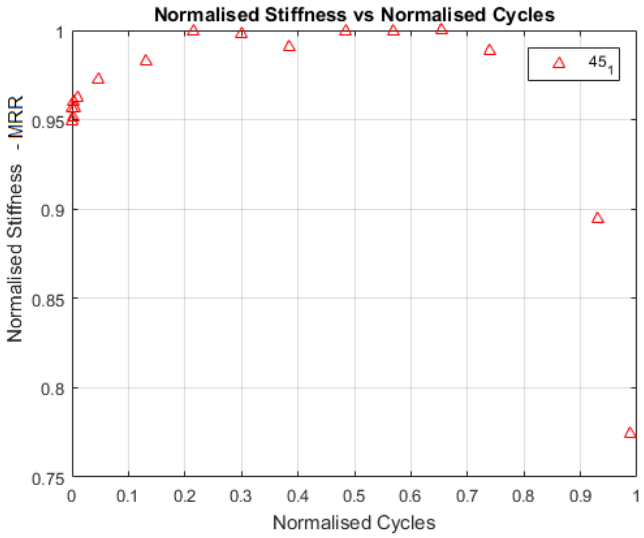

Figure 4.11: Normalised initial stiffness increase observed at 55 % UTS

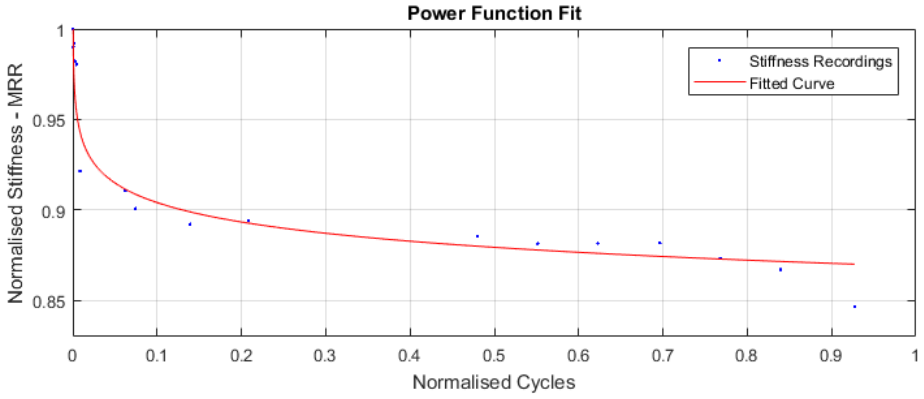

Figure 4.12: Power function fit to stiffness recordings at 50 % UTS.

Given that the part in which this material will hypothetically be used, should not be operated to failure, the decision was made to consider 80 % of the ultimate life as the general point of non-operability. The straight stiffness degradation lines are therefore plotted by neglecting the last 20 % of life. When doing a linear regression of the calculated stiffnesses for each group of specimens tested at the same load level with the origin forced at 1 on the normalised stiffness axis and 0 on the normalised cycles to failure axis, a three-dimensional plot can be generated with normalised cycles to failure, normalised stiffness and loading levels on the x-,

Table 4.3: Observable stiffness degradation trends

Percentage of UTS	Stiffness Degradation Trend	Note
45	Initial increase	
45	None	Data excluded
50	Initial increase	
50	Initial increase	
50	3 stage decrease	
55	3 stage decrease	
55	3 stage decrease	
60	Initial increase	
60	None	Very few data points
60	Initial increase	
65	3 stage decrease	
65	3 stage decrease	
65	3 stage decrease	
80	3 stage decrease	
80	3 stage decrease	
80	3 stage decrease	

y-, and z-axes respectively. From this three-dimensional plot in figure 4.13, which is challenging to present on a non-interactive 2-dimensional space such as paper, it can be seen that the slopes of the straight lines modelling stiffness degradation decreases as the cyclic loading level is increased. An exception is observed for the 80 % UTS tests where the slope is greater than for the preceding 65 % UTS group. Although noteworthy, this unpredictability does not come as a surprise since it is known that the prediction of material properties becomes inaccurate at high loading levels. Whitworth (1997) recommends that further analysis, presumably beyond simple cycles to failure information, at loading levels higher than 60 % should not be done. Table 4.4 shows the slopes of straight line fits of normalised stiffness drawn for each loading level. The individual plots per load level, shown together in Figure 4.13, are presented in Appendix A.

From these results it is suggested that when a FIL457 part undergoes constant amplitude fatigue at an R-ratio of 0.1 and one of the amplitudes tested during this study, that when the material reduces to below a stiffness specified by the stiffness degradation model, it has reached 80 % of its life and should be replaced. The threshold stiffnesses found for each load level are shown in the third column of Table 4.4.

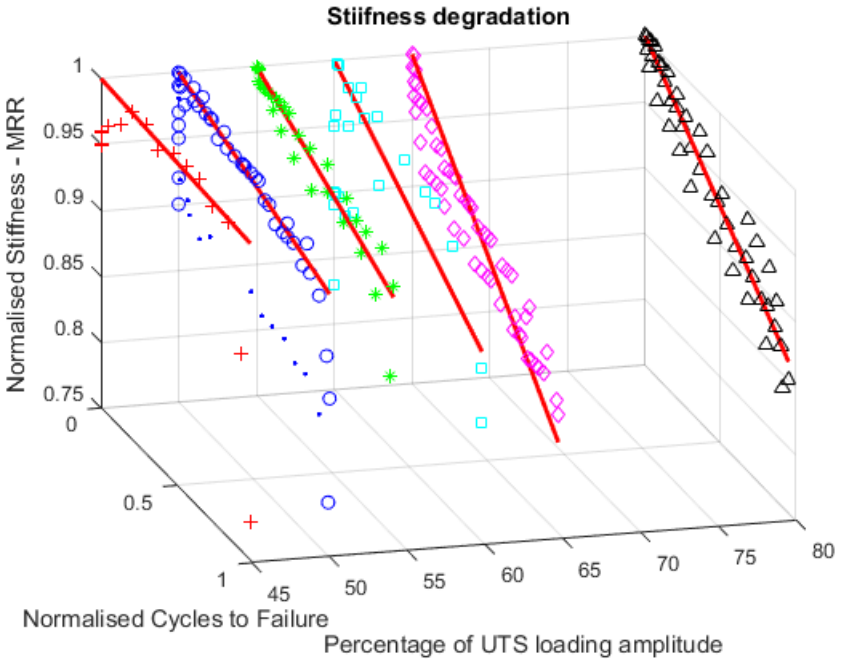

Figure 4.13: Combined stiffness data for all load levels with linear degradation slopes.

Table 4.4: Observed stiffness degradation slopes

Loading level groups Percentage of UTS	Stiffness Degradation Slope	MRR predicted at 80 % Life
45	0.0089	0.992
50	0.0506	0.959
55	0.0753	0.939
60	0.1082	0.913
65	0.1862	0.851
80	0.1430	0.887

4.3 Full-Scale Fatigue Testing Results

Testing was conducted on the FIL457 beam in a cantilever bending configuration at 2 Hz loading frequency as discussed in Section 3.3.4. The results of the observed temperature monitoring, stiffness degradation and modal analysis are discussed in this section.

4.3.1 Temperature Monitoring

A thermal imaging camera was used to monitor the temperature at the fixed cantilever clamping point during testing. The ambient conditions in the laboratory, which is not temperature controlled, ranged between approximately 24 °C and 17 °C during testing. The initial recorded surface temperature of the beam before testing commenced was 22.3 °C. Testing was conducted at night and the surface temperature of the beam decreased at the same rate as the ambient temperature. Incremental temperature recordings were made, but the material did not heat up during testing. Temperature build up in the material is therefore not expected to contribute significantly to fatigue life.

4.3.2 Stiffness Degradation

Stiffness was monitored similarly to the specimen fatigue tests where, like in figure 4.7, the slope of the load vs displacement curves of cycle groups was considered at increments spaced approximately 3600 cycles or 30 minutes apart. Figure 4.14 shows a picture taken during full-scale fatigue testing.

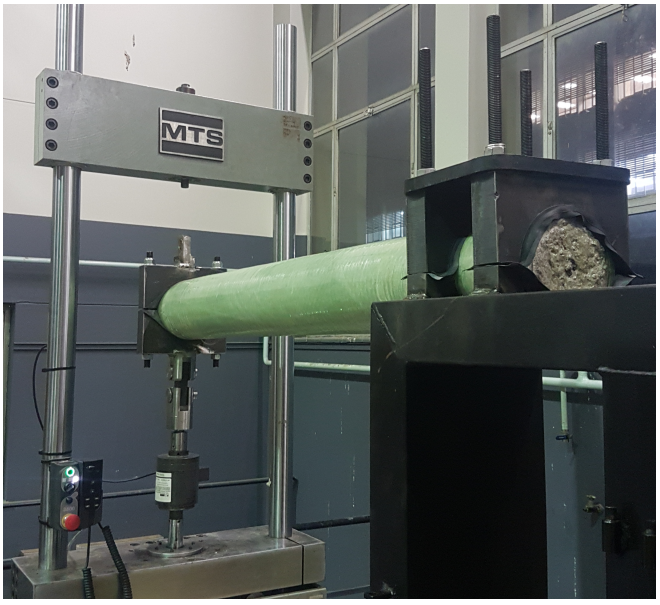

Figure 4.14: Full-scale Testing Set-up

Based on the S-N curve in Figure 4.6, testing was expected to last approximately

30682 cycles until noticeable failure. This proved not to be the case as the test was stopped at 55428 cycles without any visible sign of failure. The stiffness recordings, calculated according to equation 4.3.1, are shown in Figure 4.15 for on logarithmic scale and Figure 4.16 on normalised axes to show the MRR.

$$k = \frac{F}{\delta} = \frac{3EI}{L^3} \tag{4.3.1}$$

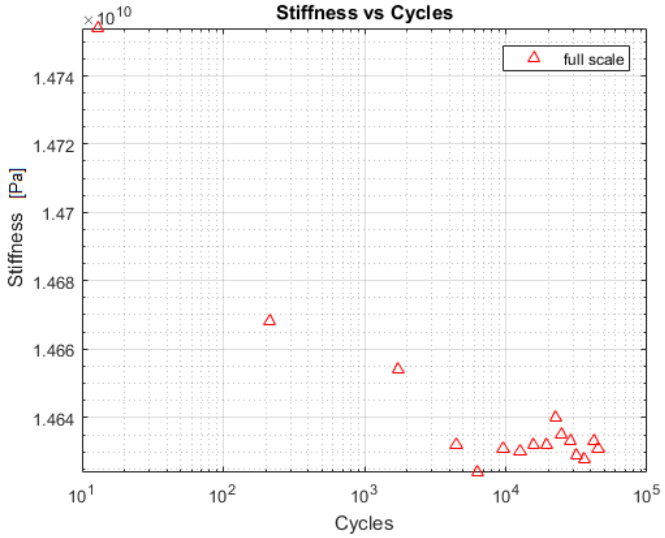

Figure 4.15: Stiffness recordings of full-scale test

The stiffness recorded during full scale testing displayed a rapid initial decrease in stiffness, followed by a period of constant stiffness. The third stage of degradation described by Figure 2.13 could however not be captured.

Finally, a slope of constant degradation cannot be drawn through the first 80 % of the cycles as done in Figure 4.13 since the full scale beam was not tested to failure and the point of 80 % life is unknown. From Figures 4.15 and 4.16 it is observed that the stiffness remains constant at an approximate MRR of around 0.992. With the constant degradation assumption, table 4.4 predicts 80 % of life to occur at an MRR of 0.939. Since a straight line approximation cannot be made here, the best approach would be to consult the two-stage power model to predict when an MRR of 0.939 would occur.

The power model was applied to the data and shown in Figure 4.17. Here the curve fitting constants K and n are 0.991 and -0.008 respectively. The correlation

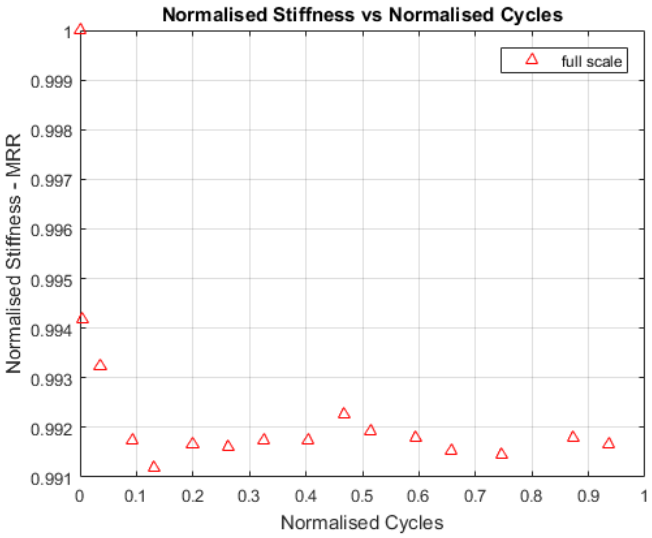

Figure 4.16: Normalised stiffness recordings of full-scale test

coefficient r^2 is equal to 0.815. Since the power function flattens out with an increasing amount of cycles, this model predicts that an MRR of 0.939 will occur after an infinite amount of cycles.

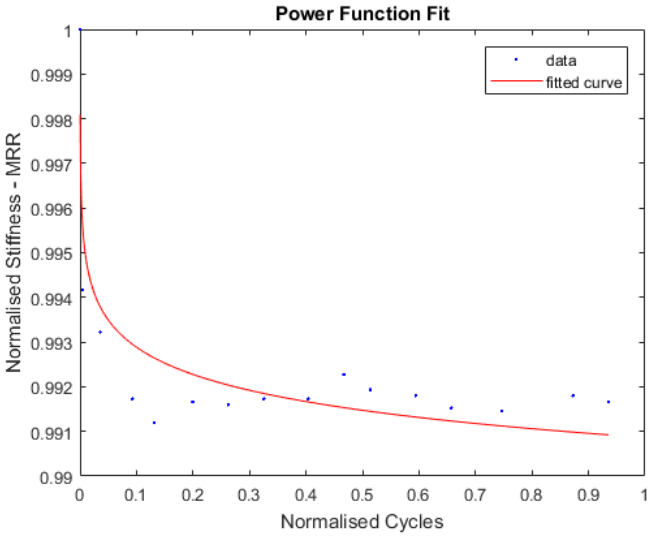

Figure 4.17: Power function fit to stiffness recordings of full-scale test

4.4 Experimental Modal Analysis

Three EMAs with a impact hammer was been done on the full scale beam without the clevises mounted. A Hanning window (Harris, 1978) was applied to the data and the average natural frequency was recorded by FRF to be equal to 39.67 Hz.

The EMAs were done before fatigue testing with the beam mounted on a steel mounting frame which cannot be considered infinitely rigid. This would be regarded an issue if the exact natural frequency of beam was of high importance, but since only the tracking of relative stiffness degradation is of interest, the added effects of the mounting platform is not considered an issue.

Figure 4.18 shows the results of these EMAs. The graph is enlarged to show only the first natural frequency since this is the natural frequency that is compared to the results from the EMA following the full-scale fatigue test.

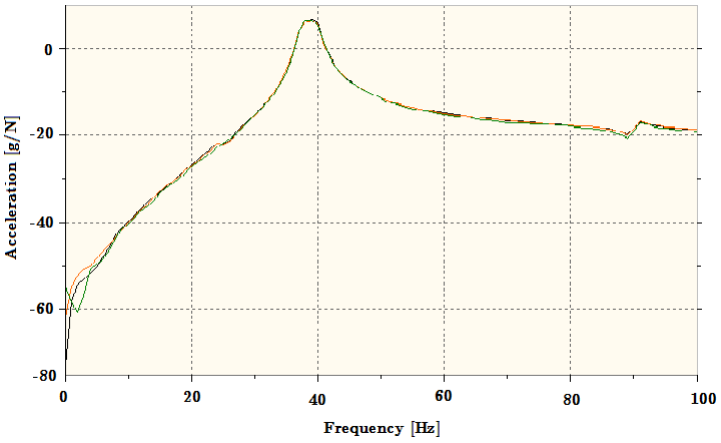

Figure 4.18: Pre-test EMA results enlarged to display first natural frequency (NFFT = 2048), Hanning window, 66 % overlap

A second round of three EMAs was done after at the approximate expected 80 % of life at 24847 cycles of fatigue testing. The average natural frequency was recorded to be equal to 38 Hz. Figure 4.19 shows the results plot enlarged at the first natural frequency. When comparing Figures 4.18 and 4.19, a slight leftward shift can be observed in the peak of the second figure. This leftward shift represents the shift in natural frequency.

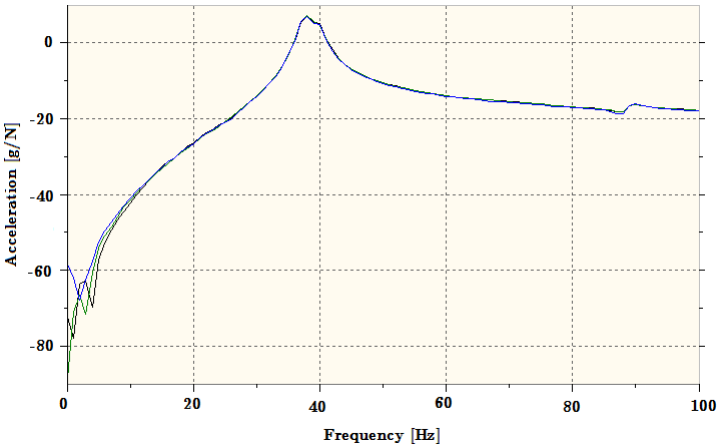

Figure 4.19: EMA results after 25170 cycles enlarged to display first natural frequency (NFFT = 2048), Hanning window, 66 % overlap

Two more EMAs, each repeated three times, were done at 45170 and 51139 cycles. The reason for the relatively small step in cycles between the last two EMAs is because an audible cracking sound was heard from the beam at around 51000 cycles. This indicated that failure might have occured and a EMA was done to investigate. The natural frequency in these last two EMAs were also recorded to be equal to 38 Hz. There is therefore no indication that major failure occurred at around 51000 cycles. Figures B.1 and B.2 in Appendix B show a the results from the second and third modal analyses. Table 4.5 summarises the results from these tests and shows the percentage drop in natural frequency from the first recorded natural frequency.

When these results are illustrated in a diagram as in figure 4.20, the trend represents a two-stage decline which can once again be modelled with a power function in the same way as the stiffness degradation data recorded by the load vs displacement readings. The curve fitting constants K and n are equal to 0.9576 and -0.00148 respectively.

Finally, if the recorded natural frequency is plotted with respect to recorded stiffness along with the same predictive curve as in Figure 3.14, it can be seen that the pre-test recording has a slightly higher natural frequency than analytically predicted and the later natural frequency recordings are slightly lower than predicted. More data would be required for a conclusive trend to be distinguished from this curve, since the four recordings can effectively only be displayed as two points on Figure 4.21.

Table 4.5: Natural frequency recordings summary

Amount of Cycles	First Natural Frequency	Percentage Difference from First Recording
Length	39.67	0
Inner Diameter	38	4.20
Outer Diameter	38	4.20
Wall Thickness	38	4.20

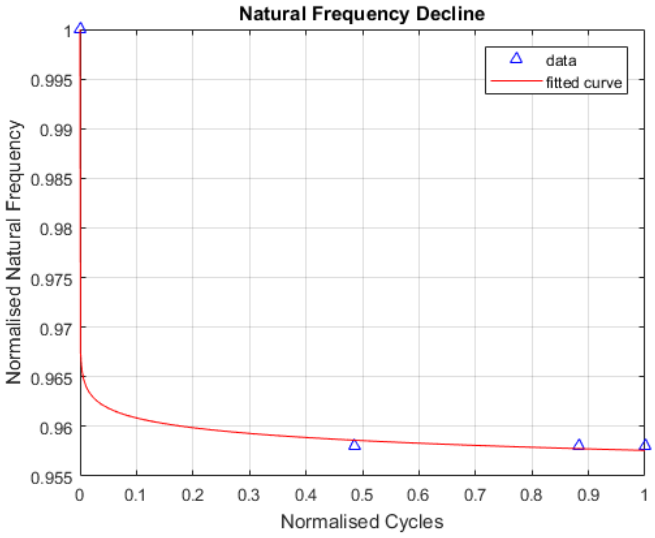

Figure 4.20: Natural frequency decline

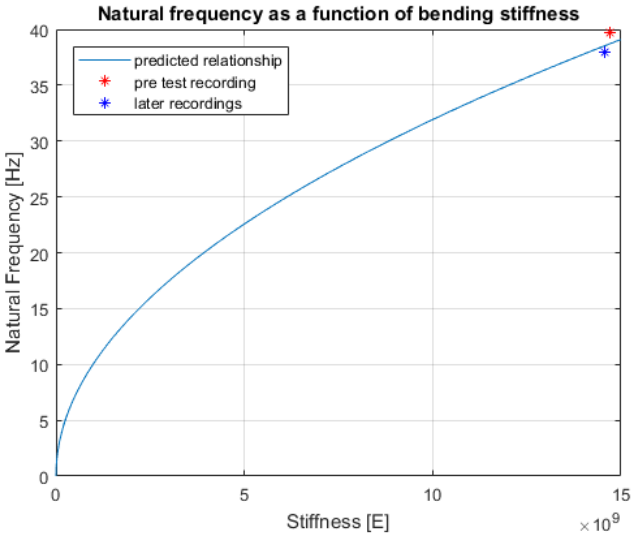

Figure 4.21: Natural frequency decline

Chapter 5

Conclusion

This study was approached to investigate the stiffness degradation under fatigue loading of a GFRP structure similar to the root of the fan blade used in the MinWaterCSP project. Questions about whether results from specimen fatigue tests translate to full-scale surrogate experiment were answered and a condition monitoring method based on investigating stiffness degradation through an EMA was developed. This chapter aims to summarise and contextualise the outcomes of this project and to make recommendations for future work.

5.1 Fatigue Life Findings

Fatigue testing of material specimens yielded an S-N curve with a slope variable of -8.71. This closely correlates with slope variables of research institutions like the Fraunhofer Institute and whose results are published in the OptiDat Database.

Furthermore, stiffness degradation data for the majority of the tests correlated with the expected three-stage stiffness degradation model. However, due to inconsistencies observed in some of the trends, where an initial stage of increasing stiffness was observed, predictions for fatigue life were based on a linear stiffness degradation assumption. This model might be a good approach for maintenance purposes since it is unable to predict the third stage of stiffness degradation and as soon as the measured stiffness values start deviating from the predicted values, part failure might be imminent.

The FIL457 beam could not be tested to failure as predicted by the specimen fatigue testing results. The full-scale specimen therefore proved much more resistant to fatigue than the material specimens tested at the same level. Reasons for

this is speculated to be because of:

1. slight material and manufacturing differences between the laminated specimens and filament wound beam.

2. geometrical interactions of the material where essentially only the top region of the beam cross section is experiencing the full effect of the tension-tension loading along the neutral axis and the other regions that are experiencing different loading states are effectively compensating for the damage caused in the top region.

3. the fact that only one specimen was available for testing statistical variance from the expected point of failure is a possibility.

Nevertheless, the full-scale test did indicate that the loading level used, 55 % UTS at an R-ratio of 0.1, even though significantly elevated from the recorded in-service loading data, is safe for operation to a possible infinite fatigue life. The reason for this conclusion being made, is that the predicted MRR at 80 % of material life is 0.939, and with the observed stiffness degradation trend from full-scale testing, it would take an infinite amount of cycles according to the two-stage power model to reach an MRR of 0.939.

5.2 Condition Monitoring Potential

Incremental experimental modal analyses proved to be a successful condition monitoring method under laboratory conditions. The observed stiffness degradation trend as calculated by load vs displacement data follow the same shape as the trend in natural frequency reduction.

The 4.2 % reduction in natural frequency is much greater than the 0.7 % degradation in stiffness and the natural frequency observed over the same amount of cycles. This more significant difference between initial and final recordings might therefore prove to be a more robust condition monitoring method than techniques that involve load vs displacement (deflection) recordings.

If the natural frequency of a fan blade decreases such that it is equal to any multiple of the fan rotational speed, the fan blade risks going into resonance which will most certainly cause increased damage and potentially premature failure. The potential of monitoring natural frequency reduction is that operators may know exactly what the natural frequency of the fan blade is with respect to the fan rotational speed at any point during the life of the fan.

With a simple set-up requiring the application of only one accelerometer to record the first natural frequency, EMAs on fan blades can potentially become part of an ACC maintenance routine. Additionally, since only a relative decrease in natural frequency is to be detected, the effect of the rigidity or lack thereof in the mounting of the fan blade to the fan hub should play no significant roll as long as it is kept constant over time.

5.3 Future Work

This project has the potential to serve as starting platform for future research in the field of fan blade fatigue. The findings discussed above are not exhaustive and there remains work to be done to refine the work and to expand the potential of providing accurate fatigue predictions. Some areas of possible improvement and future work are discussed in the this final section.

An accelerated constant amplitude load was selected to test the material and full-scale specimen at. Research has been done on variable amplitude equivalent loading sequences which have the potential to increase the ability of laboratory tests to model conditions experienced by the fan blades during actual operation. This investigation would inevitably also have to consider the equipment that will be required to apply variable amplitude sequences.

The cause of the initial increase in material stiffness seen during some of the specimen fatigue tests remain unknown. As mentioned before, a disproportionate decrease in material stiffness can be attributed to a faulty set-up where grip slippage or tabbing effects might be contributing factors. A disproportionate increase in stiffness however suggests that either the material did indeed stiffen slightly, or that the gauge length was somehow decreased. This second option seems unlikely since it must mean that the grips slipped upward while the specimen was under constant tension. To establish the reason for this a follow up study might look into the experimental set-up using different grips and an extensometer suitable for fatigue testing.

Full scale testing and condition monitoring on an actual fan blade is proven to be possible and to have the potential to yield meaningful results. This testing could be done as a possible prototyping test where the decrease in natural frequency can be monitored and if the natural frequency happens to cross a multiple of the fan rotational speed during the lifetime of the prototype, the design might be adapted to ensure that the initial natural frequency is far enough removed from the rotational frequency as not to excite resonance even after the design life of the fan.

Bibliography

Amzallag, C., Gerey, J., Robert, J. and Bahuaud, J. (1994). Standardization of the rainflow counting method for fatigue analysis. *International journal of fatigue*, vol. 16, no. 4, pp. 287–293.

Bailey, P. and Lafferty, A. (2015). Specimen gripping effects in composites fatigue testing–concerns from initial investigation. *Express Polymer Letters*, vol. 9, no. 5.

Cadavid, M.O., Al-Khudairi, O., Hadavinia, H., Goodwin, D. and Liaghat, G. (2017). Experimental studies of stiffness degradation and dissipated energy in glass fibre reinforced polymer composite under fatigue loading. *Polymers & Polymer Composites*, vol. 25, no. 6, p. 435.

D3039/D3039M, A. (2008). Standard test method for tensile properties of polymer matrix composite materials. *ASTM D3039/D3039M*, vol. 3039, p. 2008.

D3479/D3479M, A. (2012). Standard test method for tension-tension fatigue of polymer matrix composite materials. *ASTM D3479/D3479M - 12*.

E1049-85, A. (2003). Standard practices for cycle counting in fatigue analysis. *ASTM E1049-85*.

E739, A. (2015). Standard practice for statistical analysis of linear or linearized stress-life and strain-life fatigue data. *ASTM E739*.

Els, D., Muiyser, J., van der Spuy, J., Meyer, C., Louw, F. and Zapke, A. (2018 April). Performance testing of a retrofitted acc fan. In: *Fan 2018*.

Els, D.N.J. and Muiyser, J. (2016 October). Minwatercsp reference fan testing. Confidential Technical Report: Addendum 3.

Eskom (2016 July). Matimba power station.
Available at: `http://www.eskom.co.za/Whatweredoing/ElectricityGeneration/PowerStations/Pages/MatimbaPowerStation.aspx`

Giancane, S., Panella, F.W. and Dattoma, V. (2010). Characterization of fatigue damage in long fiber epoxy composite laminates. *International Journal of Fatigue*, vol. 32, no. 1, pp. 46–53.

Gibson, R.F. (2011). *Principles of Composite Material Mechanics, Third Edition (Mechanical Engineering)*. CRC Press. ISBN 978-1-4398-5005-3.

Greaves, P.R., Dominy, R.G., Ingram, G.L., Long, H. and Court, R. (2012). Evaluation of dual-axis fatigue testing of large wind turbine blades. *Proceedings of the Institution of Mechanical Engineers, Part C: Journal of Mechanical Engineering Science*, vol. 226, no. 7, pp. 1693–1704.

Harris, F.J. (1978). On the use of windows for harmonic analysis with the discrete fourier transform. *Proceedings of the IEEE*, vol. 66, no. 1, pp. 51–83.

Hashin, Z. and Rotem, A. (1973). A fatigue failure criterion for fiber reinforced materials. *Journal of composite materials*, vol. 7, no. 4, pp. 448–464.

Hernandez-Moreno, H., Douchin, B., Collombet, F., Choqueuse, D. and Davies, P. (2008). Influence of winding pattern on the mechanical behavior of filament wound composite cylinders under external pressure. *Composites Science and Technology*, vol. 68, no. 3-4, pp. 1015–1024.

Inman, D.J. (2013). *Engineering Vibrations*. Pearson Education Limited. ISBN 978-0-273-76844-9.

Jenkins, C. (1920). Materials of construction used in aircraft and aircraft engines. *Report to the Great Britain Aeronautical research committee*.

Kaw, A.K. (2005). *Mechanics of composite materials*. CRC press. ISBN 978-0-8493-1343-1.

Mao, H. and Mahadevan, S. (2002). Fatigue damage modelling of composite materials. *Composite Structures*, vol. 58, no. 4, pp. 405–410.

Matsuishi, M. and Endo, T. (1968). Fatigue of metals subjected to varying stress. *Japanese Society of Mechanical Engineering*.

MinWaterCSP (2018 May). Project.
Available at: `https://www.minwatercsp.eu/`

Mohammadi, B., Fazlali, B. and Salimi-Majd, D. (2017). Development of a continuum damage model for fatigue life prediction of laminated composites. *Composites Part A: Applied Science and Manufacturing*, vol. 93, pp. 163–176.

MSC (2016 April). *Patran 2016 User's Guide*. MSC Software Corporation.

Naderian, H., Cheung, M., Dragomirescu, E. and Mohammadian, M. (2017 May). An optimal numerical scheme for multi-span composite laminated frp deck bridges. In: *6th International Conference on Engineering Mechanics and Materials*.

Nijssen, R. (2006*a*). Optidat - fatigue of wind turbine materials database. *regularly updates via www. wmc. nl*.

Nijssen, R.P.L. (2006*b*). *Fatigue life prediction and strength degradation of wind turbine rotor blade composites*. Knowledge Centre Wind turbine Materials and Constructions. ISBN 978-90-9021221-0.

Owens, G., Cement and Institute, C. (2012). *Fundamentals of Concrete*. Cement and Concrete Institute. ISBN 9780958477970.
Available at: `https://books.google.co.za/books?id=jqoamQEACAAJ`

Palmgren, A. (1959). Ball and roller bearing engineering. *Philadelphia: SKF Industries Inc., 1959*.

Post, N., Case, S. and Lesko, J. (2008). Modeling the variable amplitude fatigue of composite materials: A review and evaluation of the state of the art for spectrum loading. *International Journal of Fatigue*, vol. 30, no. 12, pp. 2064–2086.

Prenscia, H. (2017). *GlyphWorks Worked Examples*, 13th edn.

Schuetz, W. (1996). *A History of Fatigue, Engineering Fracture Mechanics*. Pergamon. ISBN 978-3-642-50835-6.

Schulte, K. (1993). Damage monitoring in polymer matrix structures. *Le Journal de Physique IV*, vol. 3, no. C7, pp. C7–1629.

Shiri, S., Yazdani, M. and Pourgol-Mohammad, M. (2015). A fatigue damage accumulation model based on stiffness degradation of composite materials. *Materials & Design*, vol. 88, pp. 1290–1295.

Siemens, P. (2013 January). *LMS Test.Lab Guide*. LMS.

Solarreserve (2018 July). Redstone.
Available at: `https://www.solarreserve.com/en/global-projects/csp/redstone`

Tsai, S.W. (1968). Strength theories of filamentary structure. *Fundamental aspects of fiber reinforced plastic composites*.

Tsai, S.W. and Wu, E.M. (1971). A general theory of strength for anisotropic materials. *Journal of composite materials*, vol. 5, no. 1, pp. 58–80.

Vassilopoulos, A.P. and Keller, T. (2011). *Fatigue of Fiber-reinforced Composites*. Springer. ISBN 978-1-84996-180-6.

Waddoups, M. (1967). Advanced composite material mechanics for the design and stress analyst. *General dynamics, Fort Worth Division Report FZM-4763, Fort Worth, TX*.

WeatherSA (2018 June). Historical rain maps.
Available at: `http://www.weathersa.co.za/climate/historical-rain-maps`

Whitney, J.M. (1987). *Structural analysis of laminated anisotropic plates*. CRC Press.

Whitworth, H. (1997). A stiffness degradation model for composite laminates under fatigue loading. *Composite structures*, vol. 40, no. 2, pp. 95–101.

Wirsching, P.H., Paez, T.L. and Ortiz, K. (2006). *Random Vibrations*. DOVER PUBN INC. ISBN 0-486-45015-5.

Xia, M., Takayanagi, H. and Kemmochi, K. (2001). Analysis of multi-layered filament-wound composite pipes under internal pressure. *Composite Structures*, vol. 53, no. 4, pp. 483–491.

Appendix A

Additional Stiffness Degradation Results

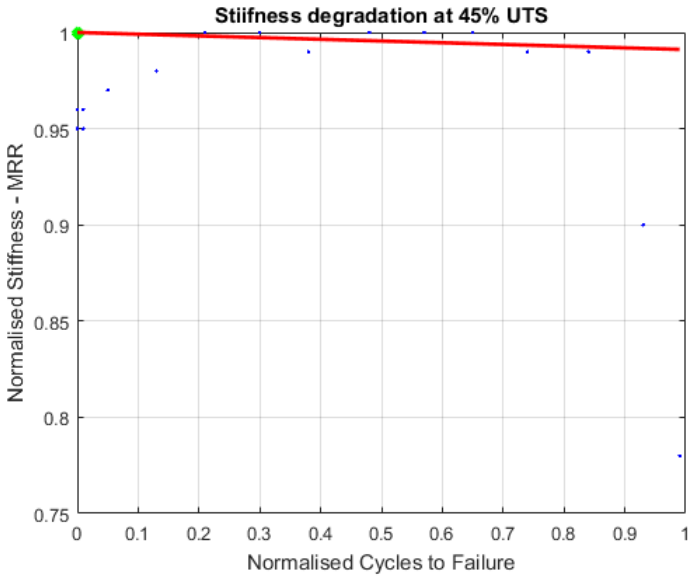

Figure A.1: Stiffness degradation at 45 % UTS

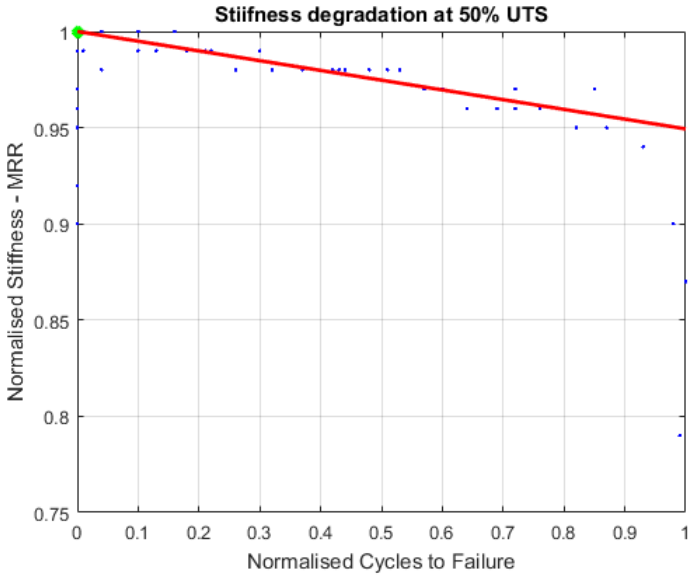

Figure A.2: Stiffness degradation at 50 % UTS

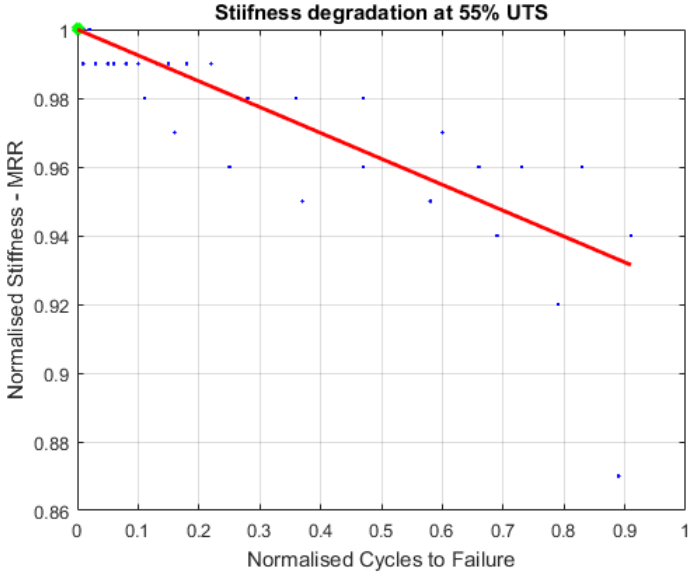

Figure A.3: Stiffness degradation at 55 % UTS

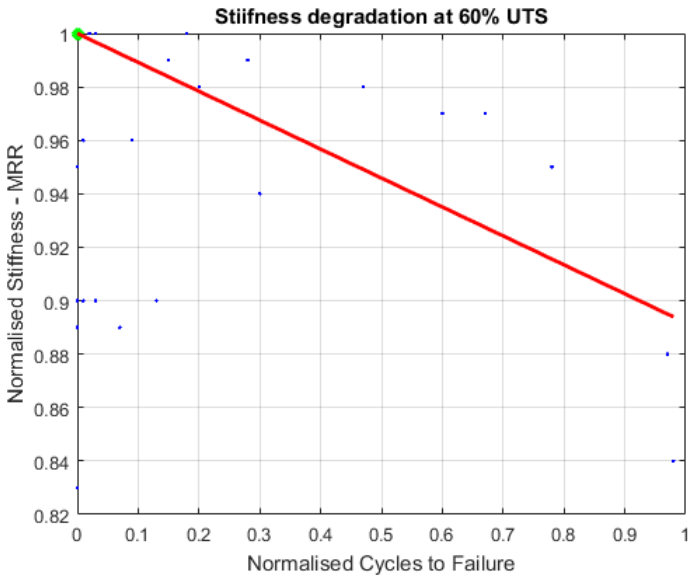

Figure A.4: Stiffness degradation at 60 % UTS

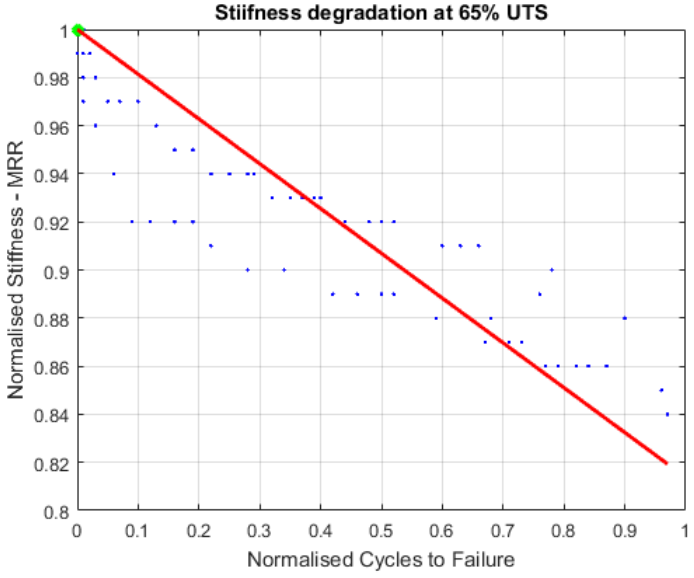

Figure A.5: Stiffness degradation at 65 % UTS

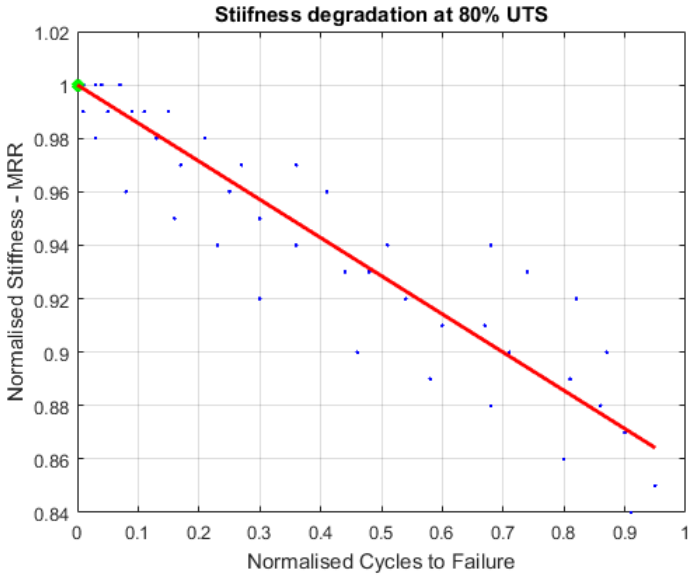

Figure A.6: Stiffness degradation at 80 % UTS

Appendix B

Additional EMA Results

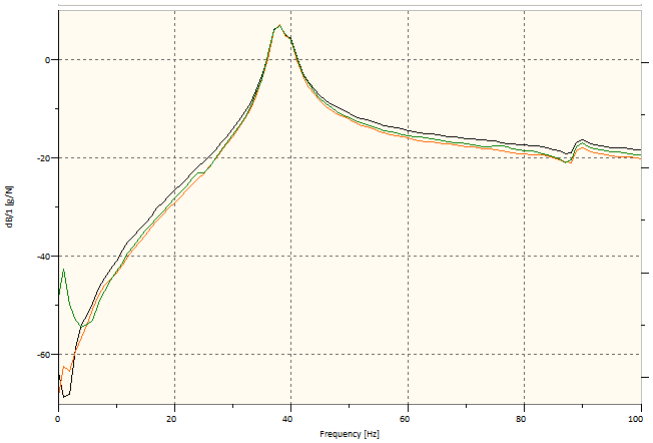

Figure B.1: EMA results after 45170 cycles enlarged to display first natural frequency (NFFT = 2048), Hanning window, 66 % overlap

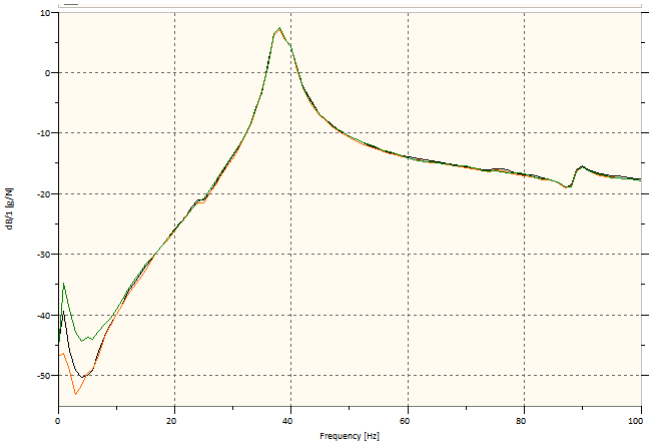

Figure B.2: EMA results after 51139 cycles enlarged to display first natural frequency (NFFT = 2048), Hanning window, 66 % overlap

Appendix C

Specification Documents

AERONTEC cc
www.aerontec.co.za

product data sheet

AEROTEX E-BX 450

E-Glass Fabric, stitched ± 45° at 450 g/m²

E-glass biaxial stitched roving for all composite applications.

The biaxial ± 45° weave assists in draping in difficult areas and is generally preferred due to better strength, “softness” and better wet-out and lower resin ratio usage.

Total Weight	450 g/m²
Standard Width	127cm / 50”
Weight Ratio +45° / -45°	50 : 50
Finish / sizing	Silane

AERONTEC cc
info@aerontec.co.za
www.aerontec.co.za
ISO9001:2008 Certified
AS9120 Certified

"UniGlass" Unidirectional Glass Fabric

Features:

100% E-glass in longitudinal direction
Excellent mechanical properties achieved
Predictable and repeatable properties achieved
Stable handling, even through wet-out machine
Will not unravel when cut, even when cutting on the diagonal
Excellent wet-out and good fibre to resin ratios achievable
Soft and formable
Greater strength and higher stiffness
Better impact resistance with correct selection of resin
Suffers less from fatigue

General Data:

500 g/sq.m, or other weights to be specified
Bonded with heat formed threads.

Typical properties with 70% UniGlass / 30% resin, fully cured:

Tensile strength with 70% UniGlass glass	1100	MN/m²
Tensile modulus with 70% UniGlass glass	42	GN/m²
Compressive strength with 70% UniGlass glass	400	MN/m²
Flexural strength with 70% UniGlass glass	1200	MN/m²
Flexural modulus with 70% UniGlass glass	40	GN/m²

EPOXYDHARZ L 1100
EPOXY RESIN L 1100

EPOXYDHARZ L 1100

STANDARD-LAMINIER- UND KLEBEHARZ

Beschreibung

- **Ungefüllt, lösungsmittelfrei**
- **niedrige Verarbeitungsviskositäten**
- **Verarbeitungszeiten individuell einstellbar**
- **gutes Benetzungsverhalten von Glas-, Kohlenstoff- und Aramid- Fasern**
- **hochbelastbare Faserverbundbauteile**
- **sehr gute dynamische Festigkeiten**
- **gute Wärmeformbeständigkeiten bei niedrigen Härtetemperaturen**
- **Zulassungen nach Germanischer Lloyd**

Das Epoxidharz EPIKOTE™ Resin L 1100 ist ein kaltanhärtendes, lösungsmittelfreies, ungefülltes 2-Komponenten-System und ergibt in der Kombination mit den Aminhärtern EPIKURE™ Curing Agent 294, EPIKURE™ Curing Agent 295 und EPIKURE™ Curing Agent 296 hochbelastbare Faserverbundbauteile mit sehr guten dynamischen Festigkeiten und sehr geringen Ermüdungseigenschaften. Die Harzsysteme besitzen hervorragende Tränkeigenschaften gegenüber Glas-, Kohlenstoff- und Aramid- Fasern und besitzen Zulassungen nach Germanischer Lloyd und eignen sich daher speziell für Pultrusions- und Injektionsverfahren (RTM, SCRIMP / VARI) im Windenergieanlagen-, Boots-, Schiffs-, Sportgeräte-, Formen- und Vorrichtungsbau.

Verarbeitung

Arbeitsphysiologische Hinweise:
Nach Möglichkeit soll der direkte Kontakt der Hände sowohl mit den einzelnen Komponenten, als auch mit der Mischung vermieden werden. Das Säubern der Hände mit Lösungsmitteln soll auf jeden Fall unterbleiben, da Lösungsmittel das natürliche Fett der Haut entziehen und schädigende Stoffe über die Lösung in die Hautporen gelangen können. Des weiteren verweisen wir auf die in den EG- Sicherheitsdatenblättern gemachten Angaben. Empfehlenswert sind Arbeitsschutzsalben.

Mischen:
Das Epoxidharz EPIKOTE™ Resin L 1100 wird mit dem jeweiligen Härter in dem angegebenen Mischungsverhältnis zusammengegeben. Nach intensivem Mischen ist die Masse sofort gebrauchsfertig.
Harz und Härter müsen miteinander vollständig und schlierenfrei gemischt werden. Dabei ist auf die Einhaltung des angegebenen Mischungsverhältnisses zu achten. Die Reaktionsgeschwindigkeit kann keinesfalls durch eine Erhöhung oder Reduzierung des Härteranteils beeinflusst werden. Größere Ungenauigkeiten bei der Einwaage können zu einer unvollständigen Aushärtung des Laminates führen und können nicht mehr durch eine Nachbehandlung korrigiert werden.

Gebrauchsdauer:
Die unterschiedlichen Verarbeitungszeiten wurden an 100 g Ansätzen bei 20 - 25 °C gemessen. Größere Ansätze sollten nur angemischt werden, wenn eine zügige Verarbeitung innerhalb der vorgegebenen Gebrauchsdauer möglich ist.

- EPIKOTE™Resin L 1100 – EPIKURE™ Curing Agent 294 ~ 400 Minuten
- EPIKOTE™Resin L 1100 – EPIKURE™ Curing Agent 295 ~ 15 Minuten
- EPIKOTE™Resin L 1100 – EPIKURE™ Curing Agent 296 ~ 25 Minuten

EPOXY RESIN L 1100

STANDARD LAMINATING AND ADHESIVE RESIN

Description

- ***free of fillers and solvents***
- ***low processing viscosities***
- ***individually configurable processing times***
- ***good wetting behaviour on glass, carbon, and aramid fibres***
- ***high-strength fibre composite components***
- ***superior dynamic strength values***
- ***good heat distortion properties at low curing temperatures***
- ***approved by Germanische Lloyd***

The epoxy resin EPIKOTE™ L 1100 is a cold-curing, solvent- and filler-free double-constituent system that yields in combination with the amine curing agents EPIKURE™ 294, 295 and 296 high-strength fibre composite components with superior dynamic strength values and ultra low fatigue properties. These resin systems exhibit outstanding impregnating properties on glass, carbon, and aramid fibres, are approved by Germanische Lloyd, and are therefore ideal specifically for pultrusion and injection moulding (RTM, SCRIMP/ VARI) for wind turbines, boat and ship building, sports equipment, moulds, and jigs.

Processing

Ergonomic information:
Whenever possible you should avoid direct skin contact with any of the constituents or the mixture. You should never wash your hands with solvents, which removes the skin's natural grease and allows harmful substances from the solution to pass through the skin's pores. In addition we refer to the specifications listed on the EC safety data sheets. We recommend barrier creams.

Mixing
The epoxy resin EPIKOTE™ L 1100 and its curing agent are mixed in the specified ratio. After intensive mixing the compound is ready for use.
The resin and curing agent must be mixed thoroughly and uniformly at the specified mixing ratio. Under no circumstances can the reaction rate be influenced by a higher or lower fraction of curing agent. Large differences in the mixing ratio can lead to imperfect curing in the laminate that can no longer be rectified by post-treatment.

Pot life
The following processing times were measured on 100 g formulations at 20–25 °C. Larger formulations should be mixed only when they can be processed quickly within the specified pot life.

- *EPIKOTE™Resin L 1100 – EPIKURE™ Curing Agent 294 ~ 400 minutes*
- *EPIKOTE™Resin L 1100 – EPIKURE™ Curing Agent 295 ~ 15 minutes*
- *EPIKOTE™Resin L 1100 – EPIKURE™ Curing Agent 296 ~ 25 minutes*

Die Härter EPIKURE™ Curing Agent 294, 295, und EPIKURE™ Curing Agent 296 sind alle in allen Mischungsverhältnissen miteinander mischbar, so dass durch Abmischung der Härter untereinander beliebige Topfzeiten innerhalb der Verarbeitungszeiten der einzelnen Härter eingestellt werden können.
Da bei allen Härtern das Mischungsverhältnis zur Stammkomponente EPIKOTE™ Resin L 1100 identisch ist, bleibt das Mischungsverhältnis der Härterabmischung konstant bei 100 : 30 Gewichtsteilen.

The curing agents EPIKURE™ 294, 295 and 296 can all be mixed with each other at all mixing ratios for individual pot lives within their processing times.
The mixing ratio for the standard resin constituent EPIKOTE™ L 1100 is identical for all curing agents, so this resin constituent can be mixed at the constant ratio of 100:30 parts by weight.

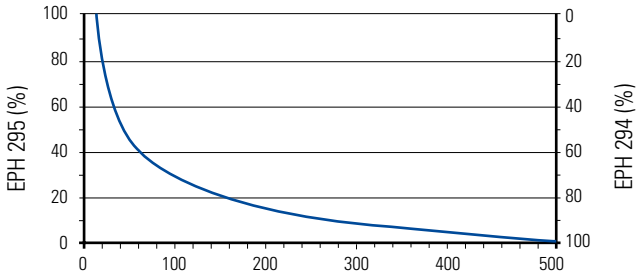

Applikation:
Die Verarbeitungszeit des 2- Komponenten Laminiersystems EPIKOTE™ Resin L 1100 ist, wie bei allen kalthärtenden Systemen begrenzt, und wird durch die Ausgangstemperatur der Komponenten und dem exothermen Reaktionsverlauf beeinflusst. Die unterschiedlichen Verarbeitungszeiten wurden an 100 g Ansätzen bei 20 - 25 °C gemessen. Größere Ansätze sollten nur angemischt werden, wenn eine zügige Verarbeitung innerhalb der vorgegebenen Gebrauchsdauer möglich ist.
Diese Faktoren sind vor allem für die manuelle Verarbeitung wichtig.

Application:
Like all cold-curing systems, the processing time for the double constituent laminating system resin EPIKOTE™ L 1100 is limited and is affected by the initial temperature of the constituents and the exothermal reaction course. The following processing times were measured on 100 g formulations at 20–25 °C. Larger formulatio
These factors are important above all for manual processing.

Vorsichtsmaßnahmen

Hinweise zum sachgemäßen Umgang mit EPIKOTE™–Epoxydharzen und EPIKURE™–Härtern entnehmen Sie bitte den entsprechenden Sicherheitsdatenblättern.

Precautionary measures

Instructions on the proper handling of EPIKOTE™ epoxy resins and curing agents can be taken from the corresponding safety data sheets.

Lagerung

In sorgfältig geschlossenen Originalgebinden sind Harze und Härter mindestens 12 Monate lang lagerfähig. Bei Temperaturen unter + 15 °C können Harze und Härter kristallisieren, sichtbar durch eine Eintrübung bzw. Verfestigung des Behälterinhaltes. Vor der Verarbeitung muß die Kristallisation durch Erwärmen beseitigt werden. Durch langsames Erwärmen auf ca. 50 - 60 °C im Wasserbad oder im Temperofen und durch Umrühren oder Schütteln wird eine Kristallisation ohne Qualitätsbeeinträchtigung beseitigt. Nur vollkommen transparente Produkte verarbeiten! Vorsicht beim Erwärmen! Behälter vor dem Erwärmen etwas öffnen, damit Druckausgleich stattfinden kann. Niemals den Behälter mit offener Flamme erwärmen! Beim Umrühren der erwärmten Produkte Schutzausrüstung (Schutzbrille, Schutzhandschuhe und Atemschutz) verwenden.

Storage

The resins and hardeners can be stored at least 12 months in their carefully sealed original containers. The resins and hardeners may crystallize at temperatures below +15 °C (60 °F). The crystallization is visible as a clouding or solidification of the contents of the container. Before processing, the crystallization must be removed by warming up. Slow warming up to approx. 50 - 60 °C (120 - 140 °F) in a water bath or oven and stirring or shaking will clarify the contents of the container without any loss of quality. Use only completely transparent products. Before warming up, open containers slightly to permit equalization of pressure. Caution during warm-up! Do not warm up over an open flame! While stirring up use safety equipment (gloves, eyeglasses, respirator).

Packungsgrößen von 0,5 kg bis 200 kg
Bestell-Nr. 103 100-X

Package sizes from 0.5 to 200 kg
Order no. 103 100-X

Einsatzgebiet für L 1100/Härter EPH 294 (langsam):
Große Bauteile wie z.B. Windkraftflügel, Formen und Bootsrümpfe

Applications for L 1100/ hardener EPH 294 (slow-curing): large components, e.g. wind turbine blades, mould, and hulls

EPOXYDHARZ L 1100
EPOXY RESIN L 1100

Daten — *Specifications*

Epoxydharz L 1100 ***Epoxy resin L 1100***	**Einheit** ***Unit***	**Wert** ***Value***
Dichte bei 20 °C *Density at 20°C*	g/cm³	1,15 ± 0,01
Viskosität bei 25 °C *Viscosity at 25 °C*	mPa·s	1.600 ± 200
Epoxydäquivalent *Epoxy equivalent*	g/Äquivalent *g/Equivalent*	192 ± 5

Härter — *Hardener*

Eigenschaften ***Properties***	**Einheit** ***Unit***	**Epikure™ curing agent 294**	**Epikure™ curing agent 295**	**Epikure™ curing agent 296**
Viskosität bei 25 °C *Viscosity at 25 °C*	mPa·s	10 ± 5	30 ± 10	400 ± 125
Mischviskosität bei 25 °C *Mixing viscosity at 25 °C*	mPa·s	~ 290	~ 380	650 ± 200
Aminäquivalent *Amine equivalent*	g/Äquiv. *g/Equiv.*	56 ± 2	55 ± 2	58 ± 2
Dichte bei 20 °C *Density at 20 °C*	g/cm³	0,934 ± 0,020	0,974 ± 0,020	1,07 ± 0,02
Mischungsverhältnis *Mixing ratio*	Gewichtsteile *parts per weight*	100:30 ± 2	100:30 ± 2	100:30 ± 2

Typische Aushärtebedingungen EPIKOTE™ Resin L 1100 — *Typical curing conditions for EPIKOTE™ resin L 1100*

	Epikure™ curing agent 294	**Epikure™ curing agent 295**	**Epikure™ curing agent 296**
Anhärtung *Preliminary curing*	15 h/20 - 25 °C	10 h/20 - 25 °C	10 h/20 - 25 °C
Nachhärtung *Post curing*	10 h/70 °C	15 h/50 - 80 °C	15 h/50 - 80 °C

Typische Formstoffeigenschaften des verstärkten EPIKOTE™ Resin L 1100 / EPIKURE™ Curing Agent 294

Die Werte wurden an 2 mm Platten (8 Lagen Gewebe 181 / Interglas 91745) gemessen. Die Härtung erfolgte über 15 Stunden bei Raumtemperatur und einer anschließenden Nachhärtung von 10 Stunden bei 70°C bzw. 10 Stunden bei 80°C.

Typical moulded properties of reinforced EPIKOTE™ L 1100 resin and EPIKURE™ 294 curing agent

The values were measured on 2 mm sheets (eight plies of 181 fabric and 91745 Interglas) that were cured for fifteen hours at room temperature and then post-cured for ten hours at 70 °C and ten hours at 80 °C.

Eigenschaften ***Properties***	**Einheit** ***Unit***	**Wert** ***Value***	**a)**	**b)**
Härtung *Curing*			10 h 70 °C	10 h 80 °C
Biegefestigkeit *Flexural strength*	MPa		445	488
E-Modul (aus Biegeversuch) (DIN 53457) *Modulus of elasticity (flexural modulus)*	MPa		22.600	18.000
ILS *ILS*	MPa		35	36
Glasübergabgstemperatur Tg (TMA) *Glass transition temperature Tg (TMA)*	°C		80	88

Typische Formstoffeigenschaften des unverstärkten EPIKOTE™ Resin L 1100

Die Werte wurden an 4 mm Reinharzplatten gemessen. Die Härtung erfolgte über 15 Stunden bei Raumtemperatur und einer anschließenden Nachhärtung von 2 Stunden bei 60 °C und 2 Stunden bei 70 °C.

Typical moulded properties of unreinforced EPIKOTE™ L 1100 resin

The values were measured on 4 mm pure resin sheets that were cured for fifteen hours at room temperature and then post-cured for two hours at 60 °C and two hours at 70 °C.

Eigenschaften ***Properties***	**Norm** ***Standards***	**Einheit** ***Unit***	**Epikure™ curing agent 294**	**Epikure™ curing agent 295**	**Epikure™ curing agent 296**
Dichte 20 °C *Density at 20 °C*	DIN 53479	g/cm³	1,135	1,144	1,1837
Zugfestigkeit *Tensile strength*	DIN 53455	MPa	65,4	69,8	83,0
Bruchdehnung (Zug) *Elongation at break (tensile)*	DIN 53455	%	9,0	4,5	5,3
E-Modul (Zug) *Tensile modulus*	DIN 53457	MPa	3160	3080	3455
Biegefestigkeit *Flexural strength*	DIN 53452	MPa	110	114,8	130,9
E-Modul (Biegung) *Flexural modulus*	DIN 53457	MPa	2730	2476	3097
Barcol - Härte *Barcol - hardness*			28 ±2	28 ±2	
Glasübergangstemperatur Tg, (TMA) *Glass transition temperature Tg, (TMA)*		°C	80	80,4	85,5
Wasseraufnahme Gew. % *Water absorption % by weight*	DIN 53495	24 h, 23 °C 168 h, 23 °C	0,13 0,34	0,145 0,368	0,114 0,287

Abhängigkeit der Glasübergangstemperatur von den Härtebedingungen

Zum Erreichen des hohen mechanischen Eigenschaftsprofils des Faserverbundbauteils empfielt sich eine Nachtemperung. Der Anstieg der Glasübergangstemperatur während dieser Nachtemperungsschrittes wird im Allgemeinen als Indikator für die Vollständigkeit des Reaktionsumsatzes Harz - Härter herangezogen.

Relationship between glass transition temperature and curing conditions

The recommended procedure for obtaining high strength properties on the fibre composite component involves post-annealing. The rise in the glass transition temperature during post-annealing can generally be taken as an indication of how far the reaction has taken place in the resin and curing agent.

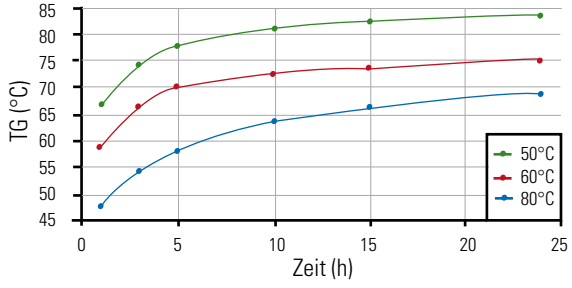

Anstieg der Glasübergangstemperaturen bei verschiedenen Temperaturen mit dem Härter EPH 294.

Rise in glass transition temperatures at various temperatures with the curing agent EPH 294.

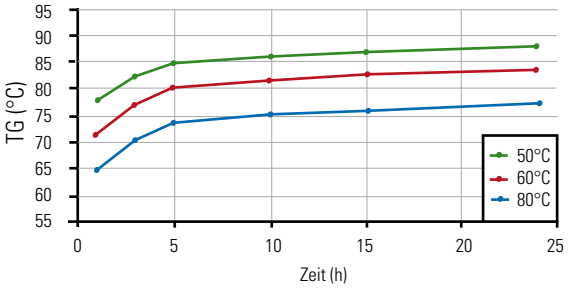

Anstieg der Glasübergangstemperaturen bei verschiedenen Temperaturen mit den Härtern EPH 295 und EPH 296.

Rise in glass transition temperatures at various temperatures with the curing agents EPH 295 and EPH 296.

JUSHI™

386T Direct Roving

For Filament winding, pultrusion, Weaving

386T Direct Roving is coated with a silane-based sizing compatible with unsaturated polyester, vinyl ester and epoxy resins and designed for filament winding, pultrusion and weaving applications.
386T is based on the JUE06 glass formulation newly launched by Jushi and has better mechanical properties, chemical corrosion resistance and high temperature resistance. It can be widely used in corrosion resistance applications such as FRP pipes, pressure vessels and gratings and high temperature applications such as temperature resistance profiles. The product can also be used to weave multi-axial fabrics for polyester-based large wind blades.

Product Features

- ◎ Good processing characteristics and low fuzz
- ◎ Multi-compatible sizing
- ◎ Rapid and complete wet-out
- ◎ High composite mechanical properties
- ◎ Excellent chemical corrosion resistance

Identification

Glass Type	E6									
Type of Size	Silane									
Size Code	386T									
Tex	300 735	200 400	600	900	1100 1200	1500	1700	2200	2400 4800	9600
Filament Diameter	14	16	17	15	17	18	19	22	24	31

Technical Parameters

Linear Density (%)	Moisture Content (%)	Size Content (%)	Breakage Strength (N/tex)
ISO 1889	ISO 3344	ISO 1887	ISO 3341
±5	⩽ 0.10	0.55 ± 0.15	⩾0.40

Mechanical Properties

Mechanical Properties	Unit	Value	Resin	Method
Tensile Strength	MPa	2657	U P	ASTM D2343
Tensile Modulus	MPa	80132	U P	ASTM D2343
Tensile Strength	MPa	2367	E P	ASTM D2343
Tensile Modulus	MPa	80526	E P	ASTM D2343

The above data are actual experimental values for E6DR17-1200-386T and for reference only.

Storage

Unless otherwise specified, fiberglass products should be stored in a dry, cool and rain-proof area. It is recommended that the room temperature and humidity should be always maintained at 20℃～25℃ and 35%~65% respectively. To ensure safety and avoid damage to the product, the pallets should not be stacked more than three layers high. When the pallets are stacked in 2 or 3 layers, care should be taken to correctly and smoothly move the top pallet.

* It is recommended to use the production preferably within 12 months.

Packaging

* The product can be packed on pallet or in small cardboard boxes.

Package height mm (in)	260 (10)	260 (10)
Package inside diameter mm (in)	160 (6.3)	160 (6.3)
Package outside diameter mm (in)	270 (10.6)	310 (12.2)
Package weight kg (lb)	15.6 (34.4)	22 (48.5)

Number of layers	3	4	3	4
Number of doffs per layer	16		12	
Number of doffs per pallet	48	64	36	48
Net weight per pallet kg (in)	750 (1653.4)	1000 (2204.6)	792 (1746)	1056 (2328)

Pallet length mm (in)	1120 (44)		1270 (50)	
Pallet width mm (in)	1120 (44)		960 (37.8)	
Pallet height mm (in)	940 (37)	1180 (46.5)	940 (37)	1180 (46.5)

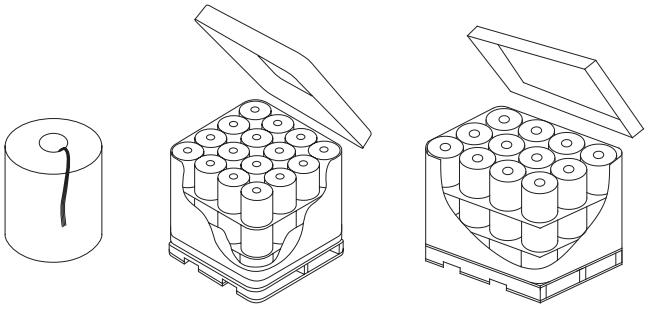

JUSHI GROUP CO., LTD.

Add: Tongxiang Economic Development Zone, Zhejiang 314500, PRC
Domestic Sales: +86-573-88181016 Fax:+86-573-88136222
Http://www.jushi.com E-mail:info@jushi.com
International Sales: +86-573-88181026 Fax:+86-573-88181058
Customer Service: +86-573-88181017 Fax:+86-573-88181388

Pretoria (Head office)
Tel: +27 12 664 5696
+27 12 664 5697
Fax: +27 12 664 2682

Physical address
1007 Kruger Avenue
Lyttelton Manor
Centurion
South Africa
0157

Postal address
P O Box 14057
Lyttelton
0140
SOUTH AFRICA

Cape Town
Tel: +27 21 981 3541
Fax: +27 86 618 3145

Factory #2
Cnr Frans Conradie Drive &
Kenwill Road
Brackenfell
Okavongo Park

E-mail: mms@mmstechno.co.za
Web: www.mmstechnology.co.za

TEGNOLOGIE (EDMS) BPK TECHNOLOGY (PTY) LTD
Reg. No. 2005 / 016454 / 07

MEGANIKA MATERIALE STRUKTURE MECHANICS MATERIALS STRUCTURES

7 May 2018 Q5047-18

University Stellenbosch
Department of Mechanical Engineering

Attention: Arno Olivier

QUOTATION Q5047-18: GRP Test Specimens

Thank you for the opportunity to present a quotation for manufacturing of GRP test specimens. The following important points should be noted.

1. Work Content

- Manufacture of GRP sheet.
- Cut to specimen size.
- Glue tabs into place.

2. Cost

The cost excluding VAT are as follows:

Item	Description	Unit Price	Quantity	Price (Excl. VAT)
1	**GRP test specimen x40**	R 8 190	1	R 8 190-00

3. Deliverables

The following items are considered deliverables for the project:

- GRP sheet consisting of biax 450gsm fibre glass, UD 500gsm fibre glass and epoxy resin, infused and cut to size 155mm x 12mm x ±4mm.
- GRP infused tabs of size 55m x 12mm x ±3mm bonded onto the specimen with an epoxy adhesive (four on each).

4. Exclusions

- Any changes to the specifications, necessitating a redesign of the original design, are excluded and will be treated separately after re-negotiation of cost and schedule.

5. Schedule

15 Working days from received order.

6. Payment Conditions

The following payment conditions are applicable.

6.1 On completion and acceptance of each phase of the project that phase will be invoiced.
6.2 Payment strictly 30 days after delivery and invoice.
6.3 A 50% deposit will be needed before work will commence.

7. Special Conditions

7.1 Cancellation of contract.
In the event of an order being cancelled before completion, all costs incurred up to date of cancellation will be invoiced.

7.2 Change in project scope and or delay in schedule.
In the event of changes in the project scope:

- The changes shall be mutually agreed upon in writing.
- The project cost will be adjusted accordingly.

8. Validity of Proposal

This proposal is valid for 40 days.

Should there be any queries please do not hesitate to call. Thanking you again for the opportunity to provide this quotation.

Yours faithfully.

Leon D. More (Jnr)

TEGNOLOGIE (EDMS) BPK TECHNOLOGY (PTY) LTD
Reg. No. 2005 / 016454 / 07

SR 8100

Epoxy system for Injection and Infusion

The **SR 8100** is a two component epoxy system. It has been specially formulated for resin transfer processes, such as injection or infusion.
This system has a very low viscosity at ambient temperature.
The different hardeners allow the moulding of small to very large parts.
The cured system gives a temperature resistance up to 80°C (Tg onset)
The hardeners SD 4770 and 4771 are designed for very thick fibers laminates

Epoxy resin SR 8100

Aspect / colour		Yellow liquid
Viscosity (mPa.s)	@ 15 °C @ 20 °C @ 25 °C @ 30 °C @ 40 °C	2370 ± 480 1320 ± 260 785 ± 155 490 ± 100 220 ± 45
Density (g/cm^3)	@ 20 °C	1.158
Storage stability	Ambiant	24 Months

Hardeners SD 8822 SD 477x

Reference Reactivity type		SD 8822 **"slow"**	SD 4772 **Slow**	SD 4771 **Ultra slow**	SD 4770 **Mega slow**
Aspect / colour Color Gardner		Light yellow liquid 5 maximum	Light yellow liquid 3 maximum		
Viscosity (mPa.s)	@ 15 °C @ 20 °C @ 25 °C @ 30 °C @ 40 °C	27 ± 5 20 ± 5 16 ± 5 13 ± 5 9 ± 5	13 ± 3 11 ± 2 9 ± 2 7 ± 1.5 5 ± 1		
Storage stability	15 to 25 °C	24 months Hardeners react with carbon dioxide and moisture. Keep tightly closed packaging, minimize maximum contact with the air.			
Density (g/cm^3)	@ 20 °C	0.935	0.927	0.944	0.944

SR 8100 / SD 8822 SD 477x Mixes

Reference		**SR 8100 / SD 8822**	**SR 8100 / SD 4472**	**SR 8100 / SD 4471**	**SR 8100 / SD4770**
Mixing ratio by weight		**100 g / 31 g**	**100 g / 29 g**		
Mixing ratio by volume		**100 ml / 39 ml**	**100ml / 36 ml**		
Initial viscosities	@ 20 °C @ 30 °C	390 250	330 150	400 160	300 145

Sicomin, 31 avenue de la Lardière, 13220 Châteauneuf les Martigues, France
T: +33 (0)4 42 42 30 20 / F: +33 (0)4 42 81 29 29 / E: info@sicomin.com / www.sicomin.com

Reactivity on 500 gr mix @ 20 °C

	SR 8100 / SD 8822	**SR 8100 / SD 4772**	**SR 8100 / SD 4771**	**SR 8100 / SD 4770**
Exothermic temperature (°C)	220	240	200	180
Time to reach the exothermic peak	4 hrs	3 hrs 45’	5 hrs 15’	7 hrs 20’
Time to reach 50 °C	3 hrs 40’	2 h 20’	4 hrs 40’	6 hrs 30’

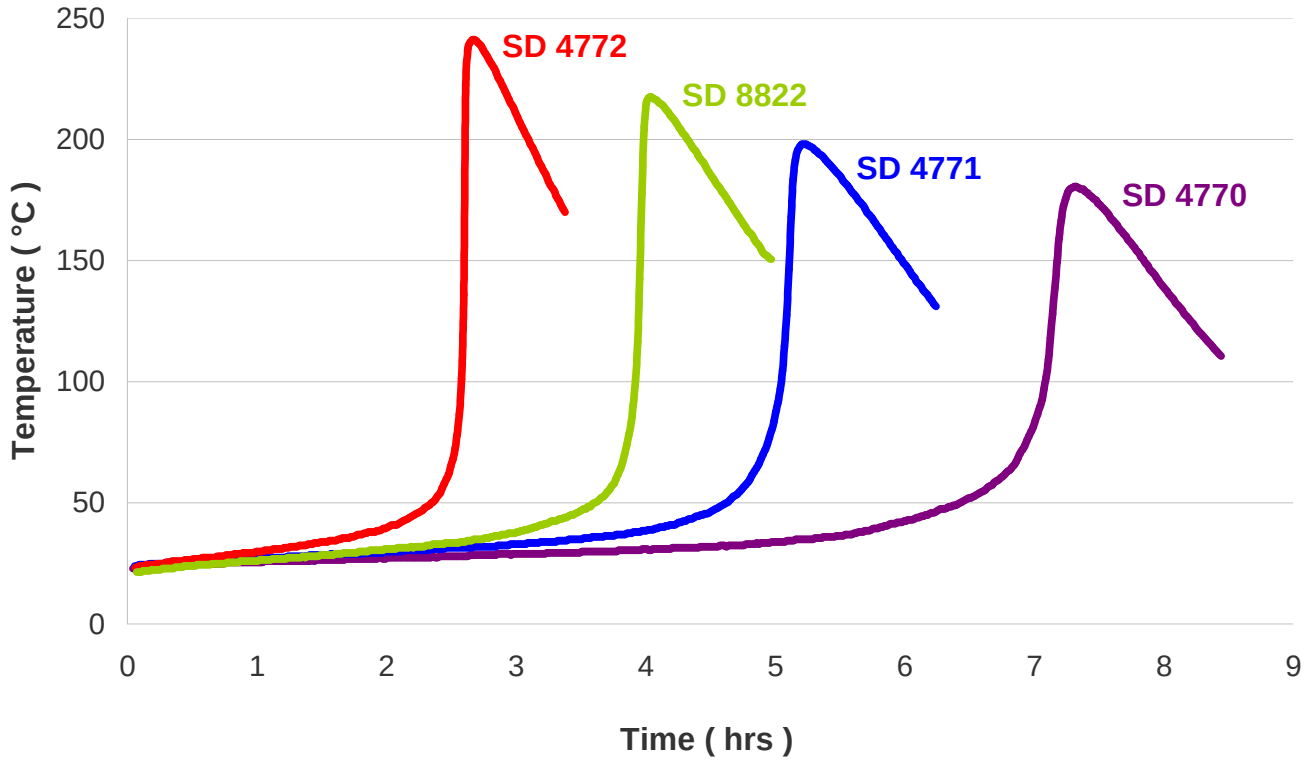

Physical tests according standard ::

Gardner color:	*NF EN ISO 4630*	*Visual metod*
Refractive index :	*NF ISO 280*	
Viscosity:	*NF EN ISO 3219*	*Rheometer 50 mm, shear $10s^{-1}$*
Density:	*NF EN ISO 2811-1*	*Pyknometer*

Viscosities increase on 1 mm film thickness

@ 20 °C

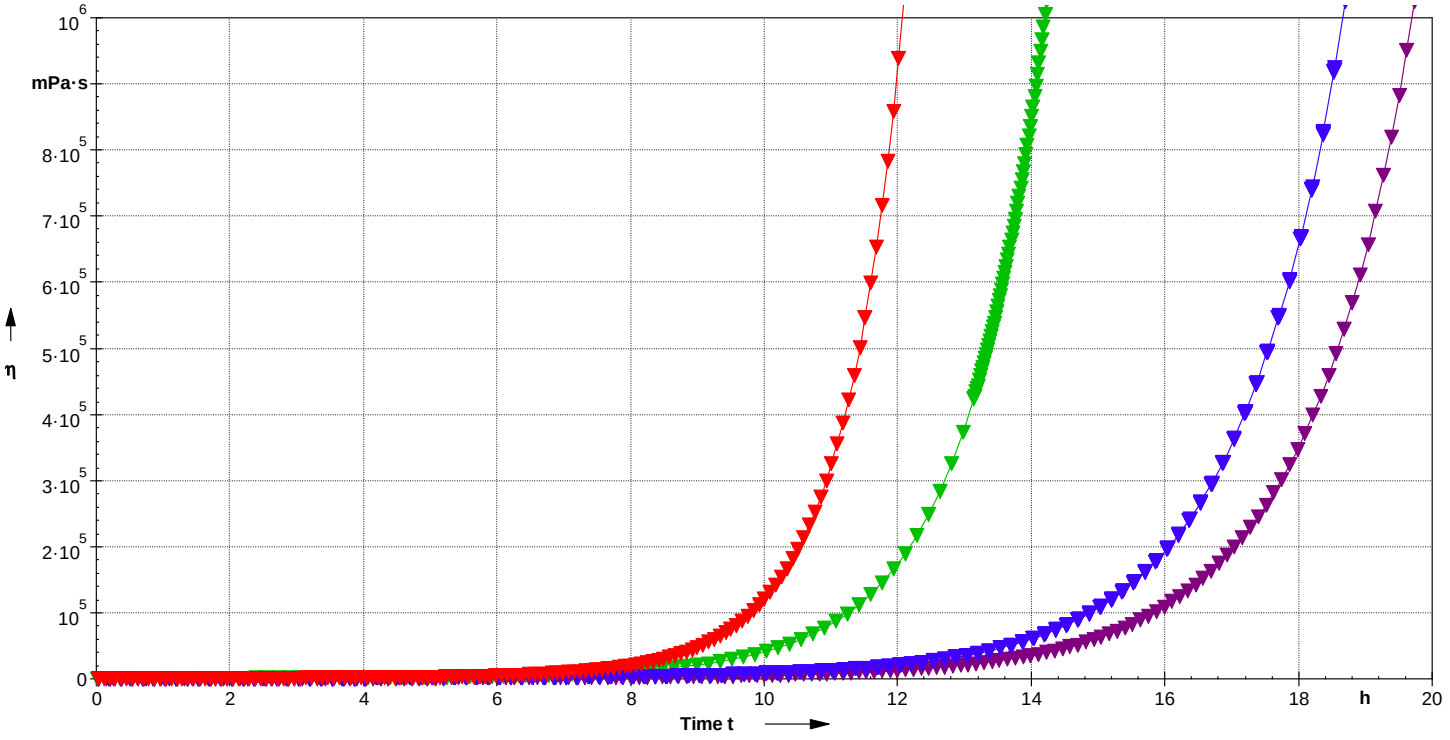

@ 30°C

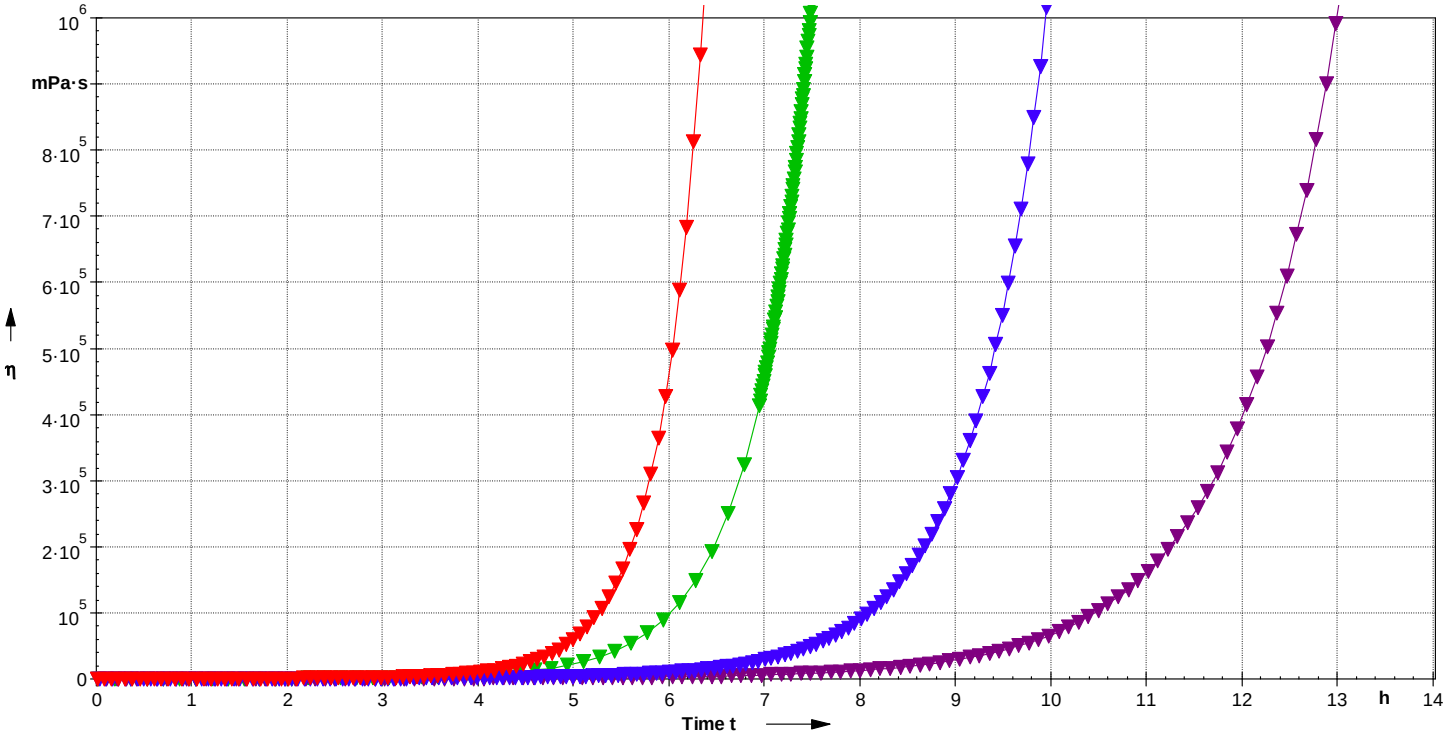

Mechanical properties on cast resin

Systems	Units	SR 8100 / SD 8822		SR 8100 / SD 8824	
Curing cycles →		24 h @ AT + 24 h 40 °C	24 h @ AT + 16 h 60 °C	24 h @ AT + 24 h 40 °C	24 h @ AT + 8 h 60 °C
Tension					
Modulus of elasticity	N/mm^2	3000	2650	2700	2400
Maximum resistance	N/mm^2	70	66	60	59
Resistance at break	N/mm^2	63	61	50	50
Elongation at max.load	%	3.3	4.1	3.2	3.9
Elongation at break	%	3.8	5.5	3.8	5.9
Flexion					
Modulus of elasticity	N/mm^2	3390	3060	2970	2850
Maximum resistance	N/mm^2	115	120	108	106
Elongation at max.load	%	3.9	5.6	4.9	5.7
Elongation at break	%	5.8	9	11.8	12
Charpy impact strength	**kJ/m^2**	19	27	52	52
Water absorption 48 h / 70 °C	**%**	1.2	1.1	1.2	1.2
Glass Transition / DSC					
Tg1	**°C**	66	80	63	74
Tg1 max.	**°C**		90		81

Propriétés mécaniques sur résine pure :

		SR 8100 / SD 4771			SR 8100 / SD 4770		
Cycles de polymérisation →		AT + 24 h 40 °C	AT + 16 h 60 °C	AT + 8 h 80 °C	AT + 8 h 40 °C 8	AT + 16 h 60 °C	AT + 8 h 80 °C
Tension							
Modulus of elasticity	N/mm^2	3400	3250	3050	3000	3150	2850
Maximum resistance	N/mm^2	78	76	71	73	75	71
Resistance at break	N/mm^2	73	71	69	67	70	67
Elongation at max.load	%	3.6	4.4	4.5	3.9	4.5	4.7
Elongation at break	%	4.0	5.3	5.4	4.5	5.7	6.3
Flexion							
Modulus of elasticity	N/mm^2	3360	2900	3000	3250	3100	2900
Maximum resistance	N/mm^2	109	105	104	107	107	103
Elongation at max.load	%	4.4	5.4	5.4	4.4	5.1	5.4
Elongation at break	%						
Shear strenght	**N/mm^2**	47	49	48	48	48	47
Compresive							
Contrainte seuil d'écoulement	N/mm^2	112	108	105	105	104	104
Déformation seuil d'écoulement	%	9	10	11	11	12	13
Impact Choc Charpy							
Resilience	KJ/m^2	26	34	34	21	25	35
Transition vitreuse							
Tg1	**°C**	65	80	83	65	76	84
Tg1 max.	**°C**			86			86

AT : Ambient Temperature
Tests carried out on samples of pure cast resin, without prior degassing, between steel plates.
Measures undertaken according to the following norms :

Tension:	NF T 51-034
Flexion :	NF T 51-001
Charpy impact strength:	NF T 51-035
Compressive:	NF T 51-101

Water absorption: Internal. Polymerisation according to cycle, machining, weighting, time spent in distilled water at 70 °C / 48 hours, weighting 1 hour after emerging, drying 24 h at 40°C, weighting, mechanical tests on 10 samples
Glass transition DSC : ISO 11357-2 : 1999 -5°C to 180°C under nitrogen gaz
Tg1 or Onset : 1st point at 20 °C/mn
Tg1 maximum or Onset : second passage

Appendix D

Material Properties for Analytical Modelling

Table D.1: Unidirectional epoxy reinforced (UD) E-glass material properties

Material Property	Value	Unit	Description
E_1	44.6	GPa	Young's Modulus in the 1-direction
E_2	17	GPa	Young's Modulus in the 2-direction
E_3	16.7	GPa	Young's Modulus in the 3-direction
ν_{12}	0.262		Poisson's Ratio in the 1-2 plane
ν_{13}	0.264		Poisson's Ratio in the 1-3 plane
ν_{23}	0.079		Poisson's Ratio in the 2-3plane
G_{12}	3.49	GPa	Shear Modulus in the 1-2 plane
G_{13}	3.77	GPa	Shear Modulus in the 1-3 plane
G_{23}	3.04	GPa	Shear Modulus in the 2-3 plane
S_{1t}	1240	MPa	Tensile Strength in the 1-direction
S_{2t}	43.9	MPa	Tensile Strength in the 2-direction
S_{3t}	31.3	MPa	Tensile Strength in the 3-direction
S_{1c}	774	MPa	Compressive Strength in the 1-direction
S_{2c}	179	MPa	Compressive Strength in the 2-direction
S_{3c}	183	MPa	Compressive Strength in the 3-direction
S_{12t}	55.8	MPa	Tensile Shear Strength in the 1-2 plane
S_{13t}	54.4	MPa	Tensile Shear Strength in the 1-3 plane
S_{23t}	52	MPa	Tensile Shear Strength in the 2-3 plane
S_{12c}	100	MPa	Compressive Shear Strength in the 1-2 plane
S_{13c}	100	MPa	Compressive Shear Strength in the 1-3 plane
S_{23c}	50	MPa	Compressive Shear Strength in the 2-3 plane
ϵ_{1tu}	3E4	$\mu\epsilon$	Maximum Tensile Strain in the 1-direction
ϵ_{2tu}	2800	$\mu\epsilon$	Maximum Tensile Strain in the 2-direction
ϵ_{3tu}	2100	$\mu\epsilon$	Maximum Tensile Strain in the 3-direction
ϵ_{1cu}	1.83E4	$\mu\epsilon$	Maximum Compressive Strain in the 1-direction
ϵ_{2cu}	1.16E4	$\mu\epsilon$	Maximum Compressive Strain in the 2-direction
ϵ_{3cu}	4.4E4	$\mu\epsilon$	Maximum Compressive Strain in the 3-direction
γ_{12u}	5E4	$\mu\epsilon$	Maximum Distortion in the 1-2 plane
γ_{13u}	5E4	$\mu\epsilon$	Maximum Distortion in the 1-3 plane
γ_{23u}	4.6E4	$\mu\epsilon$	Maximum Distortion in the 2-3 plane

Appendix E

Full-Scale Test Deflection Calculations

Cantilever Fatigue Test Calculations

The beam to be fatigue tested is expected to fail under a cantilever bending moment of 14 kNm. Testing will be conducted at 50% of this load which is 7 kNm.

The force from the cylinder rod is applied approximately 1.3 m from the cantilever clamps. This means that the required maximum cyclic load is 5.38 kN. Or approximately 550 kg.

It is calculated that the test will run approximately 70 000 cycles at low frequency of approximately 1 Hz or 2 Hz.

An initial static deflection analysis was done on the beam from 0 kN to 2.5 kN. The results are shown below for applied force vs beam tip displacement.

F_y [N]	y_disp [mm]
0	0
100	0.216
500	1.08
800	1.675
1200	2.534
1500	3.19
1800	3.842
2100	4.505
2250	4.855
2500	5.434

Assuming linear material behaviour, the table below predicts displacements for some more force vs displacement increments.

F_y [N]	y_disp [mm]
2920.833	6.255133
3221.667	6.895503
3522.5	7.535873
3823.333	8.176242
4124.167	8.816612
4425	9.456982
4725.833	10.09735
5026.667	10.73772
5327.5	11.37809
5628.333	12.01846
5929.167	12.65883
6230	13.2992
6530.833	13.93957

A FE model for the beam was made and tuned to return the same displacements as seen in the actual test.

This FE model predicts a slope at the tip of the beam of 0.740 degrees at maximum load. The analytical tip slope formula predicts tip slope to be 0.736 degrees.

Taking the tangent of this angle (Figure 1), the maximum lateral force on the cylinder is predicted to be 69.5 N or 7.1 kg.

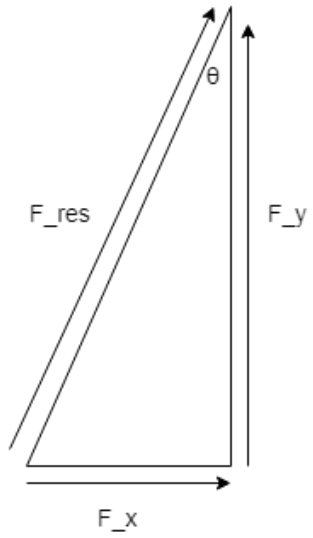

Figure 1

The deflection in the y-direction does not satisfy the criteria of "large deflections" which requires a nonlinear analysis. Despite this, concerns over additional loads on the machine perpendicular to the piston rod were analysed using nonlinear FE beam analysis. This analysis gave an indication of the x-direction displacement or effective shortening of the beam as it bends.

For a predicted deflection in the y-direction of 11.6 mm, it is predicted that the beam will deflect by 1.26e8 m or 0.0126 micrometers in the perpendicular direction. Given that the beam effectively rests on the clamp on a piece of rubber, it is expected that this displacement will induce a negligible additional perpendicular force. See Figures 2 and 3.

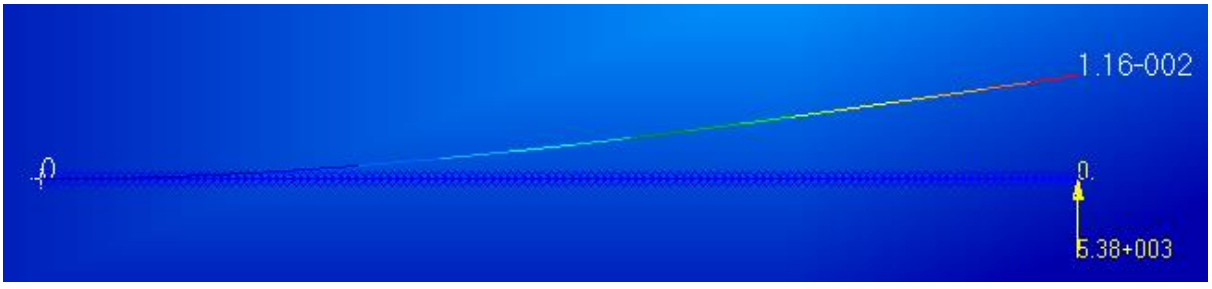

Figure 2: Y-direction deflection

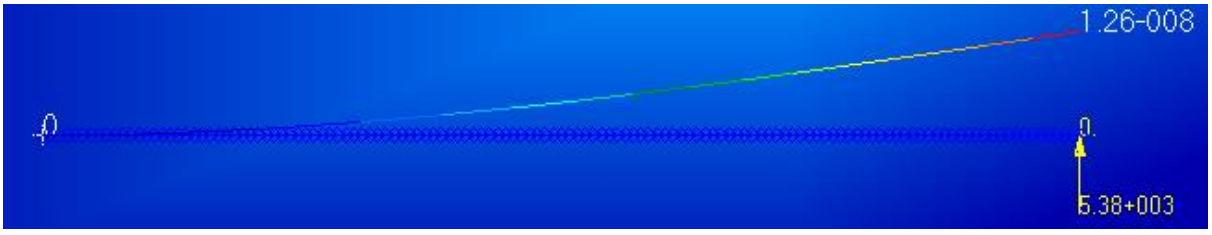

Figure 3: X-direction deflection

Despite the calculations showing low axial loads, a two -degree of freedom clevis was designed to account for possible larger deflections due to unforeseen factors like thermal expansion in the specimen, floor and mounting frame. The test will also be conducted in tension instead of compression to protect parts from buckling. The clevis is shown in Figure 4. The testing machine and support frame will be secured to the laboratory floor to ensure extra stability.

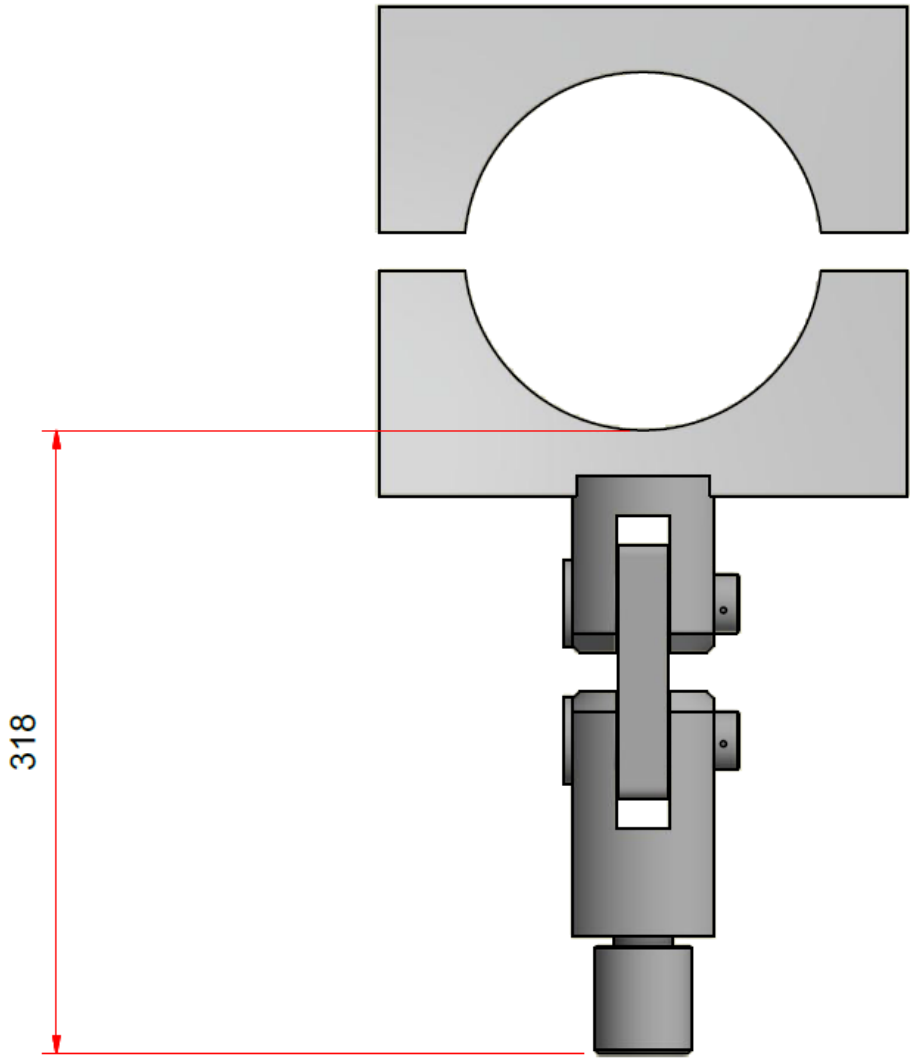

Figure 4: Clevis and clamps for tension-tension fatigue testing